BOSE-FERMI MIXTURES OF ULTRACOLD GASES OF DYSPROSIUM

BY

SEO HO YOUN

DISSERTATION

Submitted in partial fulfillment of the requirements
for the degree of Doctor of Philosophy in Physics
in the Graduate College of the
University of Illinois at Urbana-Champaign, 2011

Urbana, Illinois

Doctoral Committee:

Associate Professor Brian DeMarco, Chair
Assistant Professor Benjamin Lev, Director of Research
Professor Taekjip Ha
Professor Scott Willenbrock

Abstract

Laser cooling and trapping of the most magnetic fermionic atom, dysprosium (Dy), may provide a framework to explore quantum liquid crystal (QLC) theory (Chapter 1). This thesis presents details of the Dy laser cooling and trapping apparatus including the laser systems at 421, 741, and 1064 nm, the ultra-high vacuum (UHV) chamber, and the computer control that has produced a magneto-optically (MOT) and magneto-statically (MT) trapped Dy gas (Chapters 3, 4, 5). Despite the fact that Dy has a complex energy level structure with nearly 140 metastable states (Chapter 2), Dy MOT at 421-nm transition with 32-MHz linewidth was realized without any rempumper, exploiting its large magnetic moment, which brought a strong magnetic confinement of metastable states of Dy. This unique MOT/MT dynamics is discussed and its quantitative measurements are shown in Chapter 6. When the Dy atoms dropped from the MOT were adsorptively imaged, it was observed that Dy MOT had a bimodal temperature distribution in contrast to the usual MOT described by a single temperature (Chapter 7). Such novel anisotropic sub-Doppler laser cooling of Dy, which breaks the symmetry in cooling, is due to Dy's large magnetic spin aligned along a strong axis of the quadrupole field of the MOT, and we further support this plausible conjecture with the velocity selective resonance (VSR) theory.

The MOT at $\sim$1 mK was cooled to $\sim 10\ \mu$K by narrow-line cooling at 741 nm with a linewidth of 2 kHz, and we were able to load the optical dipole trap (ODT) at 1064 nm. By loading two isotopes of ^{164}Dy and ^{163}Dy in sequence to the MOT and narrow-line cooling them simultaneously, ultracold Bose-Fermi mixtures of Dy in the ODT were realized (Chapter 8). This thesis is concluded with a discussion of prospect on the Bose-Fermi mixtures of Dy.

To Elly and Claire.

Acknowledgments

This work would not have been possible without the guidance and support of my research advisor, Professor Benjamin Lev. I was fortunate to join him at the very early time of my graduate education. At the beginning of our dysprosium project, his great involvement in the lab was invaluable to my learning of atomic physics. It is such a precious and memorable experience to closely work with a research advisor, which is probably only possible in a newly starting research group. Also, I have been able to develop myself as a scientist from his keen physical intuition.

I am also in great debt to my colleagues in the dysprosium project, Mingwu Lu and Nate Burdick. Mingwu has set up all the lasers and the frequency stabilization systems, while I was mainly involved in the vacuum chamber project. Although Mingwu and I have been busy designing and developing the dysprosium apparatus rapidly as the first generation of the group, we have tried to have as much discussion as possible, and I have clarified a lot of physical concepts from the discussion I had with him. Nate is a new graduate student who designed and set up the optical dipole trap, and without his rapid learning of our dysprosium experiments I believe that it would not have been possible for me to timely realize ultracold Bose-Fermi mixtures of dysprosium.

I would like to also thank my current and past group members in the other two projects, atom chip and cavity QED experiments: Matt Naides, Will Turner, Alicia Kollár, Brian Kasch and Ushnish Ray. Although they were busy with their own projects, they always spared their time for me to ask questions and have discussion with them. Especially, with this opportunity, I would like to acknowledge Ushnish for his development of the control and imaging systems.

I have been greatly grateful to work next to Professor Brian DeMarco's group. I always felt like I was involved in two groups, getting help from the both. First of all, I will never forget Professor DeMarco's generosity to let me use a part of his lab space and share his students' office (I joined Professor Lev when our lab space and office were not ready) and enormous help I received from him and his students. At the building phase of dysprosium apparatus, he always welcomed me, who just started to pick up basic electronics and other necessary skills, to share and teach me his deep knowledge accumulated from his experiences.

Equally to Professor DeMarco, Matt White and Stan Kondov were so kind to explain their rubidium and potassium experimental setups in details. Matt, who is the first PhD student in DeMarco group, was very knowledgeable about not only his experimental apparatus but also electronics, computer, and everything else. Stan joined Professor DeMarco almost at the same time as I joined Professor Lev, and as I was setting up the dysprosium apparatus, he was also building up the potassium apparatus. We were learning and sharing the experimental knowledge and skills together (most of the time I learned from him, though). It was just good to learn things together. I deeply appreciate Matt and Stan about their time and explanation. David McKay and I occasionally chatted in his or my office. Since he is a joint graduate student with the University of Toronto, I could not interact with him as much as I wanted, but whenever he was in Urbana, I dragged him to discussion to scratch itchy concepts in my physical understanding.

Thanks, everyone.

A long marathon, my PhD education, would not been smoothly finished without tremendous support from my wife, Elly. Her support to my study has been extraordinary and exceptionally consistent throughout the four years spent in my graduate school and even before, since we met. Now, as I am to move onto the next stage in my life with Elly and my baby girl, Claire, I feel more confident, excited and happier than ever.

Generous support for the Dy project was provided by NSF, AFOSR, ARO, and the University of Illinois.

Table of Contents

List of Tables

List of Figures

Chapter 1

Research motivations

1.1 Introduction

The first realization of Bose-Einstein condensation (BEC) of dilute gases in 1995 [15, 16, 17] immediately led to widespread investigation of phenomena paradigmatic to condensed matter physics, such as phase transitions, phonons, superfluidity, and Josephson oscillations [18]. With cooling, trapping, and manipulation techniques developed for the achievement of BEC, there were also continuous efforts toward a Fermi degenerate gas (FDG), and it was finally realized in 1999 [19]. These quantum degenerate gases have received a great amount of attention not only in atomic, molecular, and optical (AMO) physics but also from the condensed matter community, because these atomic systems enable the exploration of many-body quantum mechanical properties and phenomena in a controlled and clean environment [20].

In the regime of ultracold gases ($\lesssim 10\ \mu$K), the properties of the degenerate gases are governed by the contact interaction [3], which reads as

$$U_{\text{contact}}(r) = \frac{4\pi\hbar^2 a_s}{m}\delta(r) \tag{1.1}$$

where a_s is the s-wave scattering length, m is atomic mass, and δ is the Dirac delta function. This short-range isotropic atom-atom interaction can be varied over a wide range of strength, as the scattering length is tuned from large negative to large positive values by applying a magnetic field through Feshbach resonances. This allows physicists to investigate the whole spectrum from a nearly non-interacting dilute gas to a strongly interacting quantum fluid [20]. Although this isotropic interaction makes the many-body physics of BEC rich [18], the dipole-dipole interaction (DDI) due to magnetic or electric dipole moments brings additional tunability in terms of range, symmetry, and strength [21]. The DDI [3] is long-range [1] (decays as $1/r^3$) and anisotropic (has angular dependence), and its energy is

$$U_{\text{DDI}}(r) = \frac{C_{\text{DDI}}}{4\pi}\frac{1-3\cos^2\theta}{r^3} \tag{1.2}$$

[1] DDI is a long-range interaction in three dimensions but a short-range interaction in lower dimensions by its definition.

where r is the distance between two particles, and θ is the angle between the polarization direction and the relative position of the two particles. C_{DDI} is the coupling constant, which is equal to $\mu_0\mu^2$ for particles with a magnetic dipole moment μ and d^2/ϵ_0 for particles with an electric dipole moment d, where μ_0 is the permeability of vacuum and ϵ_0 is the permittivity of vacuum. As a consequence of having angular dependence in the DDI, the interaction can be repulsive or attractive, depending on how the particles approach each other (Fig. 1.1).

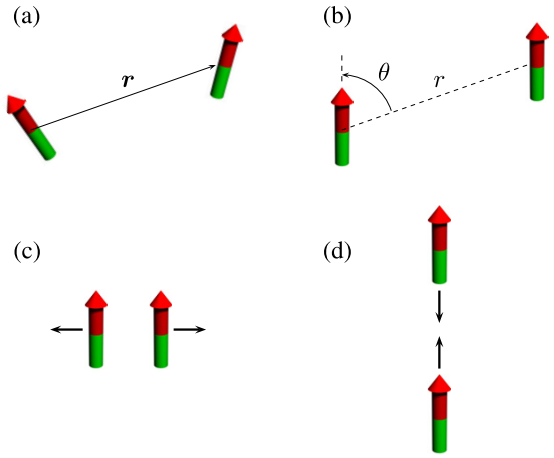

Figure 1.1: Dipole-dipole interaction between two particles. (a) Unpolarized particles. (b) Polarized particles. (c) Repulsive interaction when particles are side by side. (d) Attractive interaction when particles are top and bottom. Reproduced from *Rep. Prog. Phys.* **72**, 126401 (2009) [3].

1.2 Dipolar physics with dysprosium

Ultracold gases of fermionic dipolar atoms provide the opportunity to examine—in a pristine and tunable setting—the non-Fermi liquid, strongly correlated electronic behavior manifest in some of the most interesting materials of late: high-T_c cuprate superconductors, strontium ruthenates, 2D electron gases, and iron-based superconductors. Strong and competing interactions in these systems induce transitions to states beyond the familiar insulating, metallic, and superconducting. Specifically, phases that break rotational and translational symmetries emerge in a manner akin to those found in classical liquid crystals, e.g., the nematic and smectic [5, 22] (Fig. 1.2). Although quantum liquid crystal (QLC) theory can describe these non-Fermi liquids in a compelling and general framework, unwanted solid state material complexity—disorder and dynamical lattice distortions—can obscure the underlying electronic physics, and lack of wide system tunability can hamper efforts to fully explore QLC phase portraits (Fig. 1.3).

Exploiting large dipole-dipole interactions in ultracold gases will allow the exploration of QLC physics in

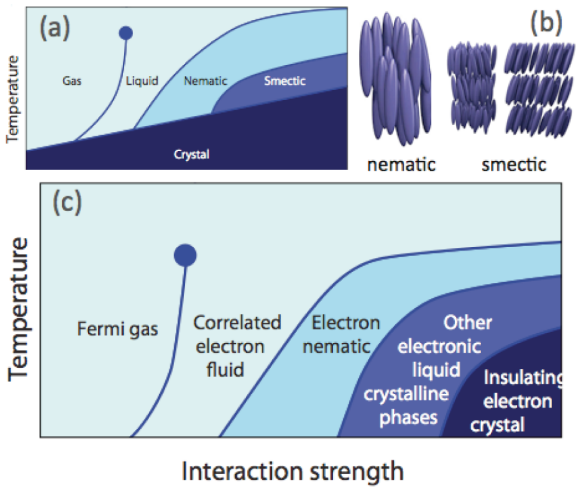

Figure 1.2: (a) Sketch of a classical liquid crystal phase diagram versus a tunable parameter. Nematics (smectics) arise from broken rotational (rotational plus translational) symmetry, as may be seen in panel (b). (c) Presumptive quantum liquid crystal phase portrait. Reproduced from *Science* **315**, 196 (2007) [4].

this inherently more tunable and characterizable system. Recent theoretical proposals employing strongly magnetic fermionic atoms or polar fermionic molecules have begun to shed light on the accessible QLC physics. These include predictions of uniaxial (meta-nematic) [23] and biaxial nematic [24] distortions of the Fermi surface in the presence of a polarizing field, and meta-nematic and smectic phases in 2D anisotropic optical lattices [25]. An exciting prospect lies in the possibility of observing spontaneous magnetization in dipolar systems, and Refs. [26, 27] postulate the existence of observable quantum ferro-nematic phases and spin textures in ultracold highly magnetic fermionic atomic gases in zero polarizing field.

While many exciting results will continue to arise from the degenerate fermionic dipolar molecule system [28, 29, 30, 31], to most easily observe true (non-meta) QLC phases, the symmetries of interest should be spontaneously broken, which is not possible when employing ground state polar molecules, although polar molecules have a high electric dipole moment in an electric field. This is because the strong, r^{-3} character of the DDI is realized only in the presence of a rotational symmetry breaking, polarizing electric field that mixes opposite parity states. Ultracold chemical reactions can also hamper the use of fermionic polar molecules for studies of DDI-induced exotic phases in 3D, as recent experiments in KRb have shown [30, 31]. In contrast, highly magnetic atoms exhibit the DDI interaction even in the absence of a polarizing field and are largely immune to chemical and inelastic collisions when spin-polarized in an optical dipole trap. While both the electric and magnetic DDI can be continuously tuned to zero, only the magnetic DDI can be tuned negative [32].

One must look to the rare earth (lanthanide) series to find atoms possessing masses and magnetic moments large enough to support exotic bosonic and fermionic phases. The extraordinarily large magnetic dipole of

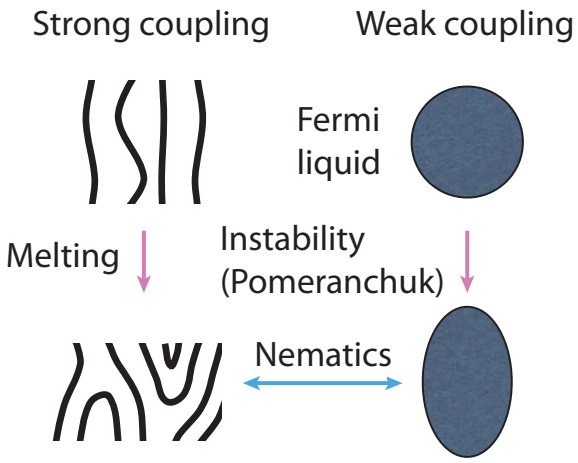

Figure 1.3: (a) Strong versus weak coupling picture of electronic quantum liquid crystals. Electron nematics may arise from the melting of a strongly coupled, conductive stripe phase in a manner that restores translational symmetry while leaving rotational broken. This may occur by a proliferation of topological defects of the smectic phase (dislocations). (b) Alternatively, nematics may arise from spontaneous distortions of the Fermi surface when long-range interactions are sufficiently strong to drive Landau free energy parameters deeply negative in a particular angular momentum channel (quadrupolar shown here). Sketch adapted from *Annu. Rev. Condens. Matter Phys.* **1**, 7 (2010) [5].

dysprosium (10 μ_B), which possesses the largest magnetic moment of any fermionic atom—and is tied with terbium in possessing the largest moment among bosonic atoms [2]—is likely sufficient to induce QLC phases [25, 26, 27].

It is not yet clear whether a degenerate gas of highly magnetic lanthanide atoms is possible to create [3], but overcoming a large DDI while cooling to degeneracy has precedent in the Bose-Einstein condensation (BEC) of chromium [21]. The attainment of Cr BEC opened the door to bosonic ultracold dipolar physics [3]. Chromium possesses the large magnetic dipole moment of 6 Bohr magnetons (μ_B). This is 6-times larger than that of the alkali atoms'—Rb has a magnetic moment of $\mu = 1\ \mu_B$ in the doubly-polarized state—and represents a significant 36-fold enhancement in the DDI strength (Eq. 1.2). However, as strong as Cr's DDI may be, recent calculations [34] suggest that novel lattice phases predicted by the extended Bose-Hubbard (eBH) model [3], such as density waves and lattice supersolids [35], lie just beyond the reach of Cr's capability. Specifically, the DDI energy must dominate the contact interaction energy, which occurs when $\epsilon = \mu_0\mu^2 m/12\pi\hbar^2 a_s \gtrsim 1$, and the extra factor of 3 in the denominator designates $\epsilon \geq 1$ as the regime in which homogeneous dipolar BECs become unstable to collapse [3]. To observe novel lattice phases, ϵ should be >0.7–0.8 [34]. For ^{52}Cr, $\epsilon_{\mathrm{Cr}} = 0.15$, and even with the demonstrated five-fold reduction of a_s

[2]Terbium has only one isotope, a boson. Unfortunately, it possesses a 400 K electronic state that could be driven by incoherent blackbody radiation, thus limiting coherence and trap lifetimes. Additionally, thulium (4 μ_B) [33] and holmium (9 μ_B) have only single bosonic isotopes.

[3]At writing of this thesis, we have realized Bose-Einstein condensation of ^{164}Dy.

via a Feshbach resonance [36], $\epsilon_{\mathrm{Cr}} = 0.7$ remains at or below the threshold for new phases. In contrast, $\epsilon_{\mathrm{Dy}} = 1.34$ which is 9× larger than ϵ_{Cr}, assuming that the as yet unmeasured scattering length for at least one of Dy's bosonic isotopes is approximately equal to ^{52}Cr's $a_s = 100\ a_0$, where a_0 is Bohr radius. With such a large ϵ_{Dy}, exploring supersolids and density wave phases without the use of Feshbach resonances should be possible with Dy.

As candidates for fermionic dipolar physics, existing MOTs of highly magnetic fermionic ^{53}Cr and ^{167}Er are not yet populous enough to contemplate cooling to degeneracy [37, 38]. The technique of buffer gas cooling has been used for cooling lanthanides and has proven successful in producing large 500 mK samples [39]. While Dy has been adiabatically cooled to ∼50 mK at final densities of $\sim 10^9$ cm^{-3} [40] in such an experiment, evaporative cooling in a magnetic trap to lower temperatures has not yet proven effective due to large inelastic collisions. Thus, the extraordinarily populous $\sim 10\ \mu$K Dy samples discussed in this thesis open the door to a rich landscape of physics.

Ultracold samples of bosonic and fermionic isotopes of Dy would find application beyond the QLC and eBH physics described above. Co-trapped isotopes of Dy present an interesting system to explore Bose-Fermi mixtures of near equal mass, reminiscent of ^{3}He-^{4}He studies, but now in the presence of same and cross-species dipolar interactions. Indeed, Wang *et al.* theorize a novel phase transition such as quantum melting of Bose-Fermi solid [41] .

Studies of large-spin degenerate spinor gases [42, 43], simulations of dense nuclear matter [44], creation of unconventional superfluid pairing [45], and explorations of zero sound [46] and roton modes [47] in dipolar gases are exciting avenues of research. In addition, ultracold samples of Dy will aid precision measurements of parity nonconservation and variation of fundamental constants [48], single-ion implantation [37], and quantum information processing [49, 50]. With regard to the latter, the low-lying telecom (1322 nm) and InAs quantum dot amenable (1001 nm) transitions (see Fig. 2.2) will be useful for creating hybrid atom-photonic or atom-quantum systems that exploit potentially long-lived spin coherences in ensembles of Dy for quantum memory. Novel ultracold collisions [51] and complex Feshbach resonance-induced molecular association phenomena are expected to appear in traps of these non-S state atoms, which may enable exploration of 1D strongly correlated gases with highly magnetic molecules [52].

1.3 Experimental considerations

In addition to these theoretical motivations, dysprosium is an attractive atomic species to work with from an experimentalist's point of view. First, due to the almost equal natural abundance of bosonic and fermionic

isotopes (see Chapter 2), dysprosium has an advantage of studying the physics of Bose-Bose [53], Fermi-Fermi [54], or Bose-Fermi mixtures [55]. Second, the ability to realize BEC or FDG highly depends on the collisional properties of species—for instance, if the scattering length is too small, the cooling efficiency is too low to realize quantum degeneracy. Because different isotopes may have different collision rates (either elastic or inelastic) [4], one can explore isotopes to achieve quantum degenerate gases.

While most of the cooling and trapping techniques developed for BEC can be used to achieve degenerate Fermi gases, there is one additional crucial cooling technique required—*sympathetic cooling*. Evaporative cooling, the only means to realize BEC so far, works by evaporating the hot component of gas and rethermalizing the remainder to a lower temperature. This cooling technique, however, is not possible for identical fermions [5] because spin-polarized fermions do not collide with each other in the ultracold regime [6]. Therefore, fermions are sympathetically cooled by introducing another species, or the same species in a different spin state, in order to induce elastic collisions.

However, inability for identical fermions to elastically collide may not be true for dipolar fermions, because there is still a possible scattering channel via DDI. The elastic collision cross section due to DDI does not vanish as the interaction temperature (or the particle temperature) decreases to the ultracold regime [56]. For the dipolar fermions, the cross section σ^{o} [56] via elastic binary collisions by Born approximation [7] can be calculated by

$$\sigma^{\mathrm{o}} = 3.351 D^2 = 3.351 \frac{M^2 \mu^4}{\hbar^4} \tag{1.3}$$

where CGS units are used, the superscript denotes the odd partial waves, the dipolar length, which characterizes dipolar strength, D is $M\mu^2/\hbar^2$, M is the reduced mass of particles, and μ is the dipole moment. Using Eq. 1.3, $\sigma^{\mathrm{o}}_{\mathrm{Dy}} \sim 4 \times 10^{-12}\, cm^{-2}$, compared to the polar molecule KRb $\sigma^{\mathrm{o}}_{\mathrm{KRb}} \sim 3 \times 10^{-9}\, cm^{-2}$. A more interesting comparison is with the elastic cross section of Rb Bose gas $\sigma_{\mathrm{Rb}} = 8\pi a_s^2 \sim 7 \times 10^{-12}\, cm^{-2}$ with $a_{\mathrm{Rb}} \sim 100\, a_0$. By this back-of-the-envelope calculation, it is plausible to predict the possibility of evaporatively cooling identical dipolar fermions in the same spin state *only* via the universal dipolar scattering, as efficiently as Rb bosons. In fact, our group has observed that all the isotopes except for ^{163}Dy, which suffers hyperfine changing collision, show a similar or universal behavior in the evaporative cooling.

The last but important collision to be considered for quantum degeneracy is inelastic collision due to three-

[4] Inelastic collisions cause heating in the cloud of trapped atoms.

[5] Our research group has just observed that identical *dipolar* fermions may collide via universal dipolar scattering. See the text.

[6] Partial waves due to atom-atom interaction with angular momentum l contribute to collisions scaling as T^{2l}, where T is temperature. As T is lowered, only s-wave scattering ($l = 0$) becomes possible. However, the anti-symmetry requirement of the wavefunction of two colliding fermions means that angular momentum l must be odd, forbidding any of these collisions.

[7] The Born approximation is valid for the ultracold regime.

body recombination, which can be large because of its scaling of μ^8 (see below) but is to be experimentally measured for dysprosium. This "bad" inelastic collision occurs in atoms with a high density $\gtrsim 10^{13}$ cm^{-3}and still can happen even in the polarized ground state of atoms, unlike spin relaxation, which is suppressed for the polarized gas. It is instructive to estimate the three-body recombination rate in regards to the evaporative cooling efficiency. Three-body recombination rate coefficient K may be roughly estimated by the following equation [57]:

$$K \to 495\hbar D^4/M \sim 5 \times 10^{-27}\,\mathrm{cm}^6/\mathrm{s}. \tag{1.4}$$

Here it is assumed that the dipolar length is greater than s-wave scattering length. This estimation is larger than the measured value of rubidium [58] but again it is still remained to be observed how the three-body recombination affects dysprosium.

Chapter 2

Dysprosium

Dysprosium (Dy) is a rare earth element with atomic number 66. Dy has a bright silver color, and is soft enough to be cut with a knife and machined. The most important characteristic of Dy in designing the vacuum system was its melting point, which is 1412 °C [6]. In order to produce the Dy atomic source, one needs to heat up Dy to a high temperature because of its high melting point [1]. Dy also has a chemical getter property, which helps the ultra-high vacuum. In our experiments, as experiments have been running and the inner wall of the chamber has been coated by the Dy deposited film, it was observed that the vacuum pressure had decreased.

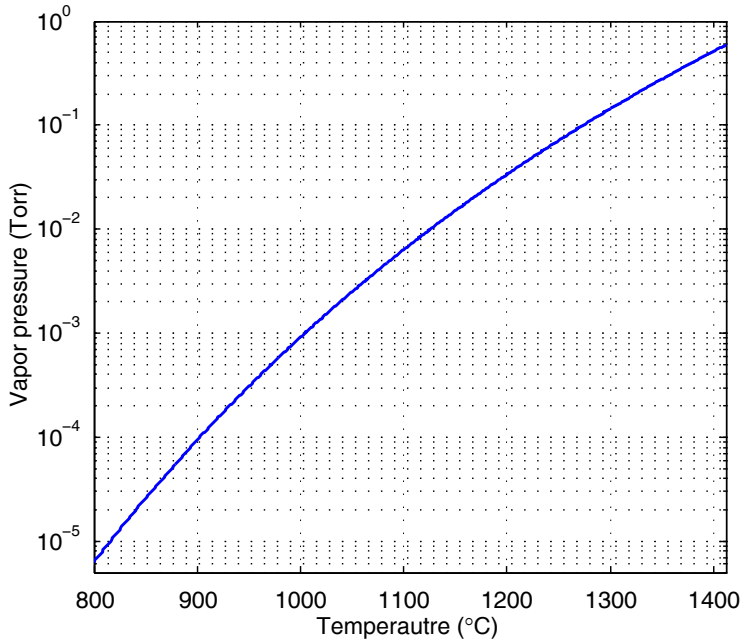

Figure 2.1: The vapor pressure as a function of temperature [6]. The atomic beam starts to be detected roughly from 800 °C. The typical operation temperature is 1250 °C.

Dy has the almost equal natural abundance of bosonic and fermionic isotopes (Table 2.1), which enables

[1] In comparison, rubidium, which is one of the most common elements studied in AMO physics, has a melting point of only 40 °C.

Table 2.1: Natural abundance of nuclear spin of stable dysprosium isotopes [1].

isotope	mass [au]	abundance [%]	nuclear spin	statistics
^{160}Dy	160	2.34	0	boson
^{161}Dy	161	18.9	5/2	fermion
^{162}Dy	162	25.5	0	boson
^{163}Dy	163	24.9	5/2	fermion
^{164}Dy	164	28.2	0	boson

Table 2.2: Laser cooling parameters for the $4f^{10}6s^2\,{}^5I_8 - 4f^{10}({}^5I_8)6s6p({}^1P^\circ{}_1)\,(8,1)^\circ{}_9$ transition from NIST database and Ref. [2] .

symbol	description	definition	value
λ	atomic wavelength (air)		421.1714 nm
k	wavevector	$2\pi/\lambda$	23743 cm^{-1}
g_g, g_e	Landé-g factor		1.24159, 1.22
Γ	spontaneous decay rate	$1/\tau$	2.02×10^8 s^{-1}
τ	lifetime of excited state	$1/\Gamma$	4.94 ns
ν	natural linewidth	$\Gamma/2\pi$	32.2 MHz
I_s	saturation intensity	$\pi hc\Gamma/3\lambda^3$	56.4 mW/cm^2
v_c	capture velocity	$\Gamma\lambda/2\pi$	14 m/s
T_D	Doppler temperature	$\hbar\Gamma/2k_B$	$774\mu K$
T_r	recoil temperature	$\hbar^2k^2/mk_B$	660 nK
a_{max}	Maximum acceleration	$\hbar k\Gamma/2m$	579000 m/s^2

one to explore Bose-Fermi mixtures of Dy. In this thesis, the most abundant ^{164}Dy and ^{163}Dy are mainly studied. In laser cooling and trapping, spectroscopic properties and transitions play an important role, and the relevant transitions are shown in Fig. 2.2. The strongest 421-nm transition with a broad linewidth of 32 MHz [2] is used for Zeeman slowing, magneto-optical trapping, and imaging, which efficiently captures atoms and forms the largest possible cloud of trapped atoms. The laser cooling parameters for the 421-nm transition are summarized in Table 2.2. The realization of magneto-optical trapping of Dy did not seem obviously possible from the beginning of our Dy project because of its complex energy level structure (Fig. 2.2). In the Dy MOT, any of the 140 metastable states between the ground and the 421-nm excited states may cause the atom loss. However, the strong magnetic trapping force due to the large magnetic moment of Dy confines these untrappable atoms in the dark states (Chapter 6). One can think of this novel MOT as a combination of MOT and magnetic trap (MT). This blue MOT at 421 nm (BMOT) prepares a half billion of atoms at $\sim$ mK, which is the Doppler limit (Table 2.2) and is far from the quantum degeneracy. In the following cooling phase (Chapter 8), 741-nm transition with a narrow linewidth of 2 kHz [2] is used to cool the Dy atoms further down to the utlracold regime at $\sim 10\mu$K, and the far-off resonant optical dipole trap at 1064 nm is loaded.

Fermionic isotopes of ^{163}Dy and ^{161}Dy, which have the hyperfine structure with six manifolds (Fig. 2.3), complicate laser cooling and trapping. The usual treatment for this is to employ repumpers, which transfer

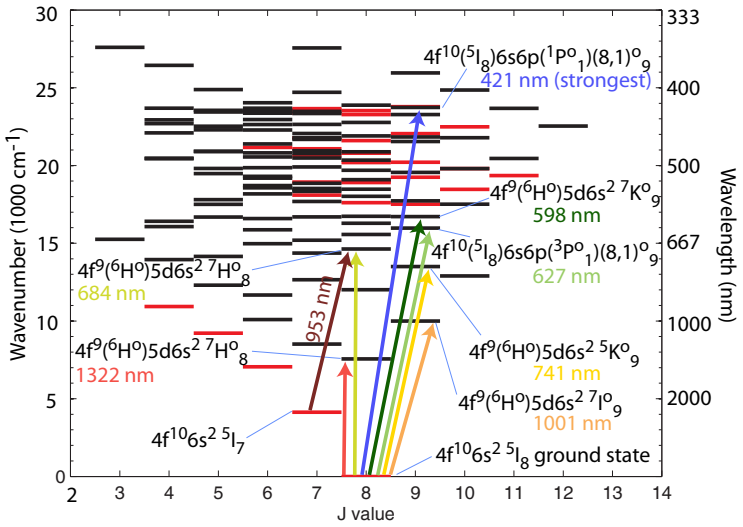

Figure 2.2: Dy energy level structure [7], where J is the total electronic angular momentum and $F = J + I$, the total electronic plus nuclear angular momentum. The strongest 421-nm transition is employed to laser cool and trap dysprosium.

the untrappable states to the trappable states in oder to avoid atom loss. However, our previous experiments show that the close spacing between $F \to F' = F + 1$ transitions and the high intensity of Zeeman slowing beam (leading to the power broadening) make it possible to laser cool and trap fermionic Dy without any additional repumper, and its population is comparable to ^{164}Dy [59].

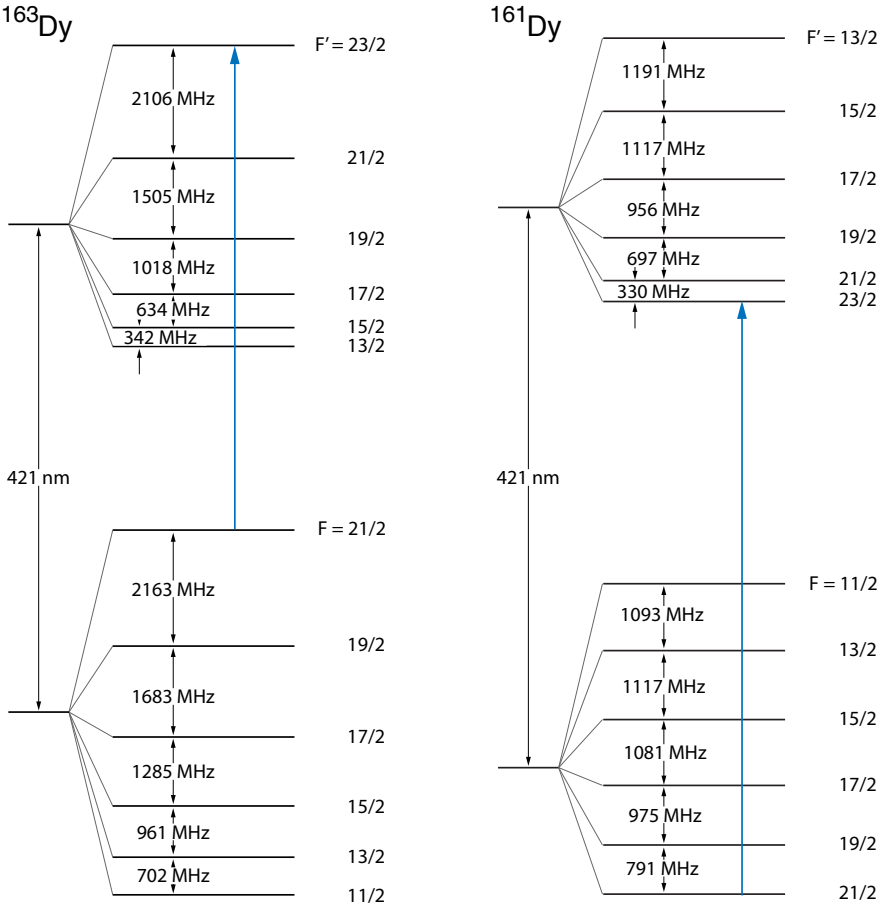

Figure 2.3: Hyperfine structure of ^{163}Dy and ^{161}Dy [8, 9]. The cooling transitions (largest) $F = 21/2 \rightarrow F' = 23/2$ are depicted as blue arrows, while other $F \rightarrow F' = F + 1$ transitions are red arrows. The two fermions have oppositely signed nuclear spin, resulting in a relative inversion in the hyperfine structure.

Chapter 3

Laser cooling system

3.1 Overview

A simple laser cooling and trapping method for highly magnetic atoms has now proven successful for three magnetic lanthanides, Er, Dy, and Tm [37, 60, 33]. Measurements of MOT recycling dynamics show that the working principle behind the Er and Dy MOTs are similar [37, 60]. Despite the existence of more than a hundred levels between ground and the open excited state of the cooling transition, no repumping laser is necessary because of a novel recycling mechanism [37]: After decaying out of the MOT cooling transition to metastable states, the highly magnetic atoms remain confined in the MOT's magnetic quadrupole trap while the metastable state population recycles to the ground state, at which point the atom are recaptured by the MOT. The strongest transition $J \rightarrow J+1$ transition is used for Zeeman slowing and MOT cooling. Whereas weakly magnetic atoms would be lost from the trapping region during time in which the atoms spend in the metastable states, the strong dipole moments (7 μ_B for Er) allow confinement even in the MOT's magnetic quadrupole gradient. The $1{:}10^5$ branching ratio between population decay back to the ground state versus to the metastable state is sufficient for a MOT to form given the efficient population recycling.

There are four criteria necessary for the large-population, highly magnetic, repumperless MOT to work when using strong open transitions: 1) to be captured by the MOT, the branching ratio must be small enough that atoms exit the Zeeman slower in their ground state; 2) the decay channel through the metastable states must be rapid enough that inelastic collision processes—from background, spin-changing, or light induced collisions—do not deplete the metastable magnetic trap (MT) reservoir; 3) decay through the metastable MT should be slow enough for it to serve as a reservoir to capture more atoms than those cycling on the MOT transition; 4) for isotopes with $I \neq 0$, the difference frequencies between adjacent $F \rightarrow F' = F + 1$ hyperfine transitions in the ground and excited states must be small enough that the cooling laser itself serves as a repumper.

3.2 421-nm laser set-up

3.2.1 Frequency stabilization

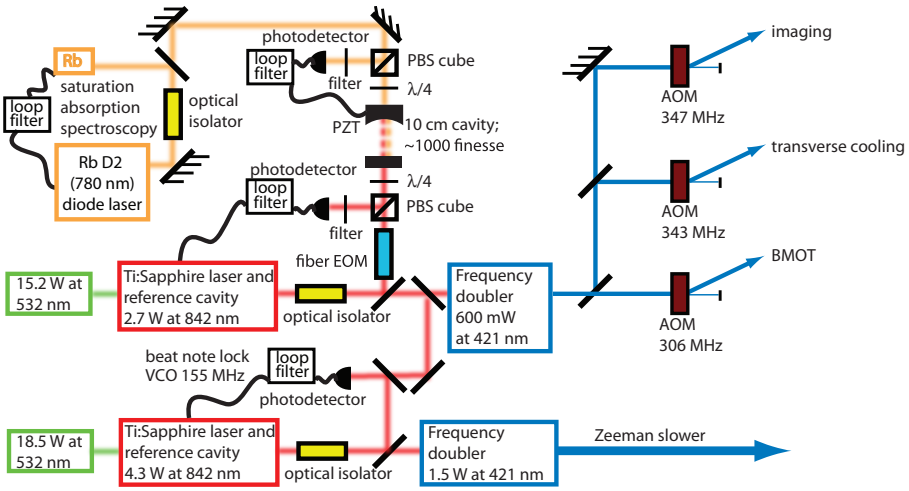

Figure 3.1: Schematic of the Dy laser cooling system.

The strongest $J \to J+1$ cycling transition is the 421-nm line, which has a broad linewidth of 31.9(0.7) MHz [7, 2]. A total of 2 W of 421-nm optical power is generated by two Ti:sapphire laser systems. Such high power is necessary because the saturation intensity 58 mW/cm^2 is large and, as we discuss below, the Zeeman slower optimally uses 1 W of power. The first Ti:sapphire system (TiS1) is pumped with 15.2 W at 532 nm, which when frequency doubled in a ring cavity with an LBO crystal produces 600 mW of continuous wave (CW) 421-nm light with a 20-kHz linewidth [61]. The second doubled Ti:sapphire laser system (TiS2) produces up to 1.6 W CW at 421 nm (again using a ring cavity frequency doubler) from a 4.3 W 842-nm beam. TiS2 is pumped by a 18.5 W 532-nm laser, and the 421-nm light has a linewidth of ∼50 kHz at 421 nm.

TiS1 produces the 421-nm light for the MOT, transverse cooling, and imaging beams, while TiS2 is used solely for the Zeeman slower. Each laser is locked, at 842 nm, to its own low-finesse reference cavity. These cavities exhibit ∼40 MHz/hr frequency drift, so we have developed a more stable locking scheme which provides a long-term stability of several 100 kHz. The frequency reference is derived using the transfer cavity technique: the 842-nm light from TiS1 is locked to a mode of an optical cavity whose length is stabilized by a 780-nm laser that is resonant with the cavity $\sim 2 \times 10^4$ modes away. This 780-nm laser is itself frequency stabilized to a hyperfine transition in Rb using saturation-absorption spectroscopy. Thus, the stability of a medium-finesse cavity locked to a Rb frequency reference is transferred to the 842-nm laser of the TiS1 system. The TiS2 system is offset locked [62] at the Zeeman slower laser detuning by detecting a beat note

at 842-nm between the TiS1 and TiS2 lasers. Fig. 3.2 describes the optics and the electronics used for the beat note lock, and Fig. 3.3 shows the beat note signal of two laser beams.

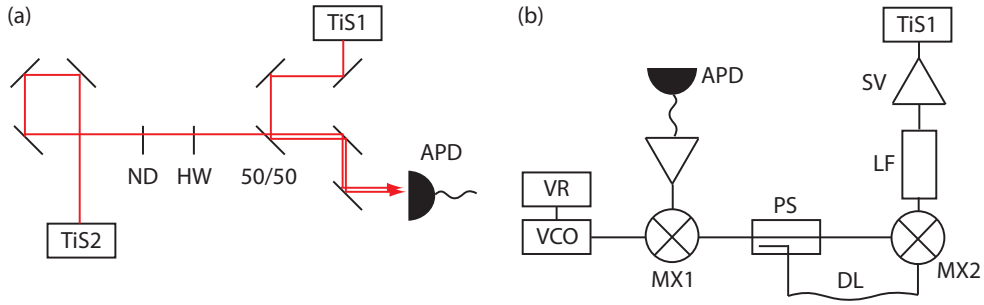

Figure 3.2: Schematic of the 421-nm beatnote lock. (a) Optics. ND: neutral density filter to match the intensity of TiS1 and TiS2 beams. HW: half-wave plate to match the polarization. APD: avalanche photodetector (Thorlabs APD210). (b) Electronics. VR: tunable voltage reference 0 – 15 V. VCO: voltage controlled oscillator (Minicircuits ZOS-300+). MX1: mixer (Minicircuits ZX05-12MH+). Amplifier: Minicircuits ZKL-2R5. PS: power splitter (Minicircuits ZSC-2-1+). DL: delay line ($\sim$ 2 m). MX2: mixer (Minicircuits ZP-3+). LF: low-pass filter (Minicircuits BLP-1.9+). SV: servo.

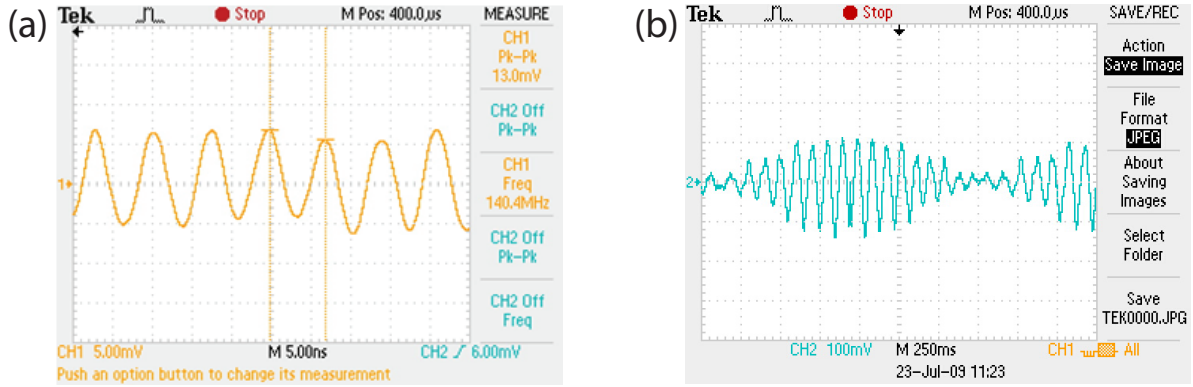

Figure 3.3: Screenshots of optical beating. (a) Signal from APD. Frequency of oscillation is the difference between TiS1 and TiS2. (b) Error signal that goes into the servo as TiS1 frequency-scans. TiS1 is stabilized to the zero point.

3.2.2 Transfer cavity lock

The external cavity diode laser at 780 nm (Fig. 3.4) is locked to a Fabry-Pérot cavity using the Pound-Drever-Hall (PDH) technique [63]. The Fabry-Pérot cavity consists of plano and concave (r = 25 cm) mirrors with high reflectivity (99.9%) at both 780-nm and 842-nm, and the mirrors are attached to a fused silica spacer with a length of 10 cm. In order to scan the resonance frequencies of the cavity, a piezoelectric transducer (PZT) ring is placed between one side of the spacer and the concave mirror. With the measured

cavity length, the corresponding free spectral range is 1.4 GHz, and the cavity has a linewidth of 1.4 MHz. The cavity is isolated from acoustic vibration and placed inside a vacuum chamber. The laser is locked to the cavity, which provides short time scale frequency stability, and then the cavity length is adjusted to bring the cavity and laser in resonance with a hyperfine transition of ^{87}Rb. Feeding back to the cavity PZT an error signal derived by Rb saturation absorption spectroscopy ensures that the cavity resonance frequencies drift by no more than a few hundred kHz.

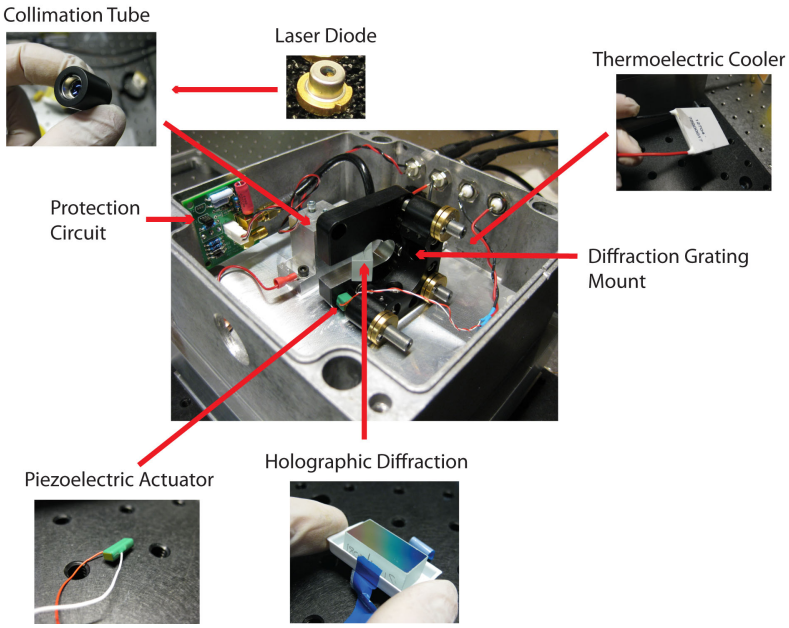

Figure 3.4: Home-built external cavity diode laser (ECDL) at 780 nm. The original design is credited to DeMarco group (see Ref. [10]).

The cavity now provides a stable frequency reference for TiS1's 842 nm beam, which is picked-off from the main beam that is directed into the ring cavity frequency doubler. To bridge the frequency gap between the nearest 842 nm mode and the doubled 842-nm wavelength necessary for generating the MOT light, the 842-nm beam passes through an optical fiber-based electro-optical modulator, which imprints strong sidebands at a frequency adjustable between 1.4 GHz–2.8 GHz. A phase-locked loop generates this microwave frequency from a stabilized and tunable RF source. One of the sidebands is adjusted in frequency to be resonant with the optical cavity, allowing the 842-nm to be locked to the cavity using the PDH technique. Once locked, the 421-nm light from both TiS1 and TiS2 (which is offset beat note locked to TiS1) may be scanned to the correct frequency by adjusting the RF reference.

3.3 741-nm laser system

Fig. 3.5 shows the schematic of the 741-nm laser system. A commercial ECDL with 18 mW is first split into three: two for ^{164}Dy and ^{163}Dy RMOT beams and one for Pound-Drever-Hall (PDH) locking branch. We use a polarization maintaining optical fiber network with two inputs and four outputs to guide the RMOT beams [1]. Each RMOT beam has a waist of 4.5 mm and an intensity of about 800 μW/cm^2. The typical operating detuning is about +1 MHz [2]. The RMOT detuning is not as sensitive as BMOT detuning to the trap population or the atomic temperature. Although the 741-nm ECDL has a 200 kHz linewidth itself, a better frequency stabilization is achieved by a transfer cavity scheme similar to the 421-nm laser system (Fig. 3.1). After locking the 741-nm laser to the cavity stabilized by the stable 780-nm, the linewidth is estimated to be 20 kHz and its long-time drift is 10 kHz/10 mins.

However, later it turns out that the long-time drift inhibits from running experiments for a long time, because although a small drift in the detuning of RMOT beams does not perturb RMOT the relative position of RMOT to the optical dipole trap (ODT) sensitively changes the ODT population [3]. Currently, in progress is a new laser locking system using a 420-nm two-photon spectroscopy of Rb.

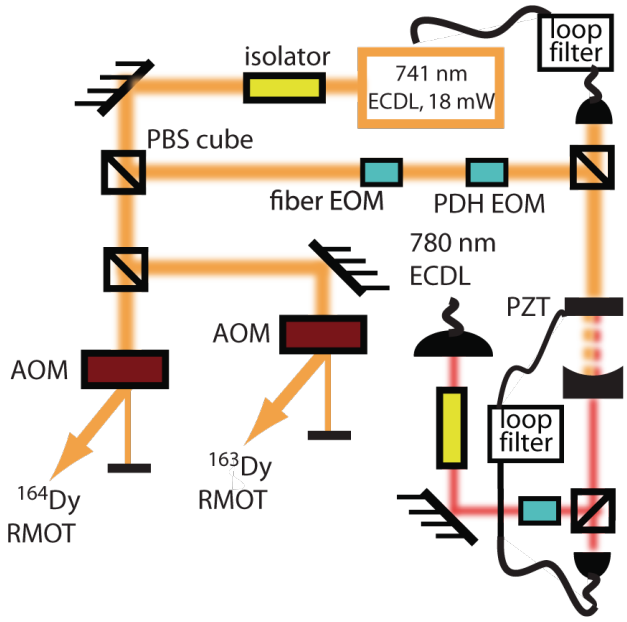

Figure 3.5: The 741-nm ECDL and its frequency-stabilization system.

[1] The fourth output is used to monitor the beam power or to test the polarization coupling.
[2] The zero-detuning was determined by disappearing the cloud of RMOT atoms at the zero point of quadrupole field.
[3] We believe that this is due to ac-Stark shift by the 1064-nm ODT beam with respect to the 741-nm atomic transition.

3.4 1064-nm laser system

The optical dipole trap is formed by a far-red-detuned single beam at 1064 nm [4]. In order to determine the lens system (Fig. 3.6), the waist ω_x at the cloud of atoms was first calculated with a given ODT beam power of 22 W [5], a target trap depth [6], and the theoretical polarizability [64]. Considering a geometrical and spatial constraint of the distance from the lens to the center of vacuum chamber and using a formula of $1/f_{\text{eff}} = 1/f_{\text{ML}} + 1/f_{\text{BL}}$ for zero-spacing between two lenses, the optics was chosen. Then, the input beam ω_0 was determined by a formula $\omega_x = \frac{f\lambda}{\pi\omega_0}$.

We use a 67-μm beam waist (ω_x), and the trap frequency is measured to be 281 Hz, which corresponds to a trap depth of 70 μK [7].

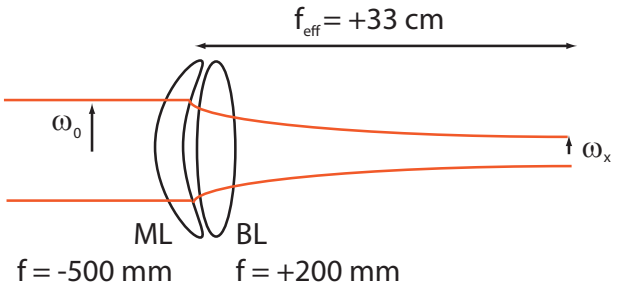

Figure 3.6: Optics for the optical dipole trap. A combination of meniscus lens (ML) and best form lens (BL) closely put gives an effective focal length of 33 cm, which is constrained by Dy trapping chamber size.

[4] We have tried to use a 532-nm laser for the optical dipole trap, but it was not successful because of its "bad" polarizability; 532 nm is in the middle of many Dy atomic transitions (Fig. 2.2).

[5] The power at the cloud of atoms.

[6] The gravitational potential is taken into account.

[7] This measured trap depth is about 60 % of our initial theoretical estimation.

Chapter 4

Vacuum chamber

4.1 Overview

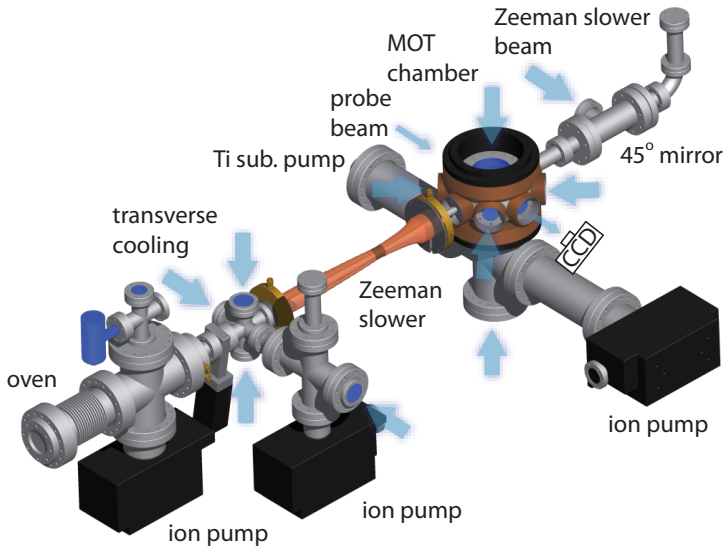

Figure 4.1: Sketch of the Dy UHV chamber system. The blue arrows depict the slowing, cooling, and imaging laser beams.

Fig. 4.1 illustrates the schematic of our Dy vacuum chamber system. A thermal atomic beam is first generated with a high-temperature oven. This atomic source is then collimated through a differential pumping tube, and a larger flux is achieved by transverse cooling. The Dy atoms are decelerated and cooled by a "spin-flip" Zeeman slower. Finally, the slowed atoms are captured and loaded into a large-gradient MOT in the trapping chamber.

The vacuum system consists of four main sections: high-temperature oven, transverse cooling, Zeeman slower, and MOT trapping chamber. Each section—except the Zeeman slower—has an ion gauge to monitor the vacuum pressure and a dedicated ion pump. In addition, there is a stainless steel tube (inner diameter 4.6 mm, length 18 cm) that provides differential pumping between the oven and transverse cooling sections [Fig. 4.2 (d)]. The Zeeman slower (inner diameter 1.7 cm, length 54 cm) also serves as a differential pumping

tube between the transverse cooling and MOT sections. One can estimate the conductance of a long round tube by the following equation [65]:

$$C_{\text{tube}} = 12.1\frac{d^3}{l} \tag{4.1}$$

where C_{tube} is in L/s and the diameter d and the length are in cm. Using Eq. 4.1, the differential pumping tube and Zeeman slower give conductance of 68 mL/s and 1.2 L/s, respectively. The ratio of pressures at two sections connected by a differential pumping tube is given by $P_1/P_2 \approx S/C_{tube}$ where P_1 and P_2 are low and high pressures and S is the pumping speed of the pump in the low pressure section. The estimated differential pumping factor is then 810 and 63 respectively for the differential pumping tubing at the transverse cooling stage and Zeeman slower.

4.2 High-temperature oven and transverse cooling

Because Dy has a very high melting point of 1412 °C, a dual-filament, all tantalum high-temperature effusion cell with a water-cooling shroud [Fig. 4.2 (a)] is used to heat mm-sized pieces of Dy. The non-isotopically purified Dy is placed in the tantalum crucible and heated to 1250 °C during typical MOT operation. A near-uniform temperature is achieved by two servos controlling heaters located at the the tip and main part of the oven. The crucible with a 5-mm diameter orifice generates a Dy beam [1]. By attaching a flexible bellow to the oven and controlling it with mechanical positioning stages, the direction of atomic beam is optimized for maximum MOT population [Fig. 4.2 (b)].

Because blackbody radiation from the crucible can heat the UHV chamber walls, a 2.25" diameter tantalum shield is installed around the tip of the differential pumping tube, immediately before the transverse cooling section. Heat propagation through the vacuum system is avoided by continuously water cooling the ConFlat (CF) flange to which the tantalum disc and differential pumping tube are welded. The atomic beam may be shuttered by an in-vacuum, pneumatically controlled tantalum shield positioned a few mm from the crucible orifice.

Typical oven operation at 1250 °C provides a Dy vapor pressure inside the crucible of $\sim 7 \times 10^{-2}$ Torr (Fig. 2.1). We achieve a vacuum of 1.0×10^{-9} Torr at the ion gauge of the oven section with the use of a 75 L/s ion pump. This low pressure is achieved with help from the getter properties of the evaporated Dy on the tantalum disk [66]. Fifteen grams of Dy lasts ∼400 h at 1250 °C operation. A gate valve after the

[1] A newly designed crucible with a 4-mm opening recently has been installed and does not show a significant decrease in the trap population.

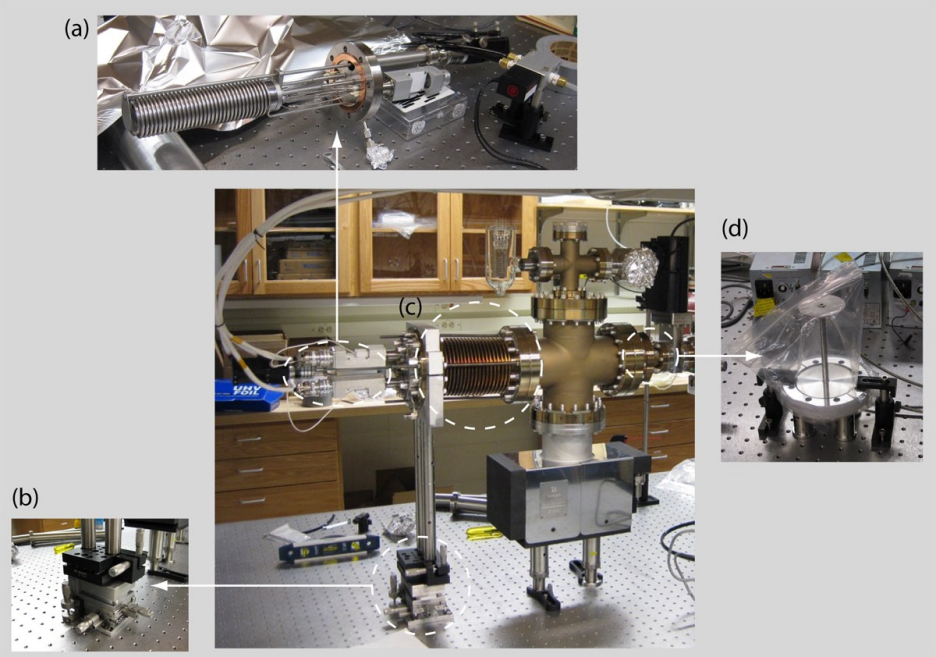

Figure 4.2: The oven section of the vacuum chamber. (a) The high temperature effusion cell custom-made from SVT Associates, Inc. (b) The fine control of the Dy atomic beam direction by a combination of the xyz-translation and angular stages. (c) A flexible bellow enabling the adjustment of the atomic beam direction. (d) The differential pumping tube with a black-body radiation block and a water-cooled flange wrapped in a vinyl bag before ultrasonication.

oven section maintains the vacuum in the rest of system while detaching the oven for the refilling. At the transverse cooling stage, the pressure is 8.2×10^{-11} Torr when continuously evacuated with a 55 L/s ion pump.

A larger atomic beam flux is achieved by transverse cooling the portion of the beam after the differential pumping tube and before the Zeeman slower. A detailed study of Dy transverse cooling appears in Ref. [67]. The transverse cooling beams are elliptically shaped such that they match the atomic beam; their dimensions are 4.4 mm by 18 mm. One beam is oriented horizontally to the the atomic beam and is retroreflected through the chamber via anti-reflection coated windows. The second beam enters the chamber vertically, passes through a quarter-wave plate, into the chamber and is again retroreflected through a quarter-wave plate before entering the chamber. Addition of the quarter-wave plates along the vertical direction enhances transfer efficiency; no such gain is observed for the horizontal branch, presumably since the local magnetic field is nonzero. The cooling beams are all red-detuned from the 421-nm transition by 0.2–0.4 Γ. At a total power of $\sim$200 mW divided among the horizontal and vertical beams, the MOT population is enhanced by up to a factor of 4. Additional power slightly reduces the MOT population, ostensibly due to increased metastable population shelving before the Zeeman slower (and possibly recoil heating). See Sec. 6.3 for more

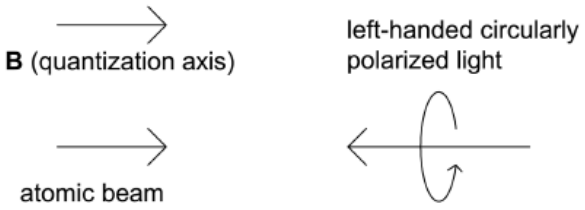

Figure 4.3: The configuration of directions. The local direction of magnetic field (**B**) defines the quantization axis, which varies in space depending on the local field where the atom interacts with light. The sign of σ is determined by the right-hand rule; i.e., when the fingers are curled along the (circular) polarization, if the thumb is aligned with the quantization axis, then it is called σ^+. The left-handed circularly polarized light (σ^+) in the first section (decreasing field) of our spin-flip Zeeman slower is shown here. In our spin-flip Zeeman slower, when passing through the decreasing field section (Section I) the atomic beam experiences σ^+ polarization and transition whereas in the increasing field section (Section II) it experiences σ^- polarization and transition.

details.

4.3 Zeeman slower

When moving atoms as atomic beam are slowed down with laser, laser is detuned by Doppler shift so that the laser is in resonance with a atomic transition. However, as the atoms are slowed down, they are no longer in resonance with the laser. In order to keep the atoms in resonance with laser and continue this slowing process as they are slowed down, we apply the spatially varying magnetic field to compensate this difference. This is called a Zeeman slower. There are three types of Zeeman slower, σ^+ [68], σ^- [69, 70], and spin-flip [65]. σ^+ Zeeman slower has a disadvantage of having slowing laser with frequency very close to magneto-optical trap (MOT, the following stage to Zeeman slower) laser at the exit of the slower. σ^- Zeeman slower also has a disadvantage of having a large field at the end of the slower. With these regards, we have constructed a spin-flip Zeeman slower (see Refs. [70, 65]).

4.3.1 Theory

In the atomic beam deceleration with laser, we have the spontaneous force (slowing force) including Zeeman effect [12] as

$$\mathbf{F}_{\rm sp} = \hbar\mathbf{k}\frac{\bar{I}\Gamma/2}{1+\bar{I}+[2(\Delta+\omega_{\rm D}-\mu B(z)/\hbar)/\Gamma]^2} \tag{4.2}$$

Table 4.1: The survey of oven temperatures from other research groups.

reference	atom	oven temp. [°C]	vapor pressure [Torr]	v_f m/s
Chikkatur [65]	Na	347	8.17×10^{-2}	30 m/s
Boyd [70]	Rb	107	3.64×10^{-4}	20 m/s
Schmidt [71]	Cr	1477	1.81×10^{-1}	N/A
Werner [72], Griesmaier [73]	Cr	1600	1.12	30 m/s
McClelland OE [74]	Er	927	1.53×10^{-5}	N/A
McClelland PRA [75], PRL [37]	Er	1350	4.38×10^{-2}	N/A
McClelland sub-Doppler [76]	Er	1200	4.4×10^{-3}	N/A

where saturation parameter $\bar{I} = I/I_s$, Δ is the Zeeman slowing laser detuning, Doppler shift $\omega_D \equiv -\mathbf{k} \cdot \mathbf{v}$, $\mathbf{v}$ is the velocity of atoms, $\mu = (g_e m_e - g_g m_g)\mu_B$, and $B(z)$ is the magnetic field along z-axis (the axial direction of Zeeman slower). The maximum slowing force [2] occurs when the following resonant condition is satisfied:

$$\Delta + \omega_D - \mu B(z)/\hbar = 0. \tag{4.3}$$

If we assume to have a constant deceleration (Table 2.2), then we can estimate the length [3] of Zeeman slower L to be constructed, using

$$L = \frac{v_f^2 - v_i^2}{2(-\eta a_{max})} \tag{4.4}$$

where v_i and v_f are the initial and final velocity of atoms. Here η is a fudge factor that takes account of spatially varying intensity of Zeeman slower [4]. By plugging the equation $v(z)^2 - v_i^2 = 2(-\eta a_{max})z$ into Eq. 4.3, we have

$$B(z) = \frac{\hbar}{\mu}\left(\Delta + k v_i \sqrt{1 - \frac{2\eta a_{max} z}{v_i^2}}\right) \ , \ 0 \le z \le L. \tag{4.5}$$

4.3.2 Design and Simulation

In order to design the Zeeman slower, we need to determine four variables: v_i, v_f, η, and Δ (Eq. 4.3). v_i is determined by the oven temperature [5]. Our target oven temperature was initially decided by comparing the vapor pressure of other systems (Table 4.1). v_f was decided to be twice v_c (Table 2.2). The fudge factor η $[\equiv \bar{I}/(1+\bar{I})]$, which determines how much intensity of Zeeman slower beam is required, was chosen to be 0.5 in our simulation.

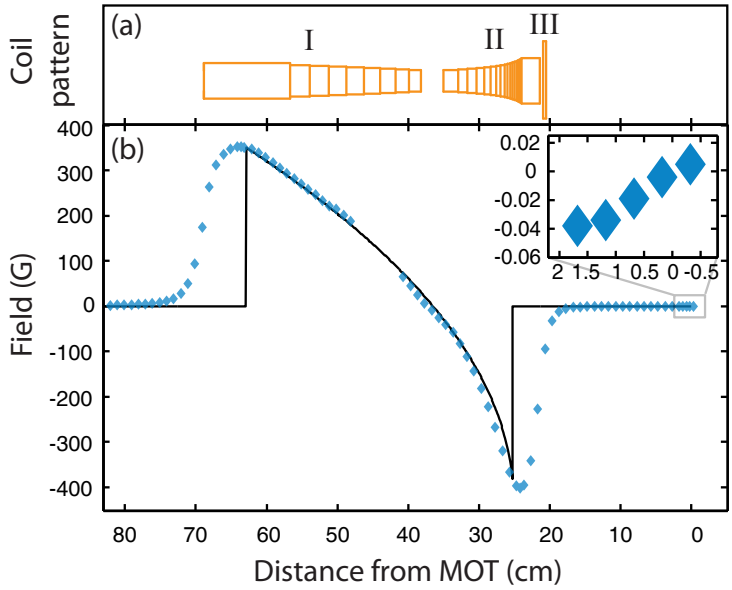

Figure 4.4: Magnetic field profile of Zeeman slower as a function of position away from the center of the trapping chamber. Target (line) and measured ($\diamond$) fields are shown. The profile is measured with 3.01 A in Section I, 3.02 A in Section II, and 40.24 A in Section III. Note that Zeeman slower was designed for 50% maximum deceleration efficiency. The optimal current for MOT production is 1.08 A in Section I, 2.66 A in Section II, and 40.21 A in Section III. Inset shows field zeroing at MOT position.

Before constructing the slower, the magnetic field profile was simulated. In Ref. [70], a C code is written to simulate the desired magnetic field. In our group, this C code was adopted and converted to MATLAB language for our convenience (Appendix A.2). However, one modification made in our simulation is to use continuous winding of coils, while Ref. [70] uses the various current density (various spacing between consecutive windings) as a function of z-axis along the slower, which we thought could be avoided for convenience in the Zeeman slower construction. The computer automatically simulated the necessary field, matching it to the desired field profile (Fig. 4.4).

[2] The moving atoms are in resonance with slowing laser.

[3] This is the length (or range) of magnetic field that actually matters to slow down atoms. Note that the length of constructed Zeeman slower is longer than this.

[4] Zeeman slower beam is focused onto the orifice of crucible.

[5] v_i is the most probable velocity of the atomic beam and equals to $\sqrt{3k_BT/m}$ [12].

Table 4.2: Parts list of Zeeman slower.

company catalog No.	description	quantity
MDC 130008	2-3/4" CF flanges blank	1
MDC 130000	1-1/3" CF flanges blank	1
MDC 480003	stainless steel tube, OD .75", wall thickness .035"	21.107"
Copper and Brass Sales	copper tube, OD 1-1/8", wall thickness 1/16"	19.400"
MWS 18 AWG HAPT	magnet wire with polyester A/I topcoat heavy insulation	500 m
Cotronics Duralco 4525IP – 1	Duralco 500 °F electrically resistant epoxy	1 pint
Von Roll	hollow 4.2 mm square magnet wire	
Speedy Metals 61r6	6" aluminum rod	1"
Speedy Metals 60r6	6" brass rod	2"

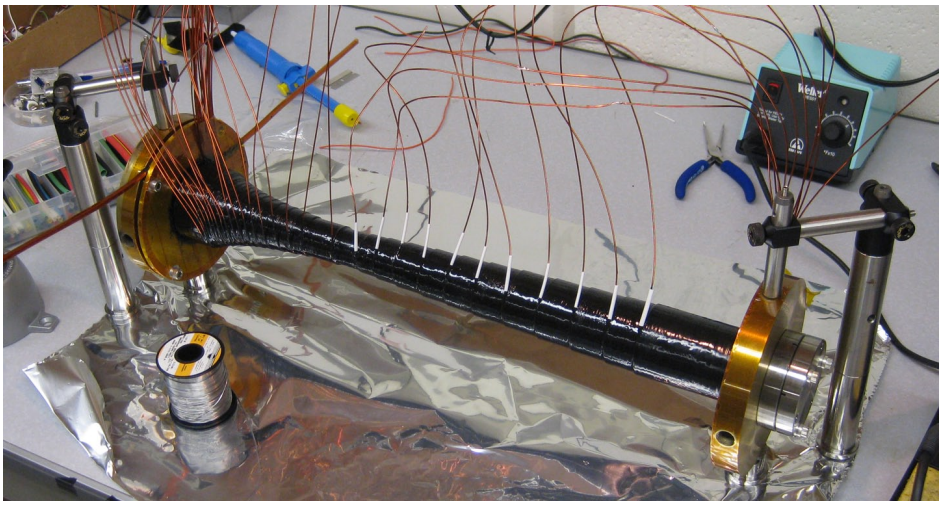

Figure 4.5: The completed Zeeman slower before the water leak was found.

After the field profile simulation was finished, the Zeeman slower was designed (Appendix B.1). Since it would be carrying an electric current of ~ 3 A in Section I & II and 40 A in Section III, water circulation was implemented to the design in order to avoid heating. Two concentric tubes in Zeeman slower were designed to provide a water channel, which efficiently cools the coils.

4.3.3 Construction

All the necessary parts are shown in Table 4.2. Epoxy was applied to every layer of coil, which was necessary because of the following three reasons: (1) The epoxy is electrical insulation, which is an extra protection for the magnet wire. (2) This epoxy application fills up the space so that the next layer of coil can be more easily wound on the more uniform surface. (3) The epoxy holds the previous layer of wire while winding wire. After winding coils for two weeks, Zeeman slower was finally completed (Fig. 4.5).

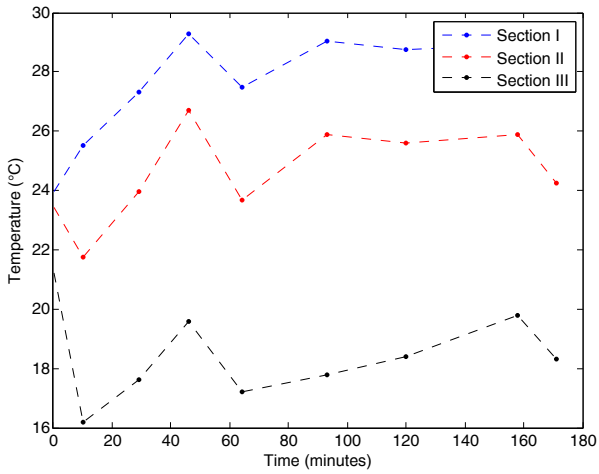

Figure 4.6: The temperature as a function of elapsed time after turning on the Zeeman slower and water cooling.

4.3.4 Water cooling and magnetic field test

Zeeman slower had two things to test on, the magnetic field profile and the water cooling. The magnetic field was characterized by Lakeshore 460 gaussmeter with 3-axis probe. This measurement had a field resolution of 2 mG and an estimated spatial uncertainty of 2 mm.

There happened an unexpected accident, where water channel had a leak. This water leak came from a broken connection between a flange and a tube. Even after attempting to seal this leak with the epoxy, we still were not able to solve the problem and finally decided to wind a water-circulated copper refrigerator tubing around the Zeeman slower externally. The water cooling efficiency was tested with 105 PSI water pressure, and its result is shown in Fig. 4.6. There is no heating observed in the Zeeman slower while running the electric current.

4.3.5 Operation

Up to 1.5 W of Zeeman slower beam power (Fig. 4.9) is used to slow the atomic beam. The laser is detuned by -21 Γ from the 421-nm atomic transition [6] and the beam is focused onto the orifice of the oven crucible.

When we first built the Dy vacuum chamber, we did not have the 45° mirror inside the chamber (Fig. 4.7). Instead, we had a viewport straight through which Zeeman slower beam shines. As the Dy experiment had been running, it was observed that the viewport had been coated by the Dy atomic beam which attenuated the beam (Fig. 4.8). This attenuation was not severe in the trap population, but we decided to install a 45° mirror. The diameter of the slowing laser is 2.5 cm at the vacuum window entrance. As shown in Fig. 4.9(b),

[6] Unless stated, all the values of detuning are with respect to ^{164}Dy atomic transition.

total trapped atom population N_{Total} saturates at ∼1 W of input power; presumably power broadening aids the velocity capture range of the slower.

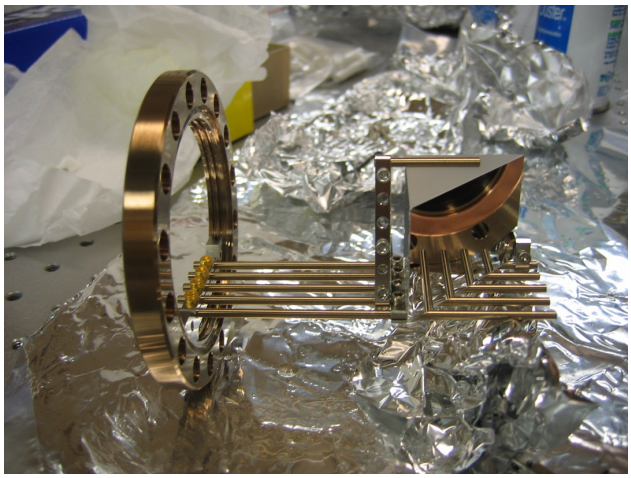

Figure 4.7: 45° mirror and its grabber assembly.

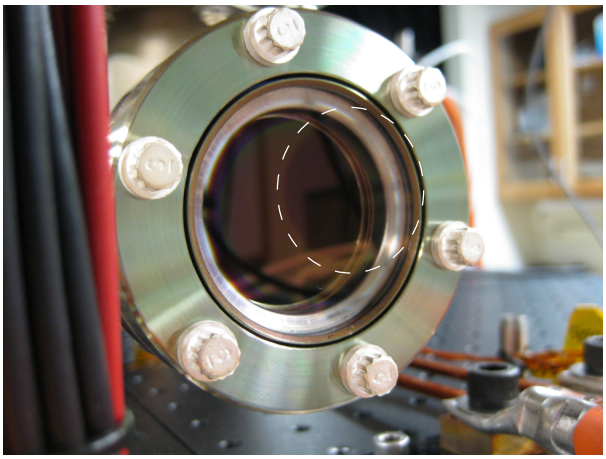

Figure 4.8: The dark region inside the white dashed line was caused by the Dy coating.

4.4 MOT trapping chamber

The MOT employs a three-retroreflected-beam configuration (a six-beam configuration can also be used, with similar results). Each beam is aligned and collimated in free-space with a waist [7] of 1.1 cm, and the MOT typically has a detuning of $\Delta = -1.2\ \Gamma$. A total intensity of 0.17–0.2I_s provides the maximum MOT population, where $I_s \approx 2.7 \times 58\ \text{mW/cm}^2$ [8]. A stainless steel octagon chamber with two 6" diameter CF

[7] All beam waists are reported as a beam $1/e^2$ radius.

[8] The additional factor of 2.7 accounts for approximately isotropic polarization and equally distributed m_J's in the MOT.

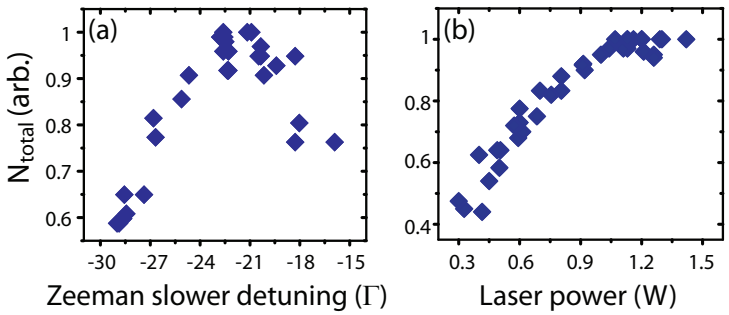

Figure 4.9: MOT population as a function of (a) Zeeman slower detuning and (b) Zeeman slower laser power. Optimal operation occurs for a detuning of -21 Γ. Population saturates above 1 W of laser power. Data for ^{164}Dy (^{163}Dy data is similar).

viewports on top and bottom and six 2.75" CF viewports on the side provide the optical access necessary for the MOT beams and imaging beam. The remaining two CF ports provide access for the atomic beam and counterpropagating Zeeman slower beam.

The magnetic quadrupole field used for both the MOT and magnetic trap [60] is generated from a coil pair in near-anti-Helmholtz configuration. The coils generate $\nabla_z B = 0.69\,\mathrm{G/cm \cdot A}$ along $\hat{z}$, which points along the quadrupole axis of symmetry; each coil has a cross-section of 10 rows ($\hat{z}$) and 7 columns ($\hat{\rho}$) . The coils are water cooled to support the ∼30 A used for the MOT. The electric current is controlled by a servo providing a 440 μs turn-off time. Stray field cancellation coils reduce the residual field to $\leq$ 1.8 mG (see Table. 4.3).

Table 4.3: Characterization of MOT and shim coils.

coil	zero configuration	resistance [Ω]	characteristics
x zero	0.01 V, -0.00 A	0.71	0.74 G/A
y zero	0.50 V, 0.70 A	0.71	0.71 G/A
z zero	0.01 V, 0.01 A	0.55	1.3 G/A
z bias	OFF	0.94	0.14 G/cm/A, 2.1 G/A
Imaging	OFF	0.71	0.74 G/A
ZSlower shim	OFF	0.71	0.74 G/A

We achieve a MOT chamber pressure of typically 1.2×10^{-11} Torr during MOT operation. The vacuum is created with the help of a 75 L/s ion pump and a titanium sublimation pump. We have noticed a lowering of the vacuum pressure from the evaporated Dy after the oven has run for several hours.

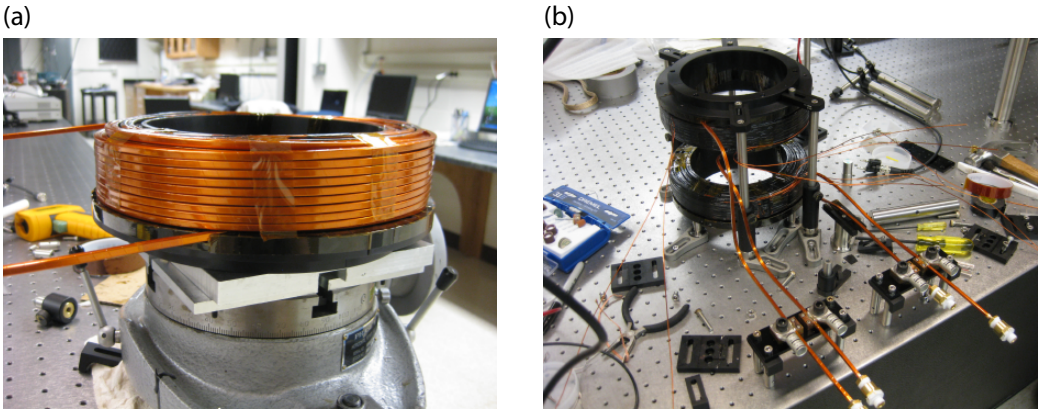

Figure 4.10: The construction of MOT coil. (a) The water-cooled wire was wound by a rotary stage. The bottom half of the MOT coil is shown. (b) Before installing the MOT coil to the vacuum chamber, the magnetic field of the coil was preliminarily characterized.

4.5 Vacuum procedures

Once we received all the necessary vacuum parts from manufacturing companies, we first cleaned them in the ultrasonic cleaner with acetone for about an hour. Then, we repeated the process with methanol for the same time. In order to achieve ultra-high vacuum (UHV) and reduce the final outgassing, we baked out the vacuum parts twice in air and in vacuum (*in situ*). The air bake-out was carried in the much higher temperature at 400 $\sim$ 450 °C, which is fine with most of the vacuum parts except for viewports or valves, and we baked the parts for about a week in a home-made oven made with insulation bricks and heating rods (Fig. 4.11). This air bake-out reduces hydrogen outgassing later when the vacuum chamber is assembled [77]. We controlled the temperature with four AC voltage transformers (Variacs) at north, south, east, and west and continuously monitored to maintain the constant temperature.

After this pre-bake stage was done, we started to assemble the vacuum chamber. In our group, we use only silver-plated vacuum bolts and plate nuts, rather than the vacuum grease and hexagon nuts. The vacuum grease is believed to cause mechanical seizing of the bolts after bake-out. The plate nuts make it so easy to assemble the vacuum chamber only with one wrench. When the vacuum chamber was assembled, it was necessary to plan in advance which part of the vacuum chamber was to be worked on first and where we started to put together.

The various parts of the vacuum chamber have different temperature ratings, which are summarized in Table 4.4 [9].

For the *in-situ* bake-out we did not raise the temperature as high as the air bake-out. The procedure is

[9]The specs may vary depending on the models and are not guaranteed to be up to date

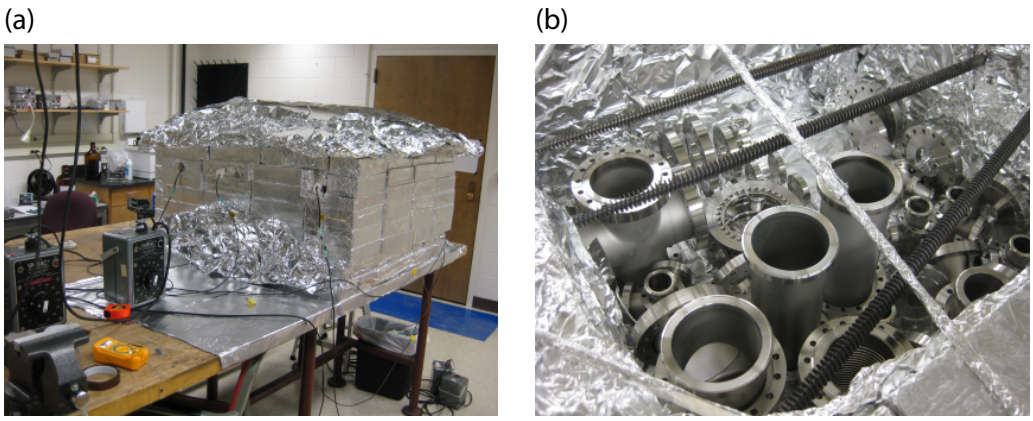

Figure 4.11: Air bake-out procedures. (a) The home-made oven with insulation bricks, three heating rods, a fiberglass top cover, and Variacs. (b) The inside view of the home-made oven showing vacuum parts.

as follows. First, we did the rough pumping using a turbomolecular pump (60 L/min) connected to three ports of the vacuum chamber. After running at normal operation [10] for 30 mins, we reached $\sim 10^{-5}$ Torr. As the first vacuum leak check, we sprayed methanol onto connections of vacuum parts to see if there was a pressure spike. In the meantime, we started to install the heating tapes. In order to heat up the chamber, we first placed thermocouples in various spots, directly on the chamber, to monitor the temperature. Note that viewports and mechanical valves are treated cautiously. One needs to carefully ramp up the temperature of viewports at the rate below those summarized in Table 4.4. The vacuum valves should be heated in a uniform manner because of mechanical parts. The high thermal gradient can cause improper closing when valves are cooled down. After placing thermocouples, the whole chamber was wrapped with UHV aluminum foil, which provides a uniform heat distribution, as tightly as possible but the viewports were wrapped having a air pocket to avoid any scratch. We then wrapped the heating tapes, avoiding any hot spot (overlap of two heating tapes). One thing to be noted is that these heating tapes are made with fiberglass so they can irritate skin. Therefore, it is recommended to work with them wearing latex gloves. For the insulation to the air, we once again wrapped the chamber with the aluminum foil.

We slowly increased the temperature using the heating elements which were connected to Variacs, while avoiding any crack on the viewports. The more Variacs you have, the better control you have over the temperature. We used 7 Variacs for the bake-out, and each had multiple heating tapes. As the temperature was being raised, the pressure was also increased (see Fig. 4.12) because of the increase in outgassing of vacuum parts. Our target temperature was around 200°C. After the temperature was reached, the pressure went down within a few days. When we believed that there would not be not much more improvement in

[10] This normal operation of the turbo pump indicates that there is no major mis-assembly of vacuum flanges.

Table 4.4: Temperature limits of various parts used in the vacuum chamber.

part	description	temperature [°C]	remarks
VAT valve	valve used for rough pump-out	300 only under vacuum	thermal gradient
MDC gate valve		250 open, 200 closed	thermal gradient
viewports	glass	400	10 °C/min ramp
viewports	fused silica	200	25 °C/min ramp
oven	SVT effusion cell	200	
ion gauge	UHV-24p	450	cable: 250 °C
ion pump		220, 350	w/, w/o cables
Ti-Sub pump		400	300 W max power
silver solder	Zeeman slower	640	
Duralco 4525	black epoxy, Zeeman slower	260	
polyester A/I topcoat	Zeeman slower thin wire	200	
welding		1300	
Kapton tape		260	
Teflon tape		280	
plexiglass		80	
polypropylene tube	white, water cooling	90	

pressure, we turned on the ion pumps for the rest of the bake-out process (4 days). Then, we blasted the vacuum chamber with Ti-Sub pump's three filaments. We closed the valves to the turbo pump, and slowly turned down the temperature. Through these vacuum procedures, we achieved a pressure of mid-10^{-12} Torr at the trapping chamber.

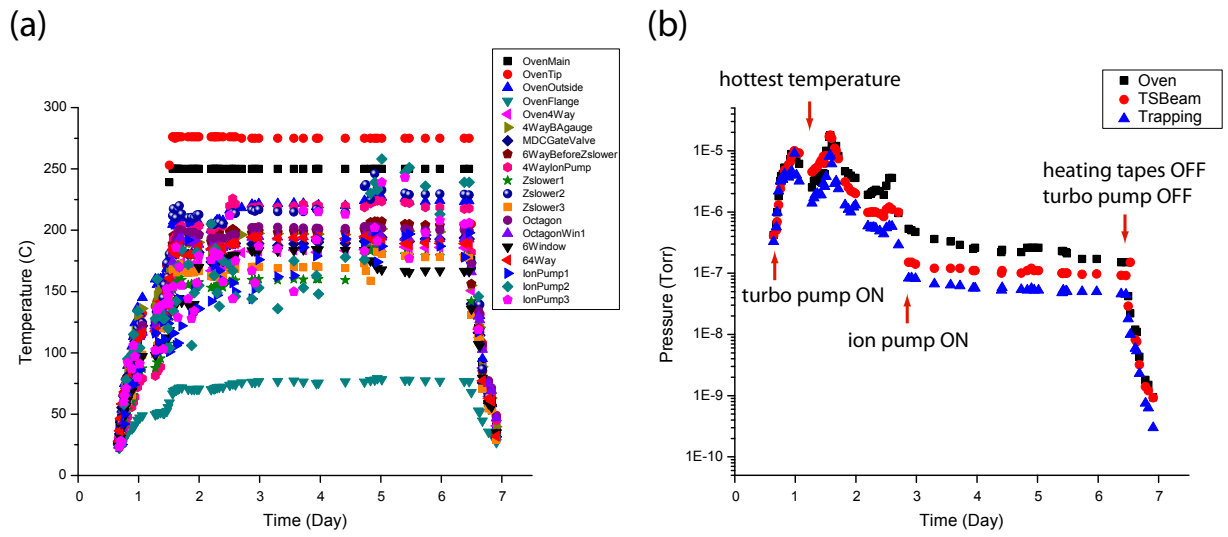

Figure 4.12: (a) Temperature of various spots on the vacuum chamber. (b) Pressure at the oven, transverse cooling, and trapping sections.

Chapter 5

Control and imaging systems

5.1 Computer control

The overall structure of control system is shown in Fig. 5.1(a). Experimental devices such as the magnetic field coil, AOMs and beam shutters require digital and analog signals from experimenters to be triggered for a precise timing. In our apparatus, those signals are provided by NI-DAQ (National Instruments Data Acquisition) boards, which communicate with a computer via C programming language (C-API). At the front user side, although LABView software is fully supported by National Instruments (NI) for users to interface with NI-DAQ, our research group use MATLAB instead to utilize an extensive range of useful and powerful built-in functions. Precise timing of experimental sequence is achieved by utilizing an NI-DAQ on-board clock, and synchronization between different boards is made by connection through a Real-Time System Integration (RTSI) cable.

There are three concepts used in the computer control [Fig. 5.1(b)]: block, subblock, and control parameter. A block corresponds to one experiment defined by a set of control parameters (CPs), for instance, magnetic field gradient or beam intensity (usually used in x-axis of plots). In experiments, it is usual that many runs of a block with a pre-defined set of CPs are executed in order to average and obtain the statistics out of the data. Also, along time axis, a block consists of a series of actions called subblock, such as loading the MOT, turning off the magnetic field, or imaging the atoms.

So far the connection structure of the computer control system and the concepts of the experimental sequence have been described. However, an experimenter follows the steps described below in order to define and execute the experiment summarized in Fig. 5.1(c), and an example code is shown in Appendix A.1.

1. Definition: Sets the experiment time duration, the name, and the sampling rate. Defines devices (analog and digital boards). Adds lines.

2. Compilation: Generates a block (or matrix in MATLAB) consisting of signal data as a function of time. Adds and compiles the generated block to lines.

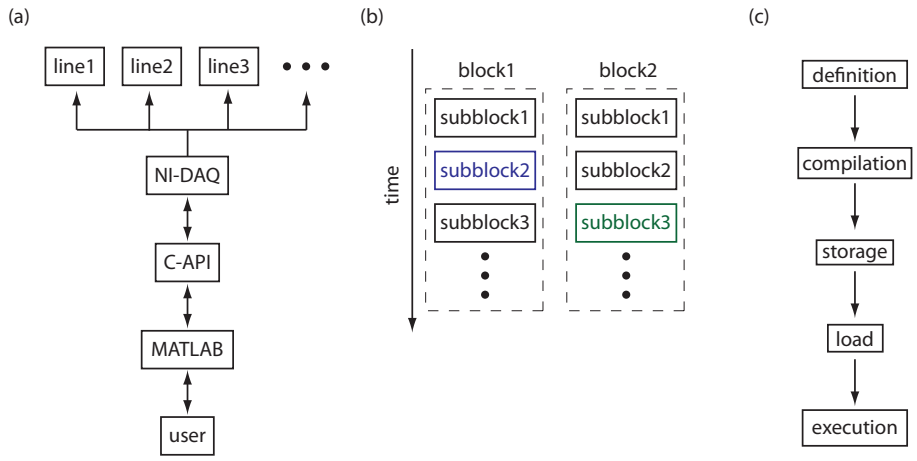

Figure 5.1: The structure of control system. (a) Communication flow from a user to multiple lines that control the experiments. NI-DAQ: National Instruments Data Acquisition boards. API: Application Programming Interface. (b) Diagram of experimental sequence describing concepts of *block* and *subblock*. Different blocks may contain a different *control parameter* as indicated by blue and green. (c) Procedure of running experiments.

3. Storage: Stores the compiled files to a hard drive.

4. Load: Loads the pre-compiled sequence into the buffer memory on the NI-DAQ boards.

5. Execution: Executes the sequence and sends out the digital and analog signals.

Although the computer control system works seemingly without any major technical issue, there are still limits in its capabilities and its possible improvements. First, generating a *single* large matrix [1] in MATLAB uses up all the memory allocated to the program and seems to cause out-of-memory errors in the block definition. This issue is caused by the fact that MATLAB requires a large continuous memory (Ref. [78]). One possible solution that we did was to simply upgrade the computer and add more memory to the operating system, which consequently allocates more memory to MATLAB. The part list for the computer control is tabulated in Table 5.1.

5.2 Image analysis

In order to characterize the cloud of atoms such as density, atom number, and temperature, either fluorescence or absorption imaging method is used. Each of these methods has advantage and disadvantage. Fluorescence imaging is relatively easier to implement than absorption imaging, since a CCD (charge-coupled device) camera can be used with MOT beams. However, the fluorescence can introduce more uncertainty

[1] Columns are the time line and their size is $\tau/d\tau$ where τ is the total experiment time and $d\tau$ is the resolution. Rows are the (device) lines. The size of the matrix that can be as large as $10^6 \times 30$.

Table 5.1: Part list of National Instruments (NI) devices.

catalog No.	description	quantity
778510-01	NI PCI-6733 analog output board	1
184749-02	SH68-68-EP, shielded cable 2 m	1
777643-01	BNC-2110 conn box	1
779672-01	NI PCIe-6536 DIO	1
778592-01	CB-2162 conn box	1
196275-01	SHC68-C68-D4 shielded cable 1 m	1
776249-02	RTSI bus cables for 2 PCI or AT/ISA devices	1

in determination of experimental settings such as solid angle and scattering rate than absorption imaging, absorption imaging is most of time preferred and used for this thesis work.

5.2.1 Absorption imaging

In absorption imaging, when probe light propagates through the cloud of atoms from $x = -\infty$ to $x = +\infty$, its intensity attenuates. This density-dependent attenuation is characterized by the concept of (two-dimensional) optical density (OD). If a cloud of atoms is assumed to have the density distribution $n(x, y, z)$ in the form of Gaussian function with a peak density n_0, then the OD is found to have the following expressions:

$$\mathrm{OD}(y,z) = \sigma(\lambda)\int_{-\infty}^{\infty} n(x,y,z)dx = \sigma(\lambda)n_0\sqrt{2\pi}\sigma_x \exp\left(-\frac{y^2}{2\sigma_y^2} - \frac{z^2}{2\sigma_z^2}\right). \tag{5.1}$$

where the peak OD equals to $\sigma(\lambda)n_0\sqrt{2\pi}\sigma_x$. Using Beer's law $dI = -\sigma(\lambda)n(\mathbf{r})Idx$ where I is the intensity of probe light, the resonant cross-section $\sigma(\lambda) = 3\pi\lambda^2/2$, $n(\mathbf{r})$ is the density of particles, x is the direction of probe light propagation, and λ is the wavelength of the probe light, Eq. 5.1 can be rewritten as

$$\begin{aligned} \mathrm{OD}(y,z) &= -\int_{I(x=-\infty)}^{I(x=\infty)} \frac{dI}{I} \\ &= -\ln\frac{I_{\mathrm{atom}}(y,z) - I_{\mathrm{dark}}(y,z)}{I_{\mathrm{light}}(y,z) - I_{\mathrm{dark}}(y,z)} \end{aligned} \tag{5.2}$$

where I_{atom} is the image with atoms, I_{light} is the image in the absence of atoms but the light, and I_{dark} is the inherent noise image from the CCD in the absence of both of atoms and light. Now we have two expressions of OD (Eqs. 5.1 and 5.2). In reality, OD image is obtained in terms of the intensity on the local pixel (Eq. 5.2).

5.2.2 Image analysis

There are three important physical parameters to characterize a cloud of atoms: the total atom number N, the density n_0, and the temperature T, and this section describes how they are extracted from images. First, we start with a definition of effective volume as

$$\bar{V} \equiv (2\pi)^{3/2}\sigma_x\sigma_y\sigma_z \tag{5.3}$$

where $\sigma_i\,(i = x, y, z)$ is defined as Eq. 5.1 and $\sigma_x = \sigma_y$ in a cylindrically symmetric cloud. Then, by fitting the OD image to Eq. 5.1 and using the assumption of $\sigma_x = \sigma_y$, one can determine n_0 and $N(= n_0\bar{V})$. Instead of the fitting method described above, the other way to determine n_0 and N is the pixel summation method, which is used in my thesis work, because it is a direct measurement. From Eq. 5.1, it is easily seen that by integrating the OD distribution further twice along y and z one can get the total atom number. In practice, CCD captures a value in each discrete pixel, which corresponds to how bright it is along x-axis in space (the brighter it is, the lower the local density is). Processing the three consecutive images with a 300-ms spacing [2] following the principle in Eq. 5.2, one obtains the OD image of $\mathrm{O}D(y, z)$. Because of its discrete nature, instead of continuous integration, one can find the total atom number, using the following expression:

$$N = \frac{A}{\sigma(\lambda)}\sum_{y,z} OD(y, z), \tag{5.4}$$

and A is area of one pixel at the cloud of trapped atoms and $n_0 = N/\bar{V}$. The temperature is measured by dropping the cloud of atoms and measuring the size of its expansion at different drop times [time-of-flight (TOF) measurement]. This TOF measurement requires more than one data point and nonlinearly fits to the following expression [79]:

$$\sigma(t) = \sqrt{\sigma_0^2 + \frac{k_B T}{m}t^2} \tag{5.5}$$

where σ_0 is the *in-situ* size of the cloud, and a typical fit for BMOT is shown in Fig. 5.2.

[2] This is technical due to our CCD camera capability.

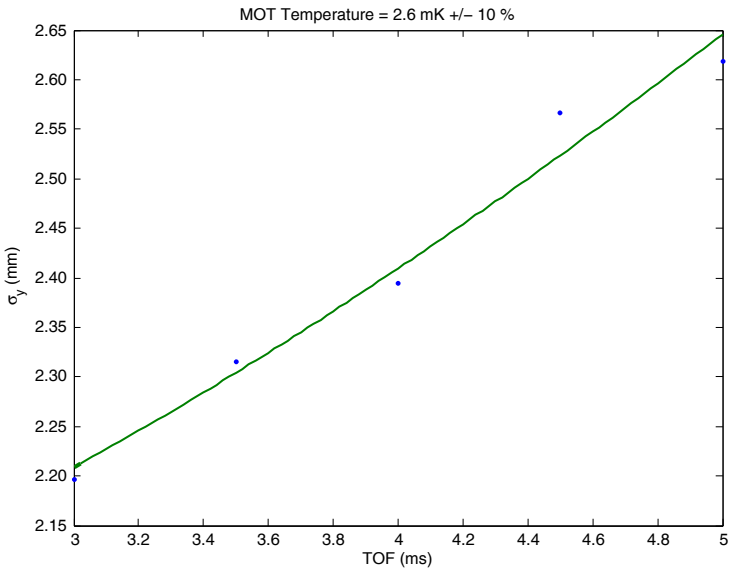

Figure 5.2: Typical TOF plot for BMOT. Data points are randomly taken in order to minimize the systematic drift of the measurements. The fit is done using Eq. 5.5.

5.3 Magnetic field control

Precise magnetic field control is achieved by a servo [Fig. 5.3(a)], using the feedback control, where the high (low) current of quadrupole field (shim coils) is measured by Danfysik 867-200IHF [3] (FW Bell NT-5), and the servo controls $V_{\rm GS}$ (the gate voltage with respect to the grounded source of MOSFET (IXYS IXFN200N07 for the quadrupole field, IRF510 for the shim coils) [4] to maintain the monitored current to the set value 5.3(b), which in the electronics means $V_{\rm control}/V_{\rm probe} = R_1/R_2$. In practice, the ratio R_1/R_2 is chosen as large as possible so that the finest control over the magnetic field is achieved [5]. In Fig. 5.3(b), the probed signal of current is split into two branches: monitor and servo [buffer + PI (proportional and integral)]. The resistance R in the monitor and the buffer is chosen such that the gain in the op-amp (operational amplifier) is unity for convenience. In practice, we usually start with generic values of electric components in the servo, which does not provide the fully optimized performance.

In order to optimize the servo [80], we first start with no integral [no C1 and C2 in Fig. 5.3(b)] and small proportional (small R3), and the proportionality is increased until the response reaches or overshoots the set value by 10% (no ringing in the response). Then, C1 is inserted to further increase the bandwidth, starting

[3] Distributor is GMW Associates.

[4] We install twice the number of MOSFETs with the operation current rating in parallel to reduce the burden to each MOSFET. In addition, MOSFETs are cooled on the water circulated plate.

[5] NI-DAQ has a fixed voltage output resolution and this discrete voltage in a larger ratio of R_1/R_2 gives a better resolution in the field control.

to observe a ringing [6]. C2 is an optional capacitor, cutting off the high frequency if necessary.

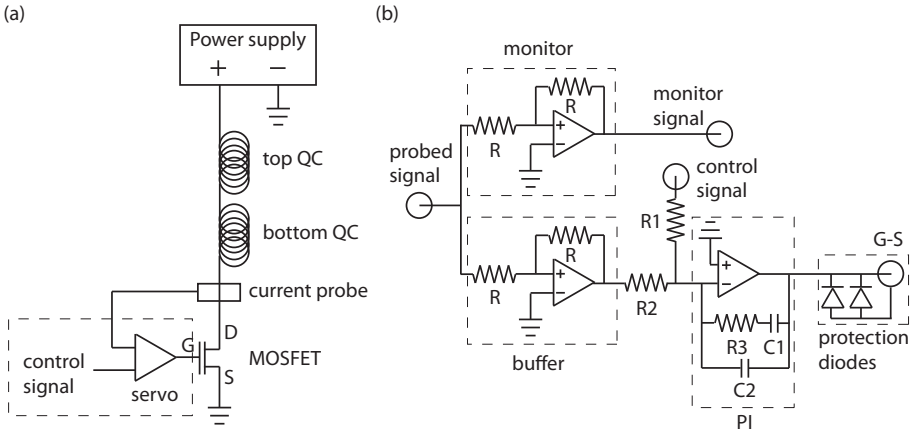

Figure 5.3: Quadrupole coil (QC) control. (a) Schematic of QC feedback. By controlling the gate (G) of MOSFETs, the current through its drain (D) to source (S) is adjusted to the set value. (b) Schematic of electronics of the servo. QC servo parameters after optimization: R = 100 kΩ, R1 = 3 kΩ, R2 = 1 kΩ, R3 = 1 kΩ, C1 = 47 nF, C2 = 100 pF.

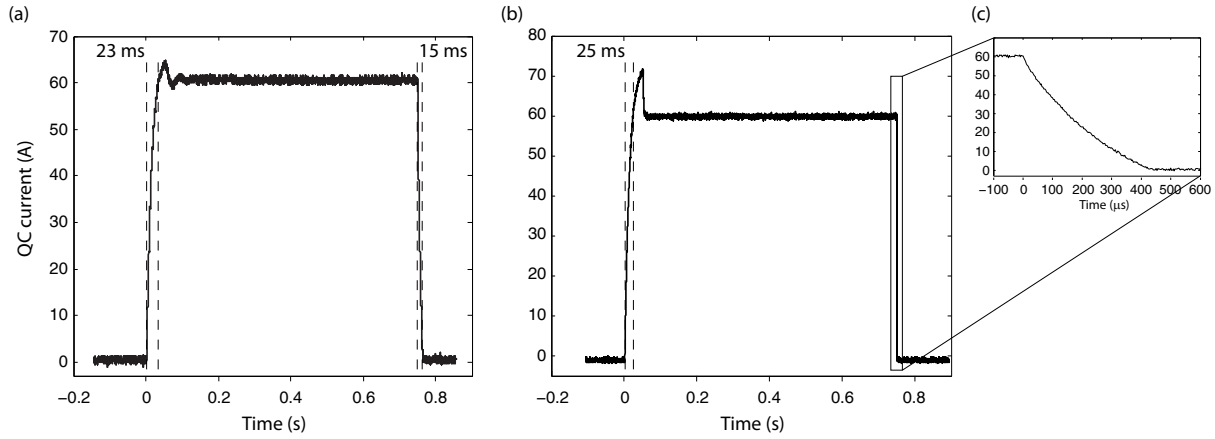

Figure 5.4: QC current response to a pulse signal (a) before and (b) after full optimization. Because the typical timescale of TOF in the MOT characterization is ∼ms, optimization was performed to meet its turn-off time of ≤ 1 ms. (c) Zoomed view at turn-off. 440-μs turn-off time.

[6] In my optimization criterion, as long as the ringing has a frequency lower than the trap frequency and does not exceed the 15% of the set point, the servo is considered to be optimized.

Chapter 6

MOT characteristics

In this chapter I discuss a detailed, semiclassical model and supporting data for how the repumper-less Dy MOT functions. Measurements of the Dy MOT population and temperature versus MOT loading time, intensity, detuning, and magnetic quadrupole field gradient are presented. I also compare Dy MOT characteristics to those of the Er MOT [37, 76].

6.1 MOT number Vs oven temperature

A simple measurement of the MOT population as a function of the oven temperature was done (Fig. 6.1) and shows the near-linear increase in the MOT number as the oven temperature and the vapor pressure increase. If necessary, the oven temperature can be increased to obtain a higher population of trapped atoms without much change in the experimental settings.

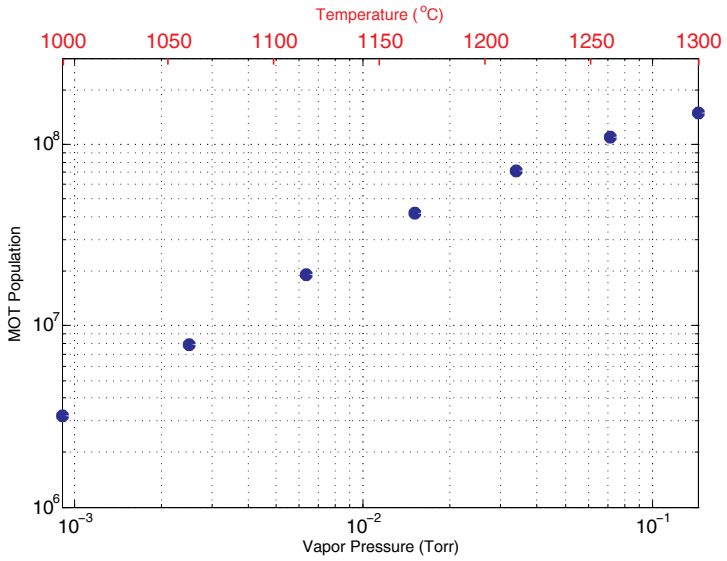

Figure 6.1: MOT population as a function of oven temperature.

6.2 MOT decay and motional dynamics

As mentioned in Chapter 3, the Dy MOT functions without any repumpers due to a population recycling mechanism based on its extraordinarily large magnetic moment. Figure 6.2 depicts a semiclassical rate equation model describing this recycling process. Population is lost from the excited state of the MOT at rate $f_{\rm ex}R_1$—which increases for larger excited state fractions $f_{\rm ex}$—and decays to one of the (possibly many) metastable states (see Fig. 2.2). A fraction of atoms $1-p$ are either in the $m=0$ Zeeman substate or in a strong magnetic field seeking m state and never become confined in the MT. The remaining atoms decay either through a fast decay channel at rate $R_{\rm fast}$ and fractional population $1-q$ or through a slow channel at rate $R_{\rm slow}$. Atoms whose electronic population reaches the ground state are reloaded into the MOT at rate $R_{\rm reload}$, which depends on the total MOT beams' saturation parameter, $s=\bar{I}/(1+(2\Delta/\Gamma)^2)$, where $\bar{I}=I/I_{\rm s}$ and Δ is the detuning from resonance. There must be some loss $R_{\rm loss2}$ from the magnetic trap as the population cascades, but as shown in Ref. [60], spin relaxation loss is $20\times$ slower than the timescales of the measured $R_{\rm fast}$ and $R_{\rm slow}$.

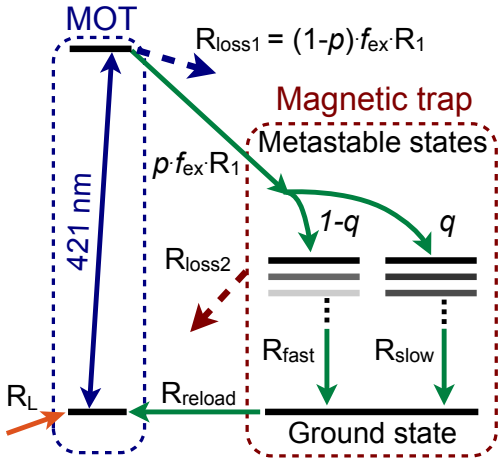

Figure 6.2: Dy MOT recycling and continuously loaded MT schematic.

The diagram in Fig. 6.2 may be represented with the following rate equations:

$$\begin{aligned}
\dot{N}_{\rm MOT} &= R_{\rm reload}N_{\rm MT} - f_{\rm ex}R_1N_{\rm MOT} + R_{\rm L},\\
\dot{N}_{\rm fast} &= (1-q)pf_{\rm ex}R_1N_{\rm MOT} - R_{\rm fast}N_{\rm fast},\\
\dot{N}_{\rm slow} &= qpf_{\rm ex}R_1N_{\rm MOT} - R_{\rm slow}N_{\rm slow},\\
\dot{N}_{\rm MT} &= R_{\rm fast}N_{\rm fast} + R_{\rm slow}N_{\rm slow} - R_{\rm reload}N_{\rm MT},
\end{aligned} \tag{6.1}$$

where $N_{\rm MOT}$, $N_{\rm fast}$, $N_{\rm slow}$, and $N_{\rm MT}$ are the populations of the MOT, fast (slow) metastable state decay

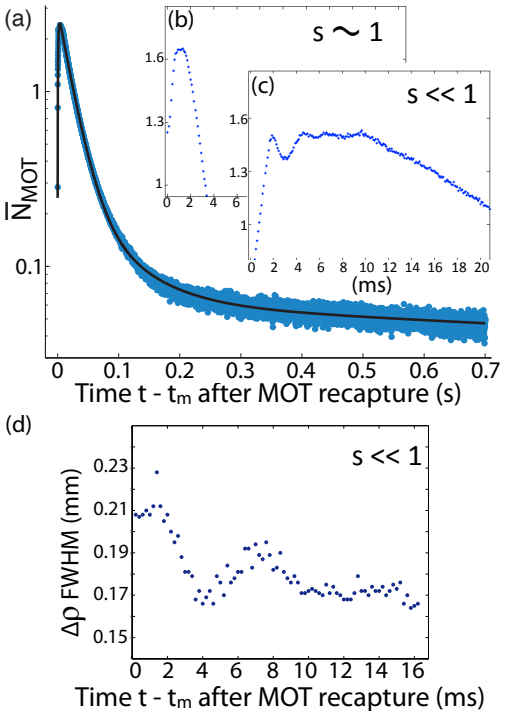

Figure 6.3: (a) Population ratio $\bar{N}_{\rm MOT}$ of recaptured MOT to steady state MOT. Black line is fit using Eqs. 6.1 to $\bar{N}_{\rm MOT}$ with Zeeman slower and atomic beam off, and $t_m = 1$ s delay between steady state MOT and recapture. (b)-(c) Oscillations in fluorescence at the peak of the recaptured MOT population appear for MOT beam saturation parameters $s \ll 1$. (d) The Dy MOT operates in the mechanically underdamped regime, as shown by breathing mode oscillations, and the photon scattering rate seems to be correlated with cloud diameter.

channel, and ground state MT, respectively, and $R_{\rm L}$ is the loading rate from the Zeeman slower. Fits of these rate equations to MOT population decay curves allow the determination of all free parameters for both the ^{164}Dy boson and the ^{163}Dy fermion:

$$\begin{aligned} \left[R_1^{163}, R_{\rm fast}^{163}, R_{\rm slow}^{163}\right] &= [1170(20), 19(2), 1.5(1)]\ {\rm s}^{-1}, \\ \left[R_1^{164}, R_{\rm fast}^{164}, R_{\rm slow}^{164}\right] &= [1700(100), 29(1), 2.3(1)]\ {\rm s}^{-1}, \\ [p, q] &= [0.82(1), 0.73(1)], \end{aligned} \tag{6.2}$$

where p and q for the two isotopes are equal within error.

An example of the Dy MOT decay and fit are shown in Fig. 6.3(a). To obtain these data, we collect MOT fluorescence using a 200-mm 2" aspherical lens and focus it through a pinhole, using a 60-mm 2" aspherical lens. The light is then collected on an amplified, high-bandwidth PIN photodetector. We load the MOT for 2–3 s to reach steady-state population before extinguishing, at $t_m = 0$, the MOT beams, the Zeeman slower beam, and the atomic beam (via the in-vacuum shutter). Note, the magnetic quadrupole

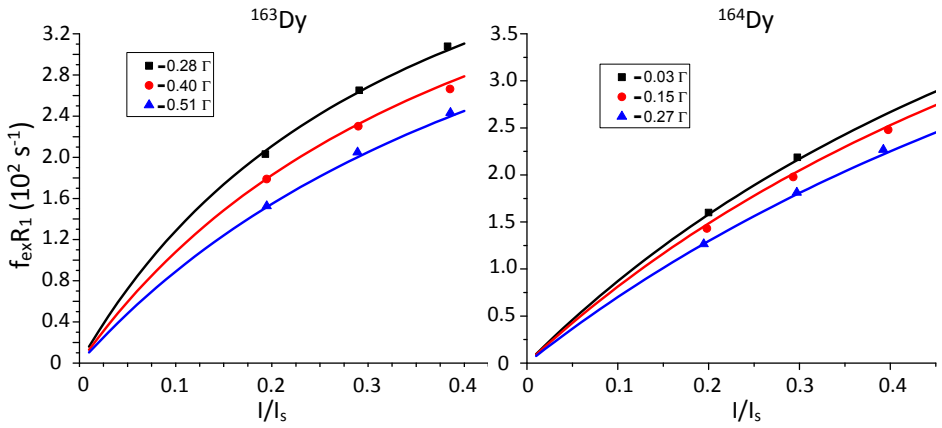

Figure 6.4: Fits of Eq. 6.4 to $f_{ex}R_1$ versus $\bar{I} = I/I_s$ and Δ for both fermionic ^{163}Dy and bosonic ^{164}Dy. A simultaneous fit to the nine (eight) data points for ^{163}Dy (^{164}Dy) allow the extraction of R_1 from the product $f_{ex}R_1$ via Eq. 6.4.

field remains on throughout this experiment, providing confinement for weak-field seeking metastable and ground state atoms. We wait for $t_m = 1$ s before recapturing the MOT by turning on the MOT beams, but we leave the Zeeman slower beam and atom beam off to ensure there is no external loading of the MOT during the measurement, i.e., $R_L = 0$. Shorter t_m times bias the results due to ill-defined initial conditions: we fit the data assuming nearly all population has decayed to the ground state, allowing us to set $N_{\rm MOT} = N_{\rm fast} = N_{\rm slow} = 0$ at $t - t_m = 0$, while $N_{\rm MT}$ is left free to vary and is normalized to the steady state MOT fluorescence signal. Fluorescence traces as in Fig. 6.3(a) are averaged over 16 sequential runs on a digital oscilloscope.

We noticed an oscillation of the recaptured MOT fluorescence near peak signal when operating at small saturation parameter $s \ll 1$. The pinhole does not restrict numerical aperture so severely that the modulation is simply due to a loss of photons when the cloud is large. This oscillation disappears when the intensity of the MOT light is increased and/or the detuning of the beams decreased to the point that $s \sim 1$ [compare Figs. 6.3(b) and (c)]. Data corrupted with oscillations could not be fit using Eqs. 6.1, so all the data used to extract R_1, $R_{\rm fast}$, $R_{\rm slow}$, p, and q were taken near $s \sim 1$.

A possible explanation of these fluorescence oscillations lies in the motional dynamics of the Dy MOT. Most MOTs, e.g., of Rb, are solidly in the overdamped regime, meaning they have a ratio $\alpha = \Gamma_{\rm MOT}/\omega_{\rm MOT} > 1$ of the MOT's optical damping rate $\Gamma_{\rm MOT} = \beta/2m$ to the trap oscillation frequency $\omega_{\rm MOT} = \sqrt{\kappa/m}$. In a 1D treatment, the damping coefficient β is

$$\beta = \frac{8\hbar k^2 |\Delta| \bar{I}}{\Gamma(1 + \bar{I} + (2\Delta/\Gamma)^2)^2}, \tag{6.3}$$

where k is the wavenumber of the MOT light, mass is m, and the spring constant is $\kappa = \mu' \nabla B \beta / \hbar k$ [12]. In this latter expression, $\mu' \equiv (g_e m_e - g_g m_g)\mu_B$, where g_i and m_i are the g factors [1] and Zeeman substates of the ground and excited levels. For a typical Rb MOT operated to maximize trap population, $\alpha_{\rm Rb} \gtrsim 7$. For the Er MOT with the parameters used in Ref. [37], $\alpha_{\rm Er} = 1.3$ and oscillations where not reported [81]. However, the Dy MOT, when operated in the regime that maximizes trapped atom population (see Sec. 6.6), is just in the underdamped regime $\alpha_{\rm Dy} = 0.8$. The origin of this lower α lies in the combination of the larger (smaller) m, k, Γ, μ' and ∇B ($\bar{I}$ and Δ/Γ) parameters in the highly magnetic Dy MOT versus typical Rb MOTs.

Indeed, $\alpha_{\rm Dy} = 0.8$ corresponds to an oscillation period of 4 ms, and a measurement of the breathing mode of the Dy MOT, shown in Fig. 6.3(d), shows a damped oscillation with a period of ~ 6 ms after the magnetic quadrupole field gradient is decreased by a factor of 2 at $t_m = 0$. We find that the breathing mode period scales $\propto \sqrt{\nabla B}$. The similar periods support the notion that fluorescence is modulated by the motion of the atoms during recapture. (Atoms confined in the magnetic trap, from which the MOT is recaptured, possess a different spatial profile from those in the MOT.) The breathing mode should have a period half that of the trap oscillation frequency, indicating that the actual $\alpha_{\rm Dy}$ is just slightly below unity; a 3D numerical MOT calculation incorporating magnetostatic forces on the highly magnetic Dy could better estimate α for these system parameters. We conjecture that optical pumping, Zeeman shifts, and spin polarization near the cloud edge—as well as modulation of optical density—could change the effective photon scattering rate as the cloud expands and contracts. To avoid complications caused by these motional dynamics, we operate the MOT in the overdamped regime of $s \sim 1$ for the decay rate measurements.

To extract MOT decay rates R_1 from the product $f_{ex}R_1$—as well as to obtain better error estimates of the other model parameters—we repeat the measurement in Fig. 6.3(a) for several combinations of $\bar{I}$ and Δ. MOTs of bosonic ^{164}Dy and fermionic ^{163}Dy are studied in a similar manner to investigate differences in decay dynamics due to hyperfine structure. Figure 6.4 shows the set of data simultaneously fit to the function

$$R(I, \Delta) = R_1 \bar{I} / (2 + 2\bar{I} + 2(2\Delta/\Gamma)^2), \tag{6.4}$$

where $R = f_{\rm ex} R_1$. Using this method to determine R_1, we arrive at the rates in Eq. 6.2 for these two Dy isotopes.

Detailed simulations of the decay channels still seem beyond the reach of tractable calculations, but such calculations might be able to employ the following simplification for modeling the fast decay channel. The shortest possible decay channel (the fast channel), must involve at minimum two metastable levels due to

[1] For Dy, $g_g = 1.24$ and $g_e = 1.22$.

the need to switch parity from odd (421-nm exited state) to even to odd before decaying back to the even parity ground state. Recent calculations reported in Ref. [82] indicate that the lifetimes for the 1001-nm and 1322-nm levels are $2\pi \cdot [53, 23]$ s^{-1}, respectively, which indicates that rapid decay to these levels followed by a delay given by their lifetime is a likely candidate for the 20–30 s^{-1} fast decay channel. For the slow decay channel, it is possible that the population becomes shelved in a longer-lived state that decays to ground or an intermediate state via a non-electric dipole (E1) allowed transition. Small-energy-difference decays could also contribute to the slow channel.

The large q parameter—73% of the atoms decay through the slow versus fast channel—serves a very useful purpose in providing a continuously loaded magnetic reservoir of metastable atoms for the MOT. Indeed, data presented in Ref. [60] show that 2.5× (^{164}Dy) to 3.5× (^{163}Dy) more atoms are in the metastable MT plus MOT than in the visible MOT alone, resulting in a maximum number of laser cooled and trapped atoms nearing 5×10^8 for the Dy system. This is reminiscent of the continuously loaded MT in the Cr system [83] that provides sufficiently large samples, 10^8 atoms, to enable Bose-condensation of Cr [21].

6.3 MOT population versus isotope

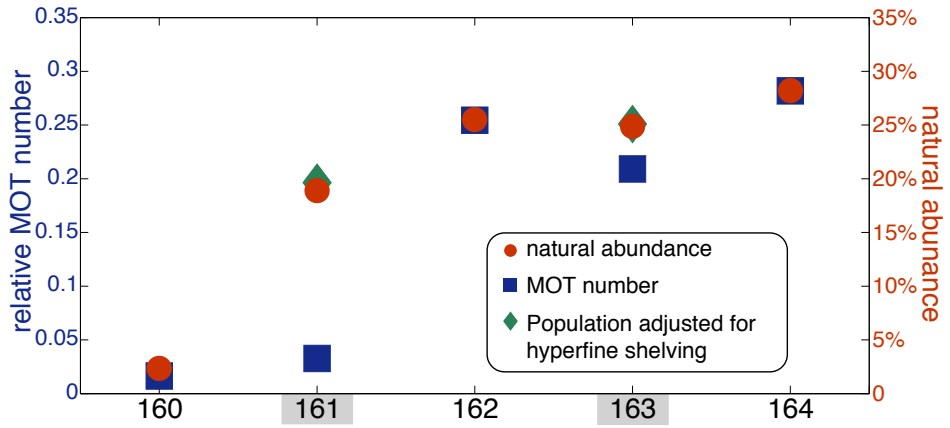

Figure 6.5: Comparison of relative MOT population to natural isotope abundance for the five highest abundance isotopes of Dy. Relative population is computed as the fraction of an isotope's MOT population out of the sum total MOT population for all the isotopes. The fermions, ^{163}Dy and ^{161}Dy are highlighted in grey. The green diamonds are the MOT populations for the fermions when multiplied by 6/5 for ^{163}Dy and 6 for ^{161}Dy to account for poor optical pumping of the six hyperfine states during laser cooling. See text for details.

Figure 6.5 plots the maximum MOT population obtained for each stable isotope (except for low 0.1% abundance ^{158}Dy) along with the natural abundance of the isotope. To facilitate comparisons to natural abundance, each MOT population is normalized by the sum of all the MOT populations of the isotopes

(for the fermionic isotopes, the MOT population is adjusted for hyperfine shelving; see below). The bosonic MOTs have relative populations very close to their proportion of the natural abundance. However, the fermionic isotopes ^{163}Dy and ^{161}Dy have populations that are 84.0% and 17.3% their natural abundances, respectively. We try, in the following, to argue why repumper-less fermionic MOTs form and are observed with these population ratios.

Unlike the bosons, the two fermions have non-zero nuclear spin $I = 5/2$, and the opposite sign of the nuclear magnetic moment between the two isotopes results in oppositely ordered hyperfine levels with respect to F versus energy [see Fig. 2.3]. With a total electronic angular momentum of $J = 8$, the isotopes have six hyperfine states, $F = 11/2$ to $21/2$ and $F' = 13/2$ to $23/2$, in their ground and 421-nm excited states, respectively. Without hyperfine repumpers (a repumper is necessary for Rb and Cs MOTs), one would expect that no MOT could form on the $F = 21/2 \rightarrow F' = 23/2$ cycling transition due to rapid decay to $F < 21/2$ states. Alkalis such as Rb and Cs, however, have smaller hyperfine splittings (<270 MHz) between their highest F' excited states than does ^{163}Dy, whose splitting is 2.11 GHz. However, such an explanation—that scattering to the lower F hyperfine state is slower due to the larger detuning—ignores the 6× shorter lifetime of the Dy excited state. Together this implies a depumping rate similar to Rb and Cs. The crucial difference, however, lies in the fact that the hyperfine splittings in the ground and excited states of Dy are nearly matched, whereas for Rb and Cs, they are different by more than 25×. Thus for Dy, the trapping light near-resonant with the $F = 21/2 \rightarrow F' = 23/2$ cycling transition also serves as an efficient repumper for the $F = 19/2 \rightarrow F' = 21/2$ transition, thereby preventing complete population shelving into dark states.

A full modeling of the intra-hyperfine manifold population transfer as the atoms progress through the transverse cooling, Zeeman slower, and MOT stages is beyond the scope of this paper, but we can make a simplified estimate of the $F = 21/2$ state decay and repumping rates in each of the stages. The atoms spend roughly 20 μs in the transverse cooling beams, scatter $\sim 8 \times 10^4$ photons from the $F' = 23/2$ state in the Zeeman slower, and spend, on average, 25 ms in the MOT scattering photons from the 421-nm excited state before decaying to metastable states. Accounting for laser intensities (power broadening) and detunings, this implies that for ^{163}Dy atoms, <1 photon is off-resonantly scattered on the $F' = 21/2$ state (which can decay to $F = 19/2$) in the transverse cooling stage, while nearly 100 and 50 are scattered in the Zeeman slower and MOT stages, respectively. However, the repumping rates in the Zeeman slower and MOT stages back to the $F' = 21/2$ state from $F = 19/2$ are only a factor of two smaller than the cycling transition scattering rate and are 570× and 1300× faster than the decay rates to $F = 19/2$, respectively: in very little time the population is repumped back into the cycling transition. No secondary laser is necessary to repump

the ^{163}Dy system.

The situation is different in the ^{161}Dy system due to the hyperfine structure inversion and the nearer detuning of hyperfine levels at the larger F and F' end of the spectrum. In the transverse cooling, Zeeman slowing, and MOT stages, approximately 10, 3×10^3, and 2×10^3 photons are off-resonantly scattered to the $F' = 21/2$ state, respectively; the ^{161}Dy system off-resonantly scatters more than in the ^{163}Dy system. Nevertheless, the repumping rates are within a factor of two of the depumping decay rates, and atoms are repumped nearly as fast as they are depumped from the cycling transition. Again, a repumper-less MOT is able to be formed with ^{161}Dy despite its multitude of hyperfine levels. Reference [37] reported a fermionic ^{167}Er MOT ($I = 7/2$), which we suspect works in a similar manner.

This leaves open the question why we observe as much as 84% of the natural abundance of ^{163}Dy, while as little as 17% of ^{161}Dy. The hyperfine population in Dy arriving from the high-temperature oven is likely to be distributed with a bias toward the higher-multiplicity large-F states. This may contribute to the large MOT population in ^{163}Dy, but ^{161}Dy's much lower population may be due to the competing effect of less-efficient optical pumping and repumping to the $F = 21/2$ state.

Optical pumping of population into the $F = 21/2$ state must occur before the Zeeman slower detunes the non-$F = 21/2$ state atoms away from resonance. Indeed, we have already seen that the 421-nm laser tuned to the $F = 21/2 \rightarrow F' = 23/2$ transition can pump atoms out of the $F = 19/2$ state on relatively short time scales, and we now estimate all the relative $F \rightarrow F' = F + 1$ effective scattering rates to examine the repumping efficiency from the $F \leq 19/2$ states:

$$\begin{aligned} \left[F^{163}_{21/2} : F^{163}_{19/2} : F^{163}_{17/2} : F^{163}_{15/2} : F^{163}_{13/2} : F^{163}_{11/2}\right] = \\ [1000 : 500 : 70 : 20 : 6 : 3]\,. \\ \left[F^{161}_{21/2} : F^{161}_{19/2} : F^{161}_{17/2} : F^{161}_{15/2} : F^{161}_{13/2} : F^{161}_{11/2}\right] = \\ [1000 : 20 : 7 : 5 : 5 : 7] \quad . \end{aligned} \tag{6.5}$$

These ratios are proportional to the number of photons scattered from the $F = 21/2 \rightarrow F' = 23/2$ cycling transition, denoted $F^{163,161}_{21/2}$ and normalized to $F^{163}_{21/2} = F^{161}_{21/2} = 1000$, during the time the atoms transit the transverse cooling stage and first 5 cm of the Zeeman slower [2]. $F^{163}_{11/2} = 3$ for the $F = 11/2 \rightarrow F' = 13/2$ transition corresponds to roughly 20 scattered photons in our experiment, assuming that the population is already optically pumped to the $m_g = F$ state [3]. This is merely an upper bound to the number of photons a non-polarized sample would scatter since $m_g < F \rightarrow m_e < F + 1$ transitions have smaller transition

[2] This is roughly the portion of the Zeeman slower in which the fast oven beam is in resonance with the slowing laser.

[3] The transition strengths are nearly equal for the five stretched-state σ_+ transitions.

strengths than the cycling transition $m_g = F \rightarrow m_e = F + 1$.

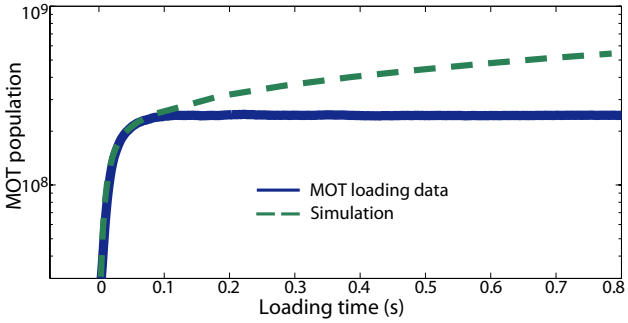

Figure 6.6: Typical MOT loading data as a function of time (blue, solid curve). The trapped atom population is detected by a photodetector recording MOT fluorescence. The Zeeman slower laser and atom beam shutters open at $t = 0$. The green (long-dash) curve is a simulation using Eqs. 6.1 and 6.2.

A striking difference between the isotopes is evident. The single 421-nm $F = 21/2 \rightarrow F' = 23/2$ laser scatters many more photons from $F < 21/2$ states in ^{163}Dy than in ^{161}Dy. This leads to much more efficient optical pumping to the $F = 21/2$ state in ^{163}Dy. We conjecture that this is why 84% of the ^{163}Dy are trapped but only 17% of the ^{161}Dy. Coincidentally, these percentages are close—within experimental error—to 5/6 and 1/6, respectively. It is tempting—but probably an oversimplification—to conclude that for ^{163}Dy, all levels but the lowest F state is optically pumped to $F = 21/2$. The case of ^{161}Dy is certainly more complicated: while it is likely that $F \leq 17/2$ states are never efficiently pumped to $F = 19/2$ (let alone $F = 21/2$), the initially larger F population from the oven should lead to larger populations than 17%. A possible explanation lies in the inversion of the hyperfine state energy hierarchy between the two isotopes. This causes Doppler shifts in atoms not optimally decelerated in the Zeeman slower to move closer to (further from) resonance with the $F < 21/2$ levels in ^{163}Dy (^{161}Dy). This contributes to a more efficient slowing—and therefore more efficient MOT loading—of ^{163}Dy versus ^{161}Dy atoms.

A thorough optical pumping simulation including all the hyperfine levels and the actual experimental parameters and geometry could better address these questions. A repumping laser system is under construction to identify into which $F < 21/2$ states population accumulate, and we suggest that only one repumper on the $F = 11/2 \rightarrow F' = 13/2$ transition for ^{163}Dy would be necessary to capture the full fraction of this isotope's natural abundance in the MOT. Reference [67] presents other repumping schemes.

6.4 MOT loading

Figure 6.6 shows a typical MOT population loading curve after the Zeeman slower laser and atomic beam are unblocked at $t = 0$. The ^{164}Dy MOT population—proportional to the MOT florescence (atoms in the

metastable MT remain dark)—rises to a steady state of 2.5×10^8 within 50 ms (blue line). A simulation of Eqs. 6.1 predicts, however, that within 5 s the population should reach a steady state 5× larger (green dashed line). The Dy MOT population limit could arise from light-induced two-body collisions as in the Cr MOT [84]. Suppression of the $R_{\rm reload}$ term in Eqs. 6.1 mimics the experimental data for a loading rate of $R_{\rm L} \approx 10^{10}$ s^{-1}. Reproduction of the loading data requires a small $R_{\rm reload}$ in simulations, while fits to decay data such as in Fig. 6.3(a) require $R_{\rm reload}$ to be of the order 10^3 s^{-1}. A main difference between the MOT loading and MOT decay experiments is the presence of the 1 W Zeeman slowing beam, which could enhance light-induced losses of Dy and reduce $R_{\rm reload}$. Another possibility involves 2-photon ionization loss while the atoms are in the metastable states (twice the cooling light energy is close to the ionization potential) [4].

6.5 Comparison to Er MOT decay dynamics

As discussed earlier, the Er MOT did not exhibit underdamped oscillations in MOT decay florescence, which we believe is due to its smaller magnetic moment. Other differences between the Dy and Er MOT decay dynamics are presented in this section.

The analysis of the Er MOT decay dynamics [37] accounted for loss only via an $R_{\rm lossMT}$ term (i.e., $p \equiv 1$) and with only one decay channel through the metastable states ($q \equiv 0$) [5]. Allowing q to be nonzero (thus introducing two decay channels), provides a much better fit to the Dy MOT decay data. The Er apparatus had a 1000× worse vacuum pressure, which might have obscured the long-time tail of the MOT decay and prevented a measurement of a second metastable state decay channel.

Perhaps coincidentally, the bosons ^{164}Dy and ^{168}Er have the same, within experimental error, rate of decay to metastable states ∼1700 s^{-1} and branching ratios. Interestingly, the fermion ^{163}Dy, which possesses hyperfine structure, has a significantly smaller decay rate 1170 s^{-1} as well as shorter metastable decay rates compared to ^{164}Dy. While it is not clear why all the ^{164}Dy decay rates are ∼1.5× larger than those for ^{163}Dy, the existence of hyperfine structure in ^{163}Dy likely plays a role.

As shown in Ref. [60], ^{163}Dy's smaller decay rates translate into larger steady state metastable MT populations, which help to enhance its total trapped population. The large q and small $R_{\rm slow}$ that provide population enhancement in the metastable MT was also seen in MOT-loaded magnetic traps of ^{168}Er, albeit to a lesser extent due to poor lifetimes from a high vacuum [76]. The majority of Dy atoms decay through a slower metastable channel (2.3 (1.5) s^{-1} versus 4.5 s^{-1} for ^{168}Er). However, 27% decay through the fast channel at rates 6× (4×) larger than $R_{\rm slow}$ in ^{164}Dy (^{163}Dy). From simulations of Eqs. 1 in Ref. [37] and

[4] The transition strengths are nearly equal for the five stretched-state σ_+ transitions.

[5] Including an $R_{\rm lossMT}$ loss term is equivalent to allowing p to be non-unity, but the latter can be more physically motivated.

Eqs. 6.1 here, one can see that the measured rates imply that the Er metastable MT reservoir could hold several times more atoms as Dy's; however, the severity of Er's magnetic trap inelastic loss rates are not yet known. Dy collisions limited the metastable trap population to 80% [60] of the maximum achievable given by the rates in Eqs. 6.2.

6.6 MOT population and temperature

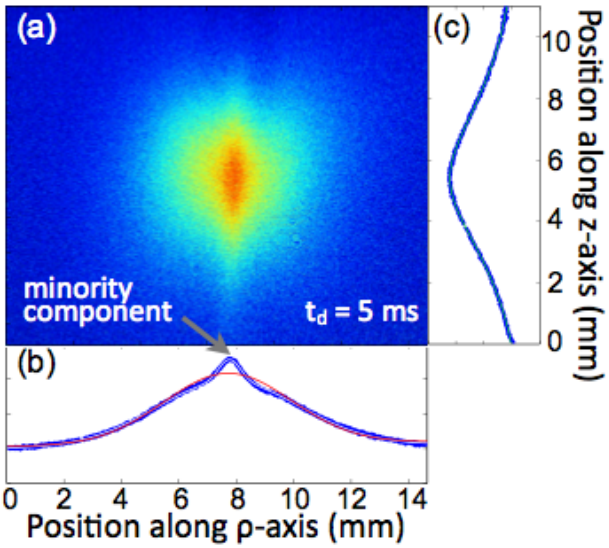

Figure 6.7: (a) Time-of-flight absorption image of ^{164}Dy MOT at $t_d = 5$ ms; MOT fields are extinguished at $t_d = 0$. Intensity integrations along (b) z and (c) ρ-directions. Grey arrow points to region of minority component for this MOT. (b) Double-Gaussian fit (white line) to MOT expansion (the red line is a single-Gaussian which results in a poor fit). The majority component (hot outer cloud) is defined as the atoms contributing to the broader Gaussian, while atoms in the narrower Gaussian comprise the minority component. (c) The anisotropically cooled stripe hampers majority component temperature measurements in the z-direction. The origin and temperature characteristics of the minority component are studied in Ref. [11].

As reported in Ref. [60], when the power between the three sets of MOT beams are mismatched, the Dy MOT can exhibit a sub-Doppler cooled core, which depending on the details of the power balancing, can be anisotropic in its temperature distribution. However, the number of atoms in this ultracold core is typically less than 10% of the total MOT population. I describe more details on this minority component in Chapter 7, and instead present in this chapter the temperature and population of the majority component of the Dy MOT as a function of MOT beam intensity $\bar{I}$, detuning Δ/Γ, and quadrupole gradient ∇_zB (see Fig. 6.8). Data presented here are typical of the majority component in all Dy MOTs.

To distinguish the hotter majority from the colder minority component—when it exists—we fit a double-temperature distribution to the time-of-flight expansions of the MOT (Fig. 6.7(b) and Fig. 4 in Ref. [60]).

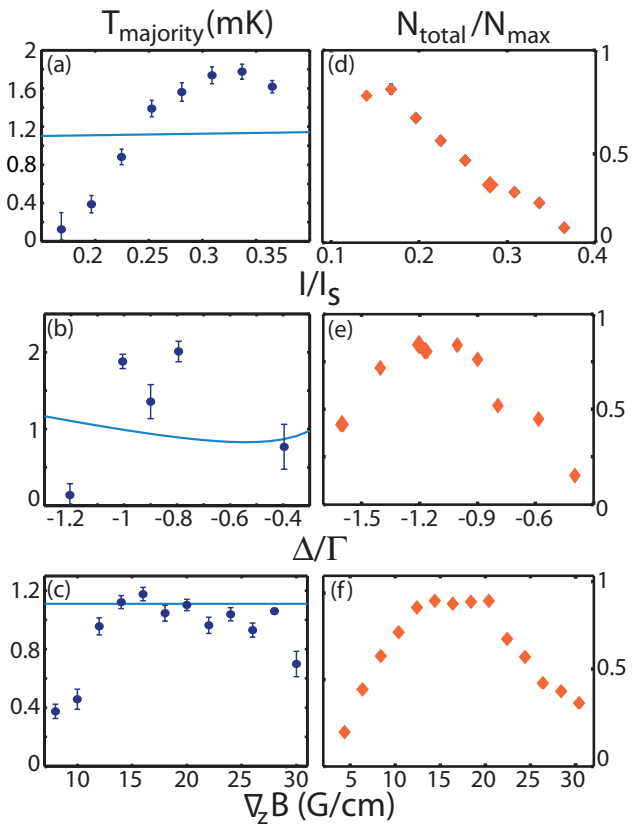

Figure 6.8: (a–c) Temperature characterization of the majority component of the Dy MOT versus intensity $\bar{I} = I/I_s$, detuning Δ/Γ, and MOT magnetic field gradient ∇_zB (∇_ρB $\approx \nabla_z$B/2). Data are the temperatures of the MOT in the ρ direction (quadrupole plane of symmetry, gravity points in the $-z$ direction). Light blue curves are plots of Eq. 6.6 for the following parameters: (a,d) $\Delta/\Gamma = -1.2$, ∇_zB = 20 G/cm; (b,e) $\bar{I} = 0.17$, ∇_zB = 20 G/cm; (c,f) $\bar{I} = 0.20$, $\Delta/\Gamma = -1$. (d–f) Total number of atoms (major plus minor component) versus $\bar{I}$, Δ/Γ, and ∇_zB. The typical visible MOT maximum population is $N_{\max} = 2 \times 10^8$. Maximum density of $\sim 10^{10}$ cm^{-3} occurs for: $\bar{I} = 0.33$ in (a,d); $\Delta/\Gamma = -1$ in (b,e); and ∇_zB = 20 G/cm in (c,f).

Figure 6.8 shows a compilation of temperature and population data of the majority component. In both Figs. 6.7 and 6.8, the data were taken for a ratio of MOT powers in the z versus ρ directions of $I_z/I_\rho \approx 1$ and $\bar{I} > 0.2$ ($I = I_z + 2I_\rho$). This results in a MOT with a vertically oriented, anisotropically sub-Doppler cooled core. The majority component data with the MOT beams set to $I_z/I_\rho \leq 1$ and $\bar{I} > 0.2$ are discussed here, since it is in this regime that we obtain the most populous MOTs.

The major component temperature T_{majority} data in the ρ-direction are shown along with plots of Eq. 6.6, the temperature T_{D} from simplified Doppler cooling theory [12]:

$$T_{\text{D}} = \frac{\hbar\Gamma}{4k_B} \frac{1 + \bar{I} + (2\Delta/\Gamma)^2}{2|\Delta|/\Gamma}. \tag{6.6}$$

The Doppler cooling limit for Dy on the 421-nm transition is 770 μK, and for the $\bar{I}$ and Δ/Γ's typically used in the experiment, the Doppler cooling temperature is $\sim$1 mK. The prolate MOT T_{majority} data are close to that predicted by Doppler cooling theory for large s (large $\bar{I}$, small Δ/Γ) and high gradients. However, T_{majority} of the atoms at small s and small gradient is below the Doppler limit.

The low gradient and low saturation data are consistent with the several hundred μK temperatures of the Er MOT [76]. One-dimensional numerical sub-Doppler cooling simulations presented in Ref. [76] indicate that population-wide MOT sub-Doppler cooling arises from the near-equal Landé g factors in Er's ground and excited states $\Delta g_{\mathrm{Er}} = 0.004$, which means that the MOT magnetic field Zeeman shifts the ground and excited m_J levels by nearly equal energies. Spherically symmetric intra-MOT sub-Doppler cooling has been observed in the cores of MOTs of more commonly used atoms (e.g., Rb [85]), but unlike Er, the majority of atoms are at hotter Doppler temperatures. The Dy MOT—which also possesses a near-degeneracy of g factors on the 421-nm line [6]—also exhibits population-wide MOT sub-Doppler cooling like the Er MOT, which is confirmed in 1D numerical simulations [81, 60]. Unlike Er, however, the Dy MOT population assumes a double-temperature distribution at large s and $\nabla_z B$.

In contrast to the Er MOT, we have also observed anisotropic sub-Doppler cooling to much lower temperatures—down to 10 μK—in the central cores of the Dy MOTs. This phenomenon of ultracold stripes, shown in Fig. 6.7, disappears at low MOT beam intensities—coincident with the appearance of sub-Doppler cooling in the majority component of the Dy MOT. The minority stripe components are typically 1-10% the population of the entire MOT, and as such are no more populous than 10^6 to 10^7 atoms (see Fig. 6.7). The Er MOT presented in Ref. [76] contained no more than 2×10^5 atoms, and the largest Er MOT to date contained 1.6×10^6 atoms [37]. We conjecture that the Er population was limited by low Zeeman slower power, which was <100 mW [81]. More populous Er MOTs might also exhibit double temperature distributions when larger MOT beam power is employed. The origin of this anisotropically sub-Doppler cooled minority component located in the Dy MOT core is explored in detail in Chapter 7 [11].

[6] $\delta g_{\mathrm{Dy}} = 0.022$ ($\delta g_{\mathrm{Dy}}/g_{\mathrm{Dy}} = 1.7\%$), which is 5.5$\times$ larger than Er's on its MOT transition, but 7.7$\times$ less than Rb's.

Chapter 7

Anisotropic sub-Doppler laser cooling

Sub-Doppler cooling [86, 87] in an optical molasses [12] subsequent to MOT capture is a crucial step toward creating degenerate gases in, e.g., alkali atomic systems such as Rb and Cs. Sub-Doppler mechanisms fail to cool the majority of atoms [88] inside these MOT because the ground state g_g factor is substantially different from the excited state's (for ^{87}Rb, $\Delta g/g_g = 34\%$) [89, 90]; population-wide σ^+-σ^- sub-Doppler cooling breaks down in the longitudinal magnetic fields of a typical MOT. Notable exceptions are the ^{87}Sr [91] system, which has a negligible g_g, and the highly magnetic lanthanides Er (7 μ_B) and Dy, whose repumperless MOTs [37, 60] operate on optical transitions whose ground and excited state g factors are the same to within 0.3% (1.7%) for Er (Dy) [7]. At low MOT beam intensity, both the Er and Dy MOTs exhibit *in-situ*, population-wide sub-Doppler cooling [76, 59]. The minimum temperatures > 200 μK are, however, more than 10 times larger than typical Rb and Cs optical molasses sub-Doppler cooled temperatures, but similar to the ^{87}Sr MOT's [91].

I describe in this chapter a novel sub-Doppler cooling mechanism in the highly magnetic Dy MOT system that we first reported in Refs. [60, 59]. These observations were expanded with additional measurements and a plausible explanation for this phenomenon is done based on the theory of velocity selective resonances (VSR) in a highly magnetic gas [92, 13, 93]. While this mechanism only cools a small fraction of the atoms to $\sim$10 μK ultracold temperatures, its existence is a first example of novel behavior arising from laser cooling the most magnetic atom.

7.1 Dy MOT regimes

In this chapter, all pairs of MOT beams are well-aligned in mutual orthogonality and retroflection [1]. I focus on the bosonic isotope ^{164}Dy with zero nuclear spin I, but similar results were observed in the fermionic ^{163}Dy MOT ($I = 5/2$).

The Dy MOT can be formed in two classes of operation, striped and stripeless, and the striped MOT

[1] Boundaries between the striped MOT regimes are blurred with substantial beam misalignment.

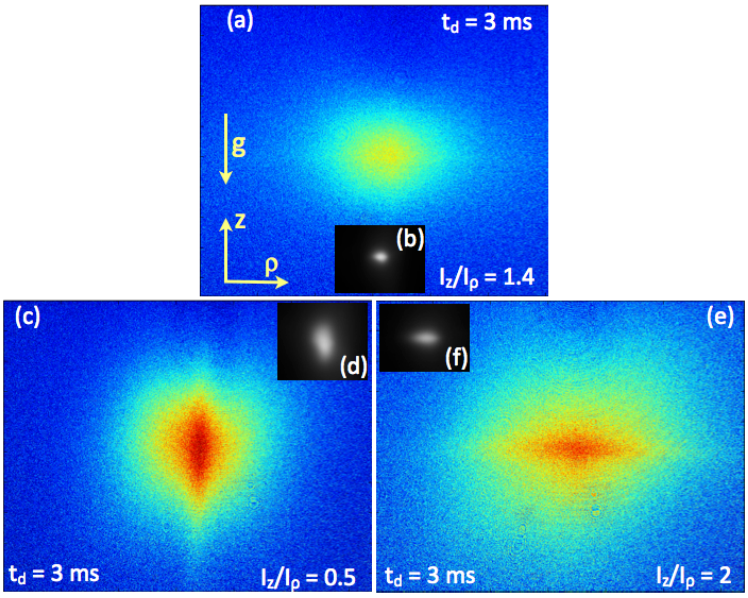

Figure 7.1: (a,c,e) Time-of-flight expansions and (b,d,f) *in-situ* images of the three striped MOT regimes exhibiting anisotropically sub-Doppler cooled cores. (a,b) Symmetric/cross MOT with $I_z/I_\rho = 1.4$. Notice the faint vertical and horizontal stripes crossing at the MOT center. (c,d) Prolate striped MOT with $I_z/I_\rho = 0.5$. (e,f) Oblate striped MOT with $I_z/I_\rho = 2$.

can be further classified into three regimes. The stripeless Dy MOT is similar to the Er MOT reported in Ref. [76], in that the majority of atoms are sub-Doppler cooled to ∼200 μK. These MOTs are obtained at low intensity $\bar{I} = I_t/I_s \lesssim 0.17$, where $I_t = I_z + 2I_\rho$ is the total MOT intensity and I_s is the saturation intensity in the MOT; $I_s = 2.7 \times 58$ mW/cm^2 [59]. Moreover, the stripeless ^{164}Dy MOT forms at low MOT magnetic quadrupole field $\nabla_z B \lesssim 12$ G/cm, where $\nabla_z B \approx 2\nabla_\rho B$ and $\hat{z}$ and $\hat{\rho}$ are the directions along the quadrupole's axis and plane of symmetry, respectively.

The temperature and density distributions in the three striped MOT regimes differ greatly from the stripeless MOT in time-of-flight. The temperature distribution is anisotropic at large $\bar{I}$ and $\nabla_z B$, and Fig. 7.1 shows characteristic time-of-flight expansions of the striped Dy MOT. In these images, MOT beams and the quadrupole field are extinguished at $t_d = 0$, and the *in-situ* images are taken at $t_d < 0$. We observe in time-of-flight a low-population core surrounded by a more populous and hotter outer shell, and we designate the group of outer shell atoms as the majority while the inner core as the minority. Parametrically driving the MOT could reveal the minority component's *in-situ* size [85].

Typical high-population MOTs are formed with $\bar{I} = 0.2$ and $\delta = \Delta/\Gamma = -1.2$, where Δ is the detuning from the $\Gamma = 2\pi \cdot 32$ MHz, 421-nm transition. These typical MOT parameters correspond to T_{D}'s of approximately 1 mK. At large MOT intensity, the temperature of the majority component T_{majority} is consistent with T_{D}, as shown in the $\hat{\rho}$ (orange square) data of Fig. 7.2 and as discussed in detail in Ref. [59].

The T_{majority} data in $\hat{\rho}$ are derived from the broader of the two Gaussians employed to fit intensity versus ρ [see Fig. 7.3(b)]. Temperature data for $\hat{z}$ (blue diamond) are derived from single Gaussian fits to intensity versus z [see Fig. 7.3(c)].

The larger $\hat{z}$ temperature data are a result of the convolution of the Doppler-cooled majority temperatures with the minority velocity distribution along $\hat{z}$ (described in Sec. 7.5). It is noted that T_{majority} data in $\hat{z}$ below $\bar{I} \approx 0.17$ are roughly equal to the $\hat{\rho}$ data and are not shown. This low-intensity region in which the temperature is below T_{D} is also the regime in which stripes cease to appear in time-of-flight expansions: In the Dy system, the stripeless regime is the low-intensity limit of the striped regime. We note that the sub-Doppler-cooled Er MOT, which did not exhibit stripes, was also operated below $\bar{I} = 0.17$ in the data of Ref. [76].

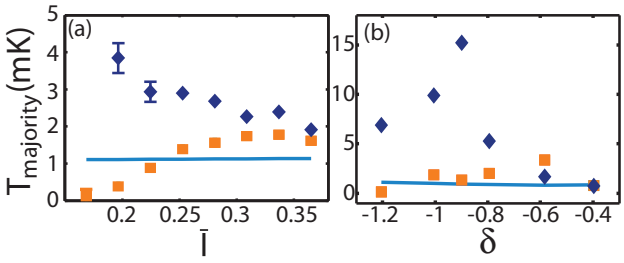

Figure 7.2: Temperature characterization of the prolate striped Dy MOT [Fig. 7.1(c)] versus normalized intensity $\bar{I}$ and detuning δ. The orange squares (blue diamonds) are the T_{majority} along $\hat{\rho}$ ($\hat{z}$). Light blue curves show the Doppler cooling limit [12] for the MOTs' parameters: (a) $\delta = -1.2$, $\nabla_z \text{B} = 20$ G/cm; (b) $\bar{I} = 0.2$, $\nabla_z \text{B} = 20$ G/cm.

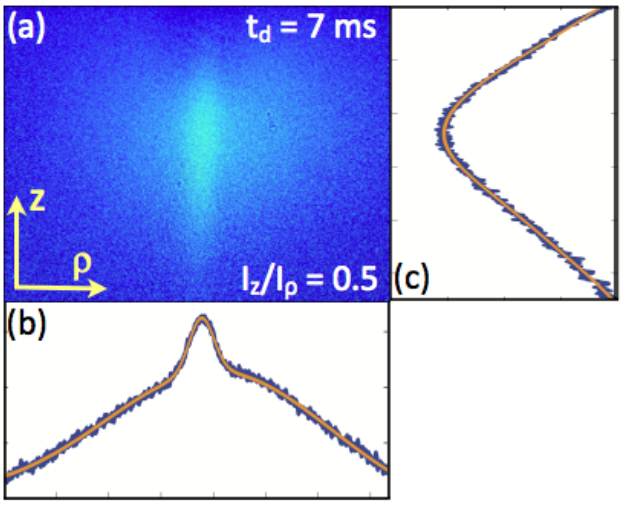

Figure 7.3: Prolate striped MOT time-of-flight expansion at $t_d = 7$ ms. (a) Double-Gaussian fit, orange line, along a $\hat{z}$ intensity integration. (b) Intensity integration along $\hat{\rho}$ is consistent with a single Gaussian.

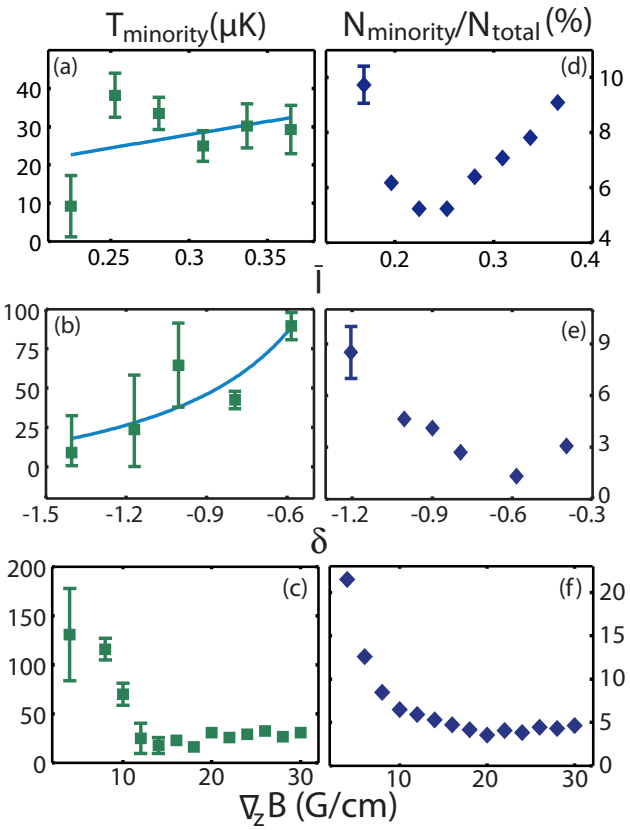

Figure 7.4: T_{minority} in $\hat{\rho}$ of the prolate striped MOT $I_z/I_\rho = 0.5$ [Fig. 7.1(c)]. Blue curves in (a, b) are fits of the data to the sub-Doppler cooling expression Eq. 7.1. (d–f) Fractional population of the minority component. (a, d) $\delta = -1.2$, ∇_zB = 20 G/cm; (b, e) $\bar{I} = 0.2$, ∇_zB = 20 G/cm; (c, f) $\bar{I} = 0.2$, $\delta = -1$.

7.2 Quantitative characterization of anisotropic sub-Doppler cooling

The minority component assumes either a prolate, symmetric/cross, or oblate shape in time-of-flight depending on whether the ratio of intensity in the MOT beams I_z/I_ρ is <1.4, ∼1.4, or >1.4 (see Fig. 7.1). MOT populations are largest in the prolate, $I_z/I_\rho < 1.4$ regime, whose minority component temperature T_{minority} and ratio of minority atoms to total MOT population $N_{\text{minority}}/N_{\text{total}}$ is shown in Fig. 7.4 [2].

T_{minority} and N_{minority} are extracted from a double-Gaussian fit to time-of-fight data such as that presented in Fig. 7.3. The temperature of the minority component is anisoptropic, leading to the vertical stripe structure in Figs. 7.1(c) and 7.3(a). The temperature in $\hat{z}$ is hotter than the majority atoms [see the $\hat{z}$ (blue diamond) data of Fig. 7.2], while the temperature in $\hat{\rho}$ is sub-Doppler cooled to temperatures as low as 10 μK, a factor of 10 less than the sub-Doppler temperatures observed in the stripeless regime. The $\hat{\rho}$ temper-

[2]Careful characterization of minority population and temperature for MOTs with $I_z/I_\rho > 1$ was inhibited by increased MOT population instability in these regimes.

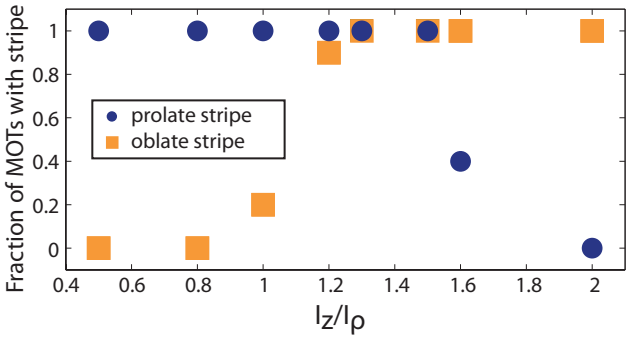

Figure 7.5: Visibility of stripe regimes—prolate, symmetric/cross, and oblate—versus the ratio of MOT beam power I_z/I_ρ. Data are taken for $\bar{I} = 0.22(0.01)$, $\delta = -1$, and $\nabla_z B = 20$ G/cm. All stripes vanish below $\bar{I}_c = 0.17$. Each point is the average of 10 MOT realizations with $t_d = 6.5$ ms.

ature of the minority component in the prolate MOT is well described by a 1D characteristic sub-Doppler scaling law [88, 91]:

$$T_\rho = T_0 + C_{\sigma^+\sigma^-}\frac{\hbar\Gamma\bar{I}}{2k_B|\delta|} \tag{7.1}$$

where $[C_{\sigma^+\sigma^-}] = [0.1(0.09), 0.55(0.20)]$ in Figs. 7.4(a) and (b), respectively. These values of $[C_{\sigma^+\sigma^-}]$ are consistent with those of the Er MOT [76], but smaller than in the ^{87}Sr MOT [91]. However, T_0 is <10 μK in both fits and is $\sim 10\times$ lower than in the Er, Sr, and stripeless Dy MOTs. This 2D, anisotropic sub-Doppler cooling—in the case of the oblate striped MOT, 1D [3]—is a much more effective cooling mechanism than the one found in the stripeless sub-Doppler-cooled Er and Dy MOTs.

7.3 Transition between prolate and oblate striped MOTs

The transition is explored between the prolate and oblate striped Dy MOT in Fig. 7.5. As the MOT's I_z/I_ρ ratio is tuned from 0.5 to 2, the occurrence—defined by visibility of the double-Gaussian structure above image noise—of stripes in a series of 10 realizations is noted. The fraction of these images exhibiting a stripe structure is noted in Fig. 7.5. Below $I_z/I_\rho = 1$, the prolate stripe is always observed, while the oblate stripe is always observed above $I_z/I_\rho = 2$. There is a smooth transition between the regimes in which successive MOT realizations may exhibit either a prolate or oblate stripe, and no explanation can be offered for either the smoothness of the transitions or their slight asymmetry.

Between these two regimes there is a third: We most often observe a spherically symmetric minority component in the range of I_z/I_ρ from 1.3 to 1.5. This is the regime of the power balanced and aligned MOT discussed in Ref. [60] and is less populous, though more dense, than the prolate regime. A prolate–

[3] We observe, by imaging in the ρ-plane, that the oblate stripe is indeed azimuthally symmetric.

oblate cross is observed [see Fig. 7.3(a)] in the region around the critical ratio $I_r^c = I_z/I_\rho = 1.4$, though not reproducibly, and the spherically symmetric core is more prevalent.

No stripes are observed below the critical intensity $\bar{I}_c < 0.17$, which coincides with the appearance of majority component (population-wide) sub-Doppler cooling [see Fig. 7.2]. The prolate stripe is observed to vanish below a critical $\nabla_z B_c \approx 12$ G/cm, as shown in Fig. 7.4(c). The minority component temperature and stripe population fraction rise below $\nabla_z B_c$—which may be interpreted as a blending of the minority and majority components—until the MOT is firmly in the stripeless, isotropically sub-Doppler-cooled regime.

7.4 Velocity selective resonance picture of anisotropic sub-Doppler cooling

This section presents a qualitative explanation of the anisotropic sub-Doppler cooling mechanism. Two properties of Dy are crucial to this explication: its large magnetic moment and the near equal ground and excited state g factors ($\Delta g \approx 0$) of the cooling transition. The latter is important for the following reason. In standard σ^+-σ^- sub-Doppler cooling, the linear optical polarization serves as the quantization axis since the optical pumping rate γ_p is typically greater than the Larmor precession rate $\omega_L = \mu \nabla B r/\hbar$, where r is the distance of the atom from the magnetic quadrupole's center. In low magnetic fields, ground state population imbalance due to non-adiabatic following of the quantization axis induces the differential scattering of σ-light, which then leads to sub-Doppler cooling to zero mean velocity [86, 12]. However, in large longitudinal magnetic fields, a non-zero Δg results in an "unlocking" of the Doppler and sub-Doppler-cooling mechanisms, and sample temperatures rise to the Doppler-cooling limit. (Hence the failure of population-wide sub-Doppler cooling in, e.g., Rb MOTs and the need for field nulling to the mG level when sub-Doppler cooling in Rb optical molasseses.) By contrast, Er and Dy MOTs remain sub-Doppler-cooled [76, 59] despite the large intra-MOT magnetic fields because $\Delta g \approx 0$ in both. This explains the existence of intra-MOT sub-Doppler cooling in Er and Dy, but not the origin of the anisotropic regime.

The anisotropic sub-Doppler-cooling mechanism may be qualitatively understood in the velocity-selective resonance (VSR) picture of 1D sub-Doppler cooling [92] when augmented to account for large magnetic fields, or equivalently, large magnetic moments [4]. In this picture, most types of sub-Doppler cooling may be understood as arising from the momentum transfer by a coherent two-photon process between ground state sub-levels (labeled by m) [92]. These coherent Raman transitions can occur when the difference in

[4] A review of such a treatment is beyond the scope of the current work. However, Refs. [13, 93] provide detailed analytical and numerical calculations of the force and diffusion felt by atoms in various relative orientations of (a large) magnetic field and σ^+ - σ^- light; see Figs. 4 and 5 and Table 1 of Ref. [13] and Fig. 4 of [93] for force versus velocity plots and additional details of the VSR cases invoked in Chapter 7.4

Doppler-shifted frequencies of counterpropagating light beams seen by an atom equals the Zeeman shift between levels separated by $\Delta m = n$. Specifically, VSRs occur when $\delta \boldsymbol{k} \cdot \boldsymbol{v} = n\mu_B B$, where $\boldsymbol{v}$ is the atom's velocity and $\delta \boldsymbol{k} = 2k$ is the difference in the wavevectors of the σ^+-σ^- light. The allowed n's depend on the relative orientation of optical and magnetic field vectors, and it is this selection rule that is the origin of the anisotropic sub-Doppler cooling in the large field (large magnetic moment) regime.

To see how this selection rule leads to anisotropic cooling, we first note that the atoms' polarization aligns along the local magnetic field in the presence of a large magnetic field (or large moment), defined as $\gamma_p \ll \omega_L \ll \Gamma$; in this large Zeeman energy regime, the magnetic field now serves as the quantization axis, not the optical polarization [13]. Now we examine the case in which the magnetic field is aligned parallel to the $\boldsymbol{k}$'s of a pair of σ^+-σ^- beams (Fig. 7.6). Along the spatial directions defined by the $\boldsymbol{k}$'s of the cooling light, the zero-mean-velocity VSR in the cooling force disappears ($n \neq 0$) even though finite-velocity VSRs remain ($n \geq 2$ are allowed). This is because there is no component of the polarization along the magnetic field (azimuthal symmetry about $\boldsymbol{k}$ is preserved), and thus no π transitions are allowed, which are necessary for $n = 0$ and $n = 1$ VSRs. In this case, sub-Doppler cooling to zero velocity along directions close to $\boldsymbol{k}$ is not possible when $\boldsymbol{B} \parallel \boldsymbol{k}$.

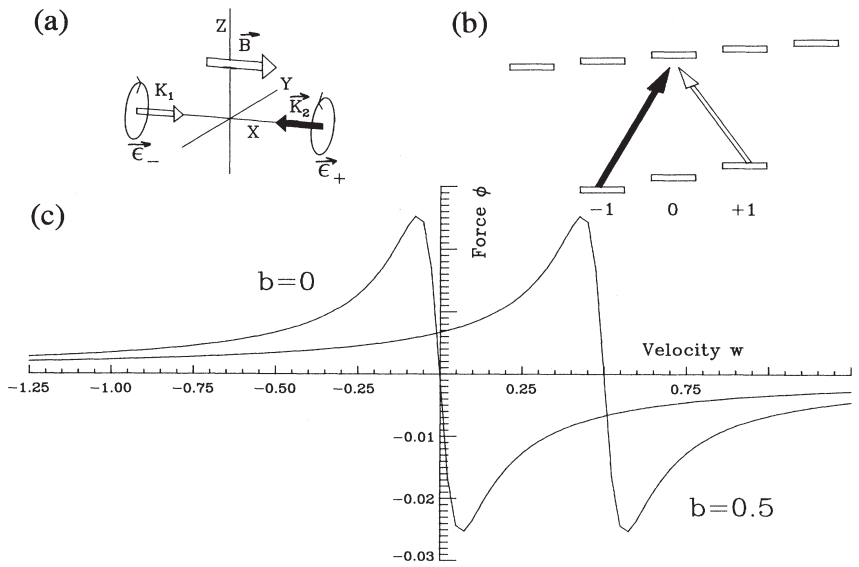

Figure 7.6: The case of the magnetic field parallel to the $\boldsymbol{k}$'s of a pair of σ^+-σ^- beams. (a) The beam and magnetic field configuration. (b) The two Zeeman states coupled by VSR with n = 2. (c) Numerical simulation with no field and a finite field. Note that a finite field shifts a zero-crossing point to a finite velocity, which results in a finite mean velocity of atoms. Reproduced from *Phys. Rev. A* **47**, 4160 (1993) [13].

However, not all sub-Doppler cooling is suppressed. A zero-velocity VSR remains in the cooling force along directions in which the local magnetic field is perpendicular to the cooling light's $\boldsymbol{k}$'s (for $\boldsymbol{B} \perp \boldsymbol{k}$ all n

are allowed) (see Fig. 7.7). This spatial modulation of allowable VSRs (n's) is the origin of the anisotropic nature of sub-Doppler cooling observed in the highly magnetic Dy system.

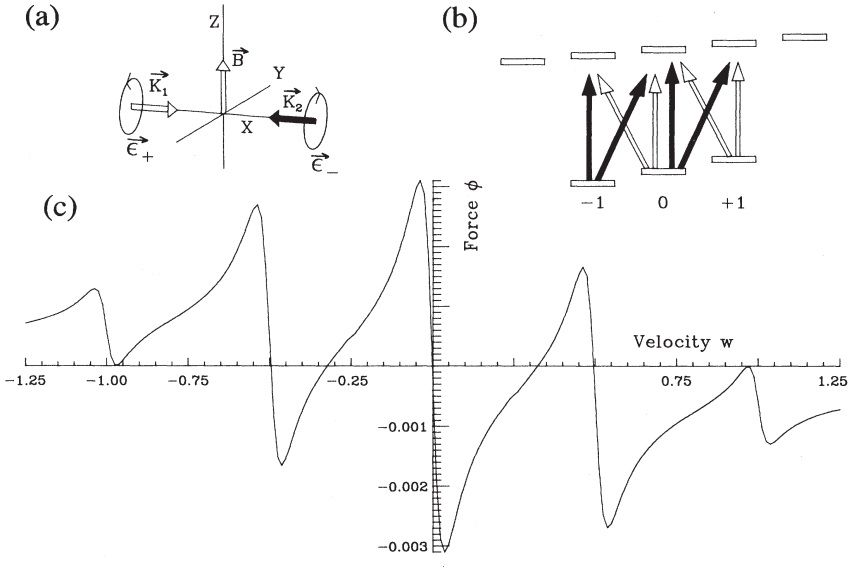

Figure 7.7: The case of the magnetic field perpendicular to the $\boldsymbol{k}$'s of a pair of σ^+-σ^- beams. (a) The beam and magnetic field configuration. (b) The three Zeeman states coupled by VSR with n = 0, ±1, ±2. (c) Numerical simulation with a finite field. Note that a finite field *does not* shift a zero-crossing point to a finite velocity, which results in cooling atoms to zero velocity. Reproduced from *Phys. Rev. A* **47**, 4160 (1993) [13].

In summary, σ^+-σ^- sub-Doppler cooling is preserved (fails) along directions perpendicular (parallel) to the local magnetic field in systems with large magnetic fields or large magnetic moments. Figure 7.8(b) illustrates this idea for the prolate striped MOT: sub-Doppler cooling occurs along $\hat{\rho}$ due to the green $\boldsymbol{k}_\rho$ σ^+-σ^- beams, but not along $\hat{z}$ due to atomic polarization orientation parallel to the magnetic field. The red $\boldsymbol{k}_z$ σ^+-σ^- beams only induce VSRs with non-zero velocity (e.g., $n \geq 2$) in the cooling force, and these beams cause the atoms to accelerate along $\hat{z}$ due to the magnetic quadrupole field gradient. The analogous mechanism holds for the oblate MOT when the magnetic field (quantization axis) is along $\hat{\rho}$ instead.

Prolate and oblate stripes oriented with respect to the quadrupole axis dominate because the only regions wherein the magnetic field is parallel to the $\boldsymbol{k}$-vectors are those in the plane or along the axis of symmetry of the quadrupole field. The regions' small relative volume is the origin of $N_{\text{minority}}/N_{\text{total}} < 10\%$. We note that this σ^+-σ^- mechanism is distinct from σ^+-σ^+ magnetically induced laser cooling [12].

7.5 Anisotropic sub-Doppler cooling in the Dy system

Although this description does not predict the prolate-to-oblate transition, our quantitative measurements in the prolate regime are consistent with this picture. Specifically, when $I_z/I_\rho < I_r^c$, $\bar{I} > \bar{I}_c$, and $\nabla_z \mathrm{B} > \nabla_z \mathrm{B}_c$ such that a prolate striped MOT forms, we observe larger-than-Doppler-limited temperatures along the $\hat{z}$ direction, which lies parallel to the local magnetic field (Fig. 7.2). As mentioned in the previous section, this is because along the $\boldsymbol{B} \parallel k$ direction the atoms accelerate as they move away from the trap center due to ever increasing magnetic fields and VSR velocities. An estimate of these resonant velocities—based on $v = \omega_z/k$ [92] in the 20 G/cm gradient field along $\hat{z}$—are $\geq T_D$, and are thus consistent with the absence of any sub-Doppler cooling mechanism along this direction. Specifically, outside a core of radius 30 μm—roughly the zone outside which anisotropic sub-Doppler cooling occurs; see below—the velocities are >0.35 m/s, resulting in 1D temperatures of >2.5 mK. Such temperatures are larger than the $T_D \approx 1$ mK limit for the typical Dy MOT parameters (see blue curves in Fig. 7.2).

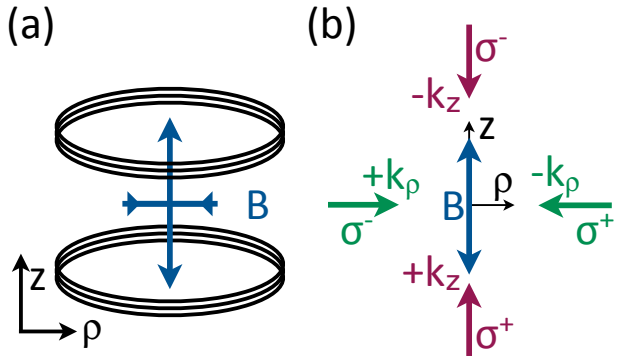

Figure 7.8: (a) Orientation of the MOT's magnetic quadrupole field. (b) Illustration of the anisotropic cooling in the prolate MOT including the MOT magnetic (B) field orientation, cooling beam wavevectors $\boldsymbol{k}$, and polarizations $\sigma^{\pm}$ near the z-axis.

Anisotropic sub-Doppler cooling is possible for the Dy MOT on the 421-nm, $\Delta g \approx 0$ transition because $\gamma_p \ll \omega_L \ll \Gamma$ is satisfied throughout the majority of the Dy MOT's quadrupole field. Specifically, Dy's optical pumping rate $\gamma_p \approx \bar{I}\Gamma/(1 + \bar{I} + 4\delta^2)$ is approximately equal to the light shift frequency, and the inequality is satisfied with the range of values $[\gamma_p, \omega_L, \Gamma] = 2\pi \cdot [0.8, 1-28, 32]$ MHz present in a typical Dy MOT with $\nabla B = 20$ G/cm and $0.04 < r < 1$ mm. In addition, $\gamma_p/\omega_L < 1$ for $\nabla \mathrm{B} > 10$ G/cm, which is close to the measured critical value $\nabla_z \mathrm{B}_c/2 = \nabla_\rho \mathrm{B}_c \approx 12$ G/cm. We do not have a simple estimate for $\bar{I}_c = 0.17$ and $I_r^c = 1.4$, but we expect that 2D numerical simulations of the Dy MOT could explicate the origin of these specific values as well as the underlying mechanism behind the stripe orientation transitions.

Chapter 8

Ultracold Bose-Fermi mixtures

^{164}Dy and ^{163}Dy are loaded into the 421-nm MOT (blue MOT or BMOT) in sequence, using a direct digital synthesizer (DDS) installed in the transfer cavity lock (Fig. 3.1). The DDS allows one to dynamically sweep its output frequency and shift the whole 421-nm laser by 271 MHz (see Fig. 8.1) for the dual species loading. In the experiments, ^{163}Dy is laser cooled and trapped after ^{164}Dy, while ^{164}Dy is held in the magnetic trap (see Fig. 8.2). This loading order avoids the loss of ^{163}Dy in the magnetic trap, which has a lower initial trap population than ^{164}Dy [1]. After the dual BMOT is loaded with the 421-nm laser, the both of ^{164}Dy and ^{163}Dy are simultaneously narrow-line cooled using the 741-nm transition.

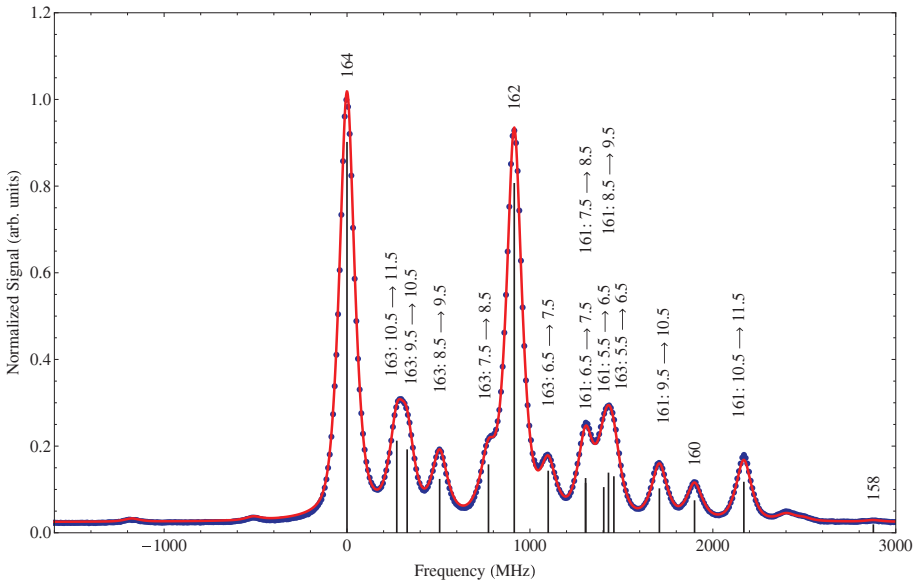

Figure 8.1: The 421-nm line spectrum. The DDS shifts the 421-nm laser frequency by 271 MHz to load the dual species BMOT. Reproduced from arxiv:0904.1438v2 [14].

The narrow-line cooling (red MOT or RMOT) exploits the 741-nm transition with a narrow linewidth of 2 kHz [2]. In this narrow-line cooling [94] , the magnetic force, the radiation force, and the gravitational

[1] This loading sequence makes the Zeeman slower beam for ^{163}Dy closer to the resonance of ^{164}Dy, but this still has $\sim$ -16Γ detuning.

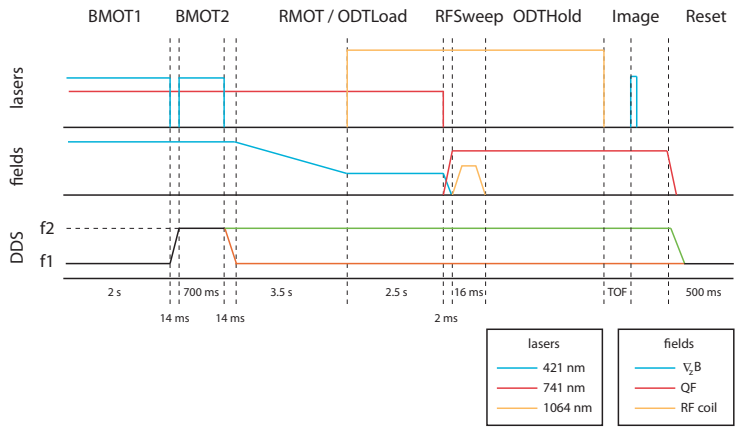

Figure 8.2: The experimental sequence to load dual species ODT. f1 is the DDS frequency for ^{164}Dy and f2 is for ^{163}Dy. By holding the DDS frequency at f2 (green), ^{163}Dy is imaged. By returning the DDS frequenc to f1 (orange), ^{164}Dy is imaged. The imaging probe beam has a pulse width of 160 μs.

force now have a comparable strength to confine the atoms, unlike the conventional MOT, where the most confinement comes from the radiation force. To see this more clearly, one can look at the net force expression F_z [94] with typical experimental parameters:

$$F_z(z, v_z) = F_0 + \frac{\hbar k \Gamma}{2} \times \frac{\bar{I}}{1 + \bar{I} + 4(\Delta/\Gamma - z/z_0^{\pm} - k v_z/\Gamma)^2} \tag{8.1}$$

where

$$F_0 = -g_g m_g \mu_B |\nabla_z B| - mg, \qquad z_0^{\pm} = \frac{\hbar \Gamma}{\mu_{\pm} |\nabla_z B|} \tag{8.2}$$

$\mu_{\pm} = (\pm g_e + m_J \Delta g_{eg})\mu_B$, and $\Delta g_{eg} = g_e - g_g$.

In the magnetic trap, only low-field seeking atoms are trapped with a force pushing the atoms toward the center of the magnetic trap, zero field point. The blue-detuned RMOT beams [2] counteract to balance against the magnetic force, pushing outward of the magnetic quadrupole field, and the RMOT is formed at a finite magnetic field point. In RMOT, we laser cool and trap atoms to the ultracold [3] temperature $\sim$ 10 μK. In addition to the final ultracold temperature, the combination of this finite magnetic field and the polarization of RMOT beams spin-polarizes atoms to the low field seeking stretched state [94].

The RMOT is loaded by lowering the magnetic field gradient as collecting the atoms from the magnetic trap and effectively cooling the atoms at a fixed low field gradient (see Fig. 8.2). As shown in Fig. 8.3, which

[2] RMOT beams are blue-detuned with respect to the unshifted atomic transition.
[3] Ultracold regime in a dipolar gas is defined by a threshold dipolar temperature, which is 50 μK for dysprosium [56].

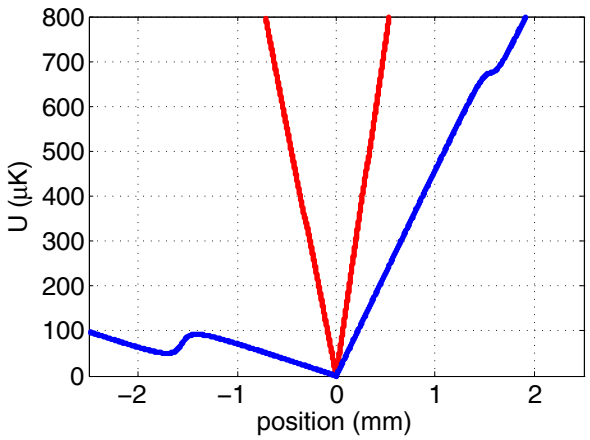

Figure 8.3: Simulation of potential energy as a function of position. Calculation with typical experimental parameters: $\bar{I} = 2000$, $\Delta = +2\pi \cdot 1\,\mathrm{M}Hz$, $|\nabla_z B| = 20$ G/cm (red) & 4 G/cm (blue), and $v_z = 0$.

is obtained by $U(z) = -\int F_z(z', v_z = 0)dz'$, the linear magnetic trap with the initial high gradient of 20 G/cm is clearly seen dominant at the beginning of the sequence. However, with a lower field gradient of 4 G/cm, the 741-nm cooling and trapping beams become comparable to the magnetic force and the atoms are trapped in the dimple of the potential energy at $z \sim$ -1.5 mm. This is in agreement with experiments. Up to the narrow-line cooling stage, there is no significant loss observed due to either the interspecies interaction between ^{164}Dy and ^{163}Dy or the hyperfine structure of ^{163}Dy in the *dual* species loading. It should be emphasized that in this thesis we capture ^{163}Dy without any repumping beam at 421 nm and 741 nm.

There are two inelastic collisions to be considered at this stage, spin relaxation and dipolar relaxation. The spin relaxation which conserves the sum of m values of two colliding particles occurs when atoms are not at the stretched ($m_J = +8$ or -8 for bosons) and can cause the heating and the loss of atoms. This spin relaxation is suppressed by spin-purification at the narrow-line cooling phase. However, the dipolar relaxation can still occur, which we believe limits the final temperature of narrow-line cooled MOT to be ~ 10 μK, much higher than Doppler temperature at 741 nm, ~ 40 nK. In principle, the dipolar relaxation is suppressed by transferring the population to the absolute ground state. For ^{164}Dy, which does not have the hyperfine structure, the absolute ground state is achieved by a single frequency sweep of the adiabatic rapid passage, which spin-flips all the $m_J = +8$ states to $m_J =$ -8 states. By doing a single frequency sweep but with a larger sweeping range to compensate the difference in Larmor frequency of ^{163}Dy, ^{163}Dy was also spin-flipped in the highest manifold $F = 21/1$ (see Fig. 2.3) together with ^{164}Dy. The trap population is summarized in Table 8.1.

Here RMOT number is almost equal to BMOT, and it may seem to be 100% transfer efficiency between the two stages. However, it is actually about 50%, because RMOT captures another half from the "background"

Table 8.1: Population of Bose-Fermi mixtures (in dual loading of ^{164}Dy and ^{163}Dy) at each stage.

stage	N_{164}	N_{163}	n_{164} [cm^{-3}]	n_{163} [cm^{-3}]
BMOT	4×10^7	7×10^6		
RMOT	5×10^7	7×10^6		
spin-flipped DualODT	6×10^6	3×10^5	5×10^9	7×10^8

magnetically trapped atoms. Higher N_{163} (8×10^5) was observed when ^{163}Dy was not simultaneously loaded into the optical dipole trap with ^{164}Dy (6×10^6), indicating that there occurs interspecies interaction in the dual trapping, but the scattering length and its sign have to be determined in the future experiments. The low ^{163}Dy trap number in the ODT is also strongly suggestive of hyperfine changing collisions. Therefore, it is required to transfer ^{163}Dy to the lowest manifold $F = 11/2$ via five additional hyperfine transitions in order to reach the absolute ground state. Currently, the work on stable microwave source and generation is in progress (see Figs. 8.4 and 8.5).

Figure 8.4: Microwave coil machined from the material Rogers Corp. R04350B with a soldered SMA connector.

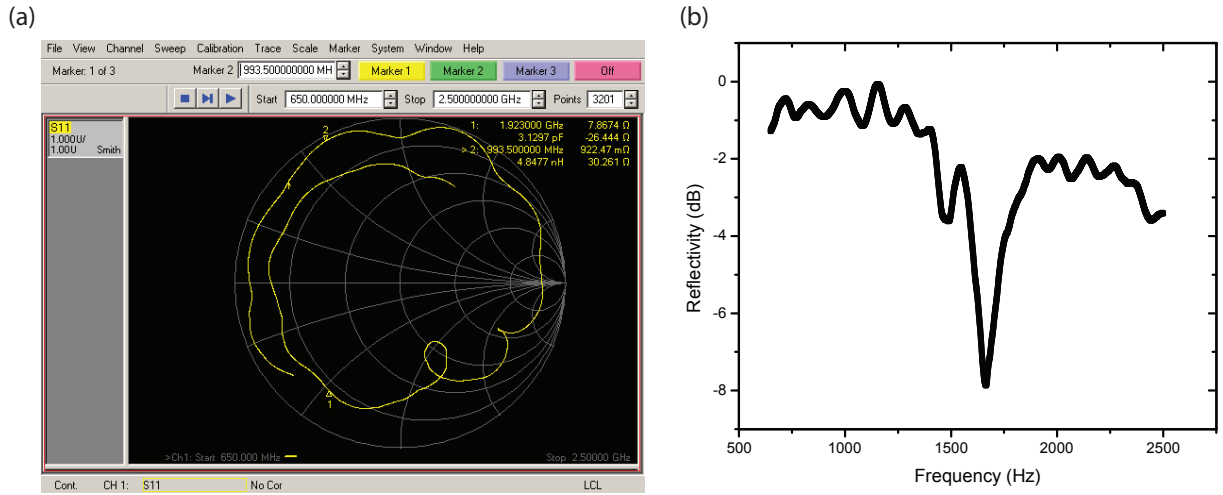

Figure 8.5: Characterization of the microwave coil shown in Fig 8.4. (a) Screenshot of Smith chart from Agilent PNA 5320A network analyzer. Two center frequencies are marked. (b) Reflectivity as a function of frequency. Note that stub-tuning is necessary.

For a prospect to realize Bose-Fermi mixtures of ^{164}Dy and ^{161}Dy, one can take an advantage of the inverted hyperfine structure of ^{161}Dy in the ground state at 421-nm and 741-nm transitions [8, 9, 2], which allows one to prepare the atoms in the lowest manifold of the hyperfine structure following the same experimental sequence discussed above with ^{163}Dy. However, this method complicates the laser systems at 421 and 741 nm. For BMOT loading, required is the ability to shift ~ 2.2 GHz of the difference of ^{164}Dy and ^{161}Dy $F = 11/2 \rightarrow F' = 13/2$ transition in the 421-nm laser (see Fig. 8.1). For RMOT, it is one solution to add another 741-nm laser system to bridge the frequency difference of ~ 1.6 GHz in Fig. 8.6, using the beat-note lock discussed in Fig. 3.2. The schematic of the 741-nm beat-note lock system in progress is depicted in Fig. 8.7.

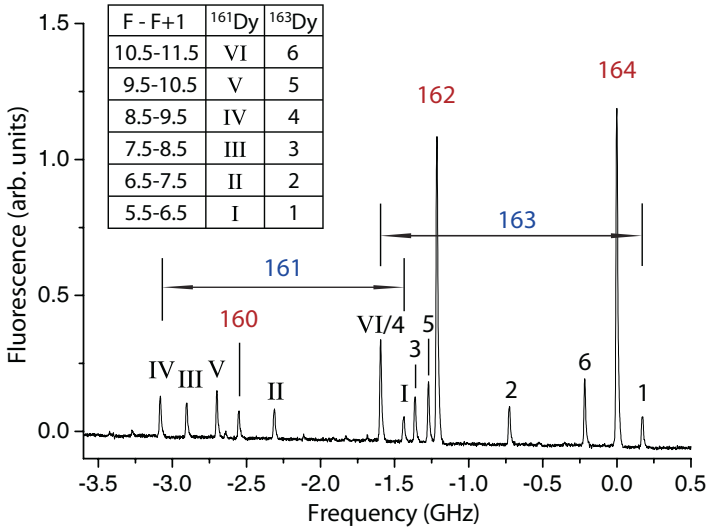

Figure 8.6: The 741-nm line spectrum for the five most abundant Dy isotopes [2]. Bosonic isotope peaks are marked with mass numbers in red. Hyperfine peaks of fermionic isotopes (blue) are identified by the markers defined in the inset table. The VIth peak of ^{161}Dy and the 4th peak of ^{163}Dy overlap.

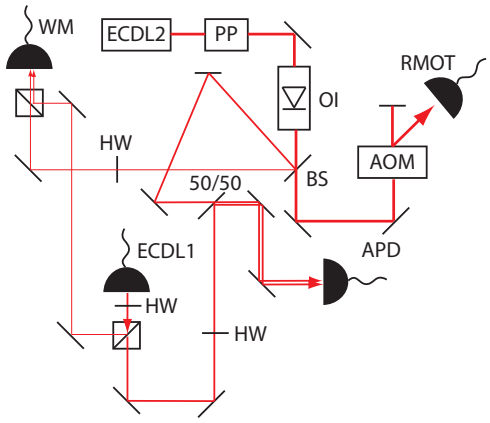

Figure 8.7: Schematic of optics for the beatnote lock at 741 nm. PP: prism pair. OI: optical isolator. BS: beam sampler. AOM: acousto-optical modulator. WM: wavemeter.

Appendix A

MATLAB codes

A.1 Control sequence example

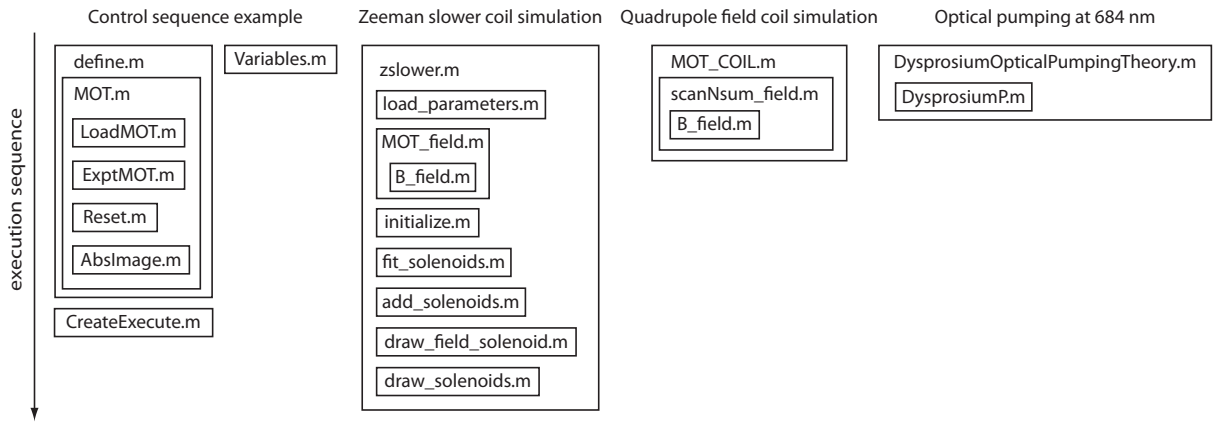

Figure A.1: The structure of codes in Appendix A.

A.1.1 define.m

```
1
2  clc
3  clear all
4  close all
5  warning off all
6
7  %Import Class Library
8  import Objects.*
9
10 %% ************************** VALUES ***********************************
11
```

```
12 run('Variables')
13 sampleRate = 1/dt;
14
15 %Loop for Block Creation as many as number of TOF measurements
16 % TOFSchedule = [0 1e-3 2e-3 3e-3 4e-3 5e-3]; 0 ms expansion, 1 ms expansion, ..., 5 ms ...
       expansion
17 % TOFSchedule is stored in Variables.m
18 N = size(TOFSchedule,2);
19
20 for i = 1 : N
21
22     outputLines = MOT(i); % i = 1 : size(TOF), i_{th} time of TOF
23     tf = size(outputLines,1) * dt;
24
25     %%BEGIN DEFINITION
26     timeLine = TimeLine;
27     timeLine.durationTime = tf; %Remember that this is in sample rate units
28
29     %Empty Block Definition
30     MOTBlock = Block('MOTBlock',timeLine);
31
32     %% ADD DEVICE
33     MOTBlock =MOTBlock.addDevice('dev1', sampleRate); %Device names must map to hardware!
34     MOTBlock =MOTBlock.addDevice('dev2', sampleRate); %Device names must map to hardware!
35
36     MOTBlock.primaryDevice = 'dev2';
37
38     %% ADD LINES
39
40     % MOTBeam           dev2/port0/line2
41     % ZSBeam            dev2/port0/line3
42     % OvenShutter       dev2/port0/line4
43     % AbsBeam           dev2/port0/line5
44     % Camera2           dev2/port0/line7
45     % MOTShutter        dev2/port1/line0
46     % AbsBeamShutter    dev2/port1/line1
47     % TransCooling      dev2/port1/line2
48     % MOTCoilAnalog     dev1/ao0
49     % QuantCoil         dev1/ao1
50     % SequenceTrigger   dev2/port3/line7
```

```
51
52      MOTBlock = MOTBlock.addLine('dev2', 'MOTBeam','dev2/port0/line2');
53      MOTBlock = MOTBlock.addLine('dev2', 'ZSBeam','dev2/port0/line3');
54      MOTBlock = MOTBlock.addLine('dev2', 'OvenShutter','dev2/port0/line4');
55      MOTBlock = MOTBlock.addLine('dev2', 'AbsBeam','dev2/port0/line5');
56      MOTBlock = MOTBlock.addLine('dev2', 'Camera2','dev2/port0/line7');
57      MOTBlock = MOTBlock.addLine('dev2', 'MOTShutter','dev2/port1/line0');
58      MOTBlock = MOTBlock.addLine('dev2', 'AbsBeamShutter','dev2/port1/line1');
59      MOTBlock = MOTBlock.addLine('dev2', 'TransCooling','dev2/port1/line2');
60      MOTBlock = MOTBlock.addLine('dev1', 'MOTCoilAnalog','dev1/ao0',-10.0,10.0);
61      MOTBlock = MOTBlock.addLine('dev1', 'QuantCoil','dev1/ao1',-10.0,10.0);
62      MOTBlock = MOTBlock.addLine('dev2', 'SequenceTrigger','dev2/port3/line7');
63
64      %Need to Initialize First
65      MOTBlock = MOTBlock.initializeAllDevices();
66
67      %Add data
68      MOTBlock = MOTBlock.addLineData('dev2', 'MOTBeam',0, outputLines(:,1));
69      MOTBlock = MOTBlock.addLineData('dev2', 'ZSBeam',0, outputLines(:,2));
70      MOTBlock = MOTBlock.addLineData('dev2', 'OvenShutter',0, outputLines(:,3));
71      MOTBlock = MOTBlock.addLineData('dev2', 'AbsBeam',0, outputLines(:,4));
72      MOTBlock = MOTBlock.addLineData('dev2', 'Camera2',0, outputLines(:,5));
73      MOTBlock = MOTBlock.addLineData('dev2', 'MOTShutter',0, outputLines(:,6));
74      MOTBlock = MOTBlock.addLineData('dev2', 'AbsBeamShutter',0, outputLines(:,7));
75      MOTBlock = MOTBlock.addLineData('dev2', 'TransCooling',0, outputLines(:,8));
76      MOTBlock = MOTBlock.addLineData('dev1', 'MOTCoilAnalog',0, outputLines(:,9));
77      MOTBlock = MOTBlock.addLineData('dev1', 'QuantCoil',0, outputLines(:,10));
78      MOTBlock = MOTBlock.addLineData('dev2', 'SequenceTrigger',0, outputLines(:,11));
79      %%REMEMBER This is only definition.
80      %%Saving
81
82      save(['MOTBlock' num2str(i)],'MOTBlock');
83      clear MOTBlock;
84
85  end
86
87  display(sprintf('Definition Elapsed Time: %.1f s',toc))
```

A.1.2 MOT.m

```
function LineOutput = MOT(i)

% i is variable for i_{th} value of TOF to be used.

%% ******************* CONFIGURATIONS ***********************************
% MOTBeam           dev2/port0/line2
% ZSBeam            dev2/port0/line3
% OvenShutter       dev2/port0/line4
% AbsBeam           dev2/port0/line5
% Camera2           dev2/port0/line7
% MOTShutter        dev2/port1/line0
% AbsBeamShutter    dev2/port1/line1
% TransCooling      dev2/port1/line2
% MOTCoilAnalog     dev1/ao0
% QuantCoil         dev1/ao1
% SequenceTrigger   dev2/port3/line7

% LineOutput = [MOTBeam ZSBeam OvenShutter AbsBeam Camera2 MOTShutter
%               AbsBeamShutter TransCooling MOTCoilAnalog QuantCoil SequenceTrigger];
% LineOutput is a collection of lines (each line as a column vector).
% The order of lines in LineOutput follows the line number shown above.

% dt -> sampling resolution, s
%% ************************** VALUES ***********************************

run('Variables')

%% ********************** INDEX CONVERSION ***************************
% starting index
% (MOTLoadST / dt) + 1
% /dt converts real time to index
% + 1 is necessary because of index starting from 1, NOT 0

% ending index
% (MOTLoadST + MOTLoadTD - dt) / dt + 1
% - dt is necessary because of convention to signal alignment to FRONT
% (leaves an index for starting index in next subblock)
% /dt converts real time to index
% + 1 is necessary because of index starting from 1, NOT 0

```

```
41 AbsImageTI = round(((LoadMOTTD + TOFSchedule(i) - MOTBeamDelay - AbsBeamTT) / dt) + 1);
42
43 ImageTD = EachAbsImageTD * 3;                % imaging time duration, s
44 % 3 refers to number of images
45 ImageID = AbsImageTI : round(AbsImageTI + ImageTD / dt - 1);
46 % index to be replaced
47
48 SequenceTriggerTI = round(SequenceTriggerTT / dt + 1);
49 % sequence trigger index
50 SequenceTriggerDI = round((SequenceTriggerDT - dt )/ dt + 1);
51 % sequence trigger duration index
52
53 %% ************************ SEQUENCES **********************************
54
55 cd SubBlocks
56
57 LineOutput = [LoadMOT; ExptMOT; Reset];
58 LineOutputAbsImage = AbsImage; % AbsImage = [AbsBeam Camera2 QuantCoil]
59
60 % absorption imaging replacement
61 LineOutput(ImageID, 4) = LineOutputAbsImage(:,1);
62 LineOutput(ImageID, 5) = LineOutputAbsImage(:,2);
63 LineOutput(ImageID, 10) = LineOutputAbsImage(:,3);
64
65 RunTDSize = size(LineOutput, 1);
66 % SequenceTrigger(1 : SequenceTriggerTI - 1, 1) = SequenceTriggerDefault;
67 % SequenceTrigger(SequenceTriggerTI : SequenceTriggerTI + SequenceTriggerDI, 1) = ...
       abs(SequenceTriggerDefault - 1);
68 % SequenceTrigger(SequenceTriggerTI + SequenceTriggerDI + 1 : RunTDSize, 1) = ...
       SequenceTriggerDefault;
69
70 LineOutput(:, NumberOfLine) = 1;
71
72 if (TOFSchedule(i) - AbsBeamTT + 3 * EachAbsImageTD) > ExptMOTTD
73     display('(TOFSchedule(i) - AbsBeamTT + 3 * EachAbsImageTD) > ExptMOTTD')
74     display('Press Ctrl + C to stop MATLAB and increase ExptMOTTD in variables.m')
75     pause
76 end
77
78 cd ..
```

A.1.3 Variables.m

```
%% ******************** TIME CONSTANTS ********************
us = 10^(-6); % s
ms = 10^(-3); % s
s = 1; % s

%% ******************** DELAYS ********************
% With respect to end of LoadMOT block
MOTBeamDelay = 1.21*ms; % OFF, 0 s delay and duration, AOM
MOTShutterDelay= 624*us + 1.21*ms; % CLOSE, 624 us delay, 1.21 ms duration
ZSBeamDelay = 2*ms + 1.2*ms + 1.21*ms; % CLOSE, 2 ms delay, 1.2 ms duration
TransCoolingDelay = 0*s + 1.21*ms; % OFF, 0 s delay and duration, AOM
MOTCoilAnalogDelay = 0*s + 316*us + (1.21*ms - 316*us); % OFF, 0 s delay, 316 us duration,
% (1.21*ms - 316*us) is necessary to sequence at the same time as MOT beam AOM
OvenShutterDelay = 141*ms + 27*ms; % CLOSE, 141 ms delay, 27 ms duration
QuantCoilDelay= 0*s + 1.92*ms; % ON, 0 s delay, 1.92 ms duration, NOT USED

%% NOT USED
AbsBeamShutterCLOSEDelay = 620*us + 660*us + 1*ms;
% CLOSE, 620 us delay, 660 us duration, 1 ms extra to ensure
AbsBeamShutterOPENDelay = 7.7*ms + 2.3*ms + 1*ms;
% OPEN, 7.7 ms delay, 2.3 ms duration, 1 ms extra to ensure

%% ******************** SCHEDULE AND TIMES ********************************

dt = 10*us; % Time resolution, s

TOFSchedule = [2.5]*ms - MOTBeamDelay;
%TOFSchedule = [3 4 5 3.3 4.3 3.6 4.6]*ms;
% 1 ms is used for MOT information, the rest is TOF for temperature

% TOF, time between the end of LoadMOT and the start of first absorption beam
numTOF = size(TOFSchedule,2);

numRun = 10; % number of sets of TOF, (or number of averaging data points
% at a specified TOF time), default = 10

contPar = 20; % control parameters
```

```
38 contParUnit = 'Gc'; % control parameter unit, mW, Gc (G/cm),...
39 numContPar = size(contPar,2);
40
41 LoadMOTTD = 2*s; %2*s;% MOT loading time duration, s
42 ExptMOTTD = 1.1*s;% MOT experiment time duration, s
43
44 EachAbsImageTD = 350*ms;                    % absorption imaging separation, s
45 Camera2TD = dt;
46 % width of Camera2 triggering
47 % NOTE Camera2TD > 1/sampling time of National Instrument board
48 AbsBeamTD = 100*us; % absorption beam pulse width, s
49 AbsBeamTT = 0*ms; %QuantCoilDelay; % time from EACH absorption imaging to absorption beam ...
       start, s
50
51 ResetTD = 0.5*s;                            % reseting time duration, s
52
53 SequenceTriggerTT = 2*s;                   % sequence triggering time, s
54 SequenceTriggerDT = 1*ms;                   % sequence triggering duration, s
55
56 %% ******************** VARIABLE ASSIGNMENTS ********************
57
58 NumberOfLine = 11;
59
60 MOTBeamOn = 1; % MOT beam On
61 MOTBeamOff = 0;
62 ZSBeamOn = 0; % Zeeman slower beam On
63 ZSBeamOff = 1;
64 OvenShutterOpen = 0; % oven shutter open
65 OvenShutterClose = 1;
66 AbsBeamOn = 1;
67 AbsBeamOff = 0; % absorption bem off
68 Camera2Default = 0; % camera on side default setting, ready to trigger
69 MOTShutterOpen = 0; % MOT beam shutter open
70 MOTShutterClose = 1;
71 AbsBeamShutterOpen = 1; % absorption beam shutter open
72 AbsBeamShutterClose = 0;
73 TransCoolingOn = 1; % transverse cooling beam on
74 TransCoolingOff = 0;
75 MOTCoilAnalogCal = -0.0289;
76 % calibration of Vset / QT graident, V / (G/cm)
```

```
77 % V Agilent = 6.506 V, 12/15/09
78 % Note quadrupole servo needs optimization and recalibration.
79
80 MOTCoilAnalogDefault = contPar; % quadrupole coil default gradient, G/cm
81
82 MOTCoilAnalogOff = 1; % V_set = +1 V, 0 A, OFF
83 QuantCoilCal = -5/3;
84 % quantization axis coil calibration, Vset / Iactual = -5 V / 3A, 01/06/10
85 % V/A
86 QuantCoilOff = +1; % quantization axis coil default, 1 V set point -> 0 A
87 SequenceTriggerDefault = 0; % sequence trigger default value
88
89 %% Lines
90
91 LineOutputNames = {'MOTBeam', 'ZSBeam', 'OvenShutter', 'AbsBeam', 'Camera2', 'MOTShutter',...
92     'AbsBeamShutter', 'TransCooling', 'MOTCoilAnalog', 'QuantCoil', 'SequenceTrigger'};
```

A.1.4 ExptMOT.m

```
1  function LineOutput = ExptMOT
2
3  % ************************** VALUES ************************************
4  cd ..
5  run('Variables')
6  cd SubBlocks
7
8  RunTDSize = round(ExptMOTTD / dt);
9
10 MOTBeam(1 : RunTDSize, 1) = MOTBeamOff;
11 ZSBeam(1 : RunTDSize, 1) = ZSBeamOff;
12
13 OvenShutter(1 : RunTDSize, 1) = OvenShutterOpen;
14
15 AbsBeam(1 : RunTDSize, 1) = AbsBeamOff;
16 Camera2(1 : RunTDSize, 1) = Camera2Default;
17 MOTShutter(1 : RunTDSize, 1) = MOTShutterClose;
18 AbsBeamShutter(1 : RunTDSize, 1) = AbsBeamShutterOpen;
19 TransCooling(1 : RunTDSize, 1) = TransCoolingOff;
```

```
MOTCoilAnalog(1 : RunTDSize, 1) = MOTCoilAnalogOff;
QuantCoil(1 : RunTDSize, 1) = 3 * QuantCoilCal;

LineOutput = [MOTBeam ZSBeam OvenShutter AbsBeam Camera2 MOTShutter...
    AbsBeamShutter TransCooling MOTCoilAnalog QuantCoil];
```

A.1.5 LoadMOT.m

```
function LineOutput = LoadMOT

% ************************** VALUES ***********************************
cd ..
run('Variables')
cd SubBlocks

RunTDSize = round(LoadMOTTD / dt);

MOTBeamTI = round((LoadMOTTD - MOTBeamDelay) / dt);
MOTShutterTI = round((LoadMOTTD - MOTShutterDelay) / dt);
ZSBeamTI = round((LoadMOTTD - ZSBeamDelay) / dt);
TransCoolingTI = round((LoadMOTTD - TransCoolingDelay) / dt);
MOTCoilAnalogTI = round((LoadMOTTD - MOTCoilAnalogDelay) / dt);
OvenShutterTI = round((LoadMOTTD - OvenShutterDelay) / dt);

MOTBeam(1 : MOTBeamTI, 1) = MOTBeamOn;
MOTBeam(MOTBeamTI + 1 : RunTDSize, 1) = MOTBeamOff;
ZSBeam(1 : ZSBeamTI, 1) = ZSBeamOn;
ZSBeam(ZSBeamTI + 1 : RunTDSize, 1) = ZSBeamOff;

% OvenShutter(1 : OvenShutterTI, 1) = OvenShutterOpen;
% OvenShutter(OvenShutterTI + 1 : RunTDSize, 1) = OvenShutterOpen;
OvenShutter(1 : RunTDSize, 1) = OvenShutterOpen;

AbsBeam(1 : RunTDSize, 1) = AbsBeamOff;
Camera2(1 : RunTDSize, 1) = Camera2Default;
MOTShutter(1 : MOTShutterTI, 1) = MOTShutterOpen;
MOTShutter(MOTShutterTI + 1 : RunTDSize, 1) = MOTShutterClose ;
AbsBeamShutter(1 : RunTDSize, 1) = AbsBeamShutterOpen;
```

```
TransCooling(1 : TransCoolingTI, 1) = TransCoolingOn;
TransCooling(TransCoolingTI + 1 : RunTDSize, 1) = TransCoolingOff;
MOTCoilAnalog(1 : MOTCoilAnalogTI, 1) = MOTCoilAnalogDefault * MOTCoilAnalogCal;
MOTCoilAnalog(MOTCoilAnalogTI + 1 : RunTDSize, 1) = MOTCoilAnalogOff;
QuantCoil(1:MOTCoilAnalog,1) = QuantCoilOff;
QuantCoil(MOTCoilAnalogTI + 1 : RunTDSize, 1) = 3*QuantCoilCal;;
%QuantCoil(1 : RunTDSize, 1) = QuantCoilOff;

LineOutput = [MOTBeam ZSBeam OvenShutter AbsBeam Camera2 MOTShutter...
    AbsBeamShutter TransCooling MOTCoilAnalog QuantCoil];
```

A.1.6 Reset.m

```
function LineOutput = Reset

% ************************** VALUES ***********************************
cd ..
run('Variables')
cd SubBlocks

RunTDSize = round(ResetTD / dt);

MOTBeam(1 : RunTDSize, 1) = MOTBeamOn;
ZSBeam(1 : RunTDSize, 1) = ZSBeamOn;

OvenShutter(1 : RunTDSize, 1)  = OvenShutterOpen;

AbsBeam(1 : RunTDSize, 1) = AbsBeamOn;
Camera2(1 : RunTDSize, 1) = Camera2Default;
MOTShutter(1 : RunTDSize, 1) = MOTShutterOpen;
AbsBeamShutter(1 : RunTDSize, 1) = AbsBeamShutterOpen;
TransCooling(1 : RunTDSize, 1) = TransCoolingOn;
MOTCoilAnalog(1 : RunTDSize, 1) = MOTCoilAnalogDefault * MOTCoilAnalogCal;
QuantCoil(1 : RunTDSize, 1) = QuantCoilOff;

LineOutput = [MOTBeam ZSBeam OvenShutter AbsBeam Camera2 MOTShutter...
    AbsBeamShutter TransCooling MOTCoilAnalog QuantCoil];
```

A.1.7 AbsImage.m

```
function LineOutput = AbsImage

% ************************** VALUES ***********************************
cd ..
run('Variables')
cd SubBlocks

%% ***************************** TIMES ***********************************
% BE AWARE OF DEAD TIME OF TRIGGERING!
% OPTICAL PUMPING IS NOT DONE HERE.
RunTDSize = round((EachAbsImageTD * 3) / dt);
% 3 refers to number of images taken in this block

Image1ST = 0; % % image1 start triggering time, s
Image1ET = Image1ST + Camera2TD; % image1 end triggering time, s
AbsBeam1ST = Image1ST + AbsBeamTT; % absorption beam start triggering time, s
AbsBeam1ET = AbsBeam1ST + AbsBeamTD; % absorption beam end triggering time, s
Image2ST = EachAbsImageTD; % s
Image2ET = Image2ST + Camera2TD;
AbsBeam2ST = Image2ST + AbsBeamTT; % s
AbsBeam2ET = AbsBeam2ST + AbsBeamTD;
Image3ST = EachAbsImageTD + EachAbsImageTD; % s
Image3ET = Image3ST + Camera2TD;
AbsBeam3ST = Image3ST + AbsBeamTT; % s
AbsBeam3ET = AbsBeam3ST + AbsBeamTD;

Image1SI = round((Image1ST / dt) + 1); % image1 starting index
Image1TI = round((Image1ET / dt) + 1); % image1 triggering index
Image1EI = round((Image1ST + EachAbsImageTD - dt) / dt + 1); % image 1 ending index
AbsBeam1SI = round((AbsBeam1ST / dt) + 1);
AbsBeam1EI = round((AbsBeam1ET / dt) + 1);
Image2SI = round((Image2ST / dt) + 1); % image2 starting index
Image2TI = round((Image2ET / dt) + 1);
Image2EI = round((Image2ST + EachAbsImageTD - dt) / dt + 1); % image 2 ending index
AbsBeam2SI = round((AbsBeam2ST / dt) + 1);
AbsBeam2EI = round((AbsBeam2ET / dt) + 1);
Image3SI = round((Image3ST / dt) + 1); % image3 starting index
```

```
38 Image3TI = round((Image3ET / dt) + 1);
39 Image3EI = round((Image3ST + EachAbsImageTD - dt) / dt + 1); % image 3 ending index
40 AbsBeam3SI = round((AbsBeam3ST / dt) + 1);
41 AbsBeam3EI = round((AbsBeam3ET / dt) + 1);
42
43 AbsBeamShutterCLOSETI = round((Image3ST - AbsBeamShutterCLOSEDelay) / dt + 1);
44 % AbsBeamShutter is triggered to be CLOSED in advance before 3rd image taking
45 % because of OFF delay and duration (icluding extra time)
46 % AbsBeamShutterCLOSEDelay is set with respect to Image3ST
47 % AbsBeamShutter cannot be triggered too close to Image2TT (2nd image
48 % taking)
49
50 %% ***************************** IMAGE1 **********************************
51 % image WITH cloud
52 Camera2(Image1SI : Image1TI, 1) = abs(Camera2Default - 1);
53 % abs is used to switch to the other
54 Camera2(Image1TI + 1 : Image1EI, 1) = Camera2Default;
55 AbsBeam(Image1SI : AbsBeam1SI - 1, 1) = AbsBeamOff;
56 AbsBeam(AbsBeam1SI : AbsBeam1EI, 1) = AbsBeamOn;
57 AbsBeam(AbsBeam1EI + 1 : Image1EI, 1) = AbsBeamOff;
58 %AbsBeamShutter(Image1SI : Image1EI, 1) = AbsBeamShutterOpen;
59 QuantCoil(Image1SI : Image1EI, 1) = 3*QuantCoilCal; % 3 A
60
61 %% ***************************** IMAGE2 **********************************
62 % image WITHOUT cloud BUT LIGHT
63 % (the cloud has disappeared, life time < EachAbsImageTD)
64 Camera2(Image2SI : Image2TI, 1) = abs(Camera2Default - 1);
65 Camera2(Image2TI + 1 : Image2EI, 1) = Camera2Default;
66 AbsBeam(Image2SI : AbsBeam2SI - 1, 1) = AbsBeamOff;
67 AbsBeam(AbsBeam2SI : AbsBeam2EI, 1) = AbsBeamOn;
68 AbsBeam(AbsBeam2EI + 1 : Image2EI, 1) = AbsBeamOff;
69 %AbsBeamShutter(Image2SI : AbsBeamShutterCLOSETI, 1) = AbsBeamShutterOpen;
70 %AbsBeamShutter(AbsBeamShutterCLOSETI + 1 : Image2EI, 1) = AbsBeamShutterClose;
71 QuantCoil(Image2SI : Image2EI, 1) = 3*QuantCoilCal; % 3 A
72
73 %% ***************************** IMAGE3 **********************************
74 % image of camera noise and background of dark room
75 Camera2(Image3SI : Image3TI, 1) = abs(Camera2Default - 1);
76 Camera2(Image3TI + 1 : Image3EI, 1) = Camera2Default;
77 AbsBeam(Image3SI : AbsBeam3SI - 1, 1) = AbsBeamOff;
```

```
78 AbsBeam(AbsBeam3SI : AbsBeam3EI, 1) = AbsBeamOff;
79 AbsBeam(AbsBeam3EI + 1 : Image3EI, 1) = AbsBeamOff;
80 %AbsBeamShutter(Image3SI : Image3EI, 1) = AbsBeamShutterClose;
81 QuantCoil(Image3SI : Image3EI, 1) = 3*QuantCoilCal; % 3 A
82
83 LineOutput = [AbsBeam Camera2 QuantCoil];
```

A.1.8 CreateExecute.m

```
1  import Objects.*
2  %% This code is an example of loading a saved block definition
3  % and executing it.
4
5  clear all
6  clc
7
8  fname = 'MOTBlock'; %Base file name.
9
10 run('Variables')
11
12 N = size(TOFSchedule,2); %Number of TOF points
13 % TOFSchedule = [0 1e-3 2e-3 3e-3 4e-3 5e-3]; 0 ms expansion, 1 ms expansion, ..., 5 ms ...
       expansion
14 % TOFSchedule is stored in Variables.m
15
16 for j = 1:1
17     for i = 1:1 % TOF data points (how many different TOF times are used)
18         % number of sets of TOF, (or number of averaging data points
19         % at a specified TOF time), default = 10
20
21         var = [fname num2str(i)];
22         load(var);
23
24         block = eval(fname);
25         block.initializeLibrary('..\')
26
27         display(['Running Block: ' var]);
28         block = block.initializeHardware;
```

```
29          block = block.run;
30
31          block = block.clearTasks;
32
33          clear block;
34      end
35  end
```

A.2 Zeeman slower coil simulation

tilefigs.m is required and is available in Ref. [95].

A.2.1 Coil profile

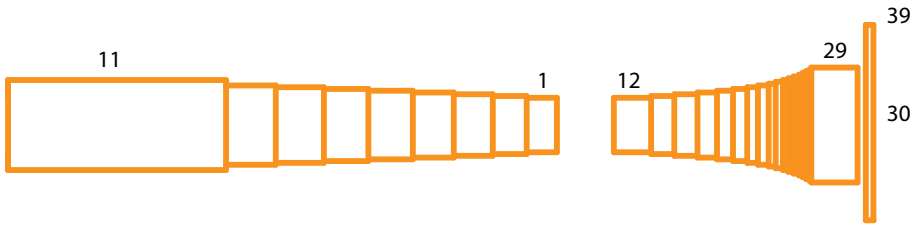

Figure A.2: Coil winding of Zeeman slower.

```
1   Solenoid 1: Length: 308.0 mm
2   Solenoid 2: Length: 291.0 mm
3   Solenoid 3: Length: 272.0 mm
4   Solenoid 4: Length: 250.0 mm
5   Solenoid 5: Length: 227.0 mm
6   Solenoid 6: Length: 203.0 mm
7   Solenoid 7: Length: 177.0 mm
8   Solenoid 8: Length: 150.0 mm
9   Solenoid 9: Length: 123.0 mm
10  Solenoid 10: Length: 96.0 mm
11  Solenoid 11: Length: 73.0 mm
12  Solenoid 12: Length: 149.0 mm
13  Solenoid 13: Length: 119.0 mm
14  Solenoid 14: Length: 108.0 mm
15  Solenoid 15: Length: 96.0 mm
```

```
Solenoid 16: Length: 86.0 mm
Solenoid 17: Length: 76.0 mm
Solenoid 18: Length: 69.0 mm
Solenoid 19: Length: 62.0 mm
Solenoid 20: Length: 56.0 mm
Solenoid 21: Length: 52.0 mm
Solenoid 22: Length: 47.0 mm
Solenoid 23: Length: 44.0 mm
Solenoid 24: Length: 41.0 mm
Solenoid 25: Length: 38.0 mm
Solenoid 26: Length: 36.0 mm
Solenoid 27: Length: 34.0 mm
Solenoid 28: Length: 32.0 mm
Solenoid 29: Length: 30.0 mm
Additional Solenoid 1: Length: 4.2 mm
Additional Solenoid 2: Length: 4.2 mm
Additional Solenoid 3: Length: 4.2 mm
Additional Solenoid 4: Length: 4.2 mm
Additional Solenoid 5: Length: 4.2 mm
Additional Solenoid 6: Length: 4.2 mm
Additional Solenoid 7: Length: 4.2 mm
Additional Solenoid 8: Length: 4.2 mm
Additional Solenoid 9: Length: 4.2 mm
Additional Solenoid 10: Length: 4.2 mm
Additional Solenoid 1: Length: 0.0 mm
WIRE_LENGTH_12 = 1334.74 ft, 406.83 m.
WIRE_LENGTH_34 = 7.27 ft, 2.22 m.
```

A.2.2 zslower.m

```
%% ************ ZEEMAN SLOWER SIMULATION MAIN PROGRAM V4 ******************

% SEO HO YOUN
% LEVLAB, DEPARTMENT OF PHYSICS, UNIVERSITY OF ILLINOIS AT URBANA—CHAMPAIGN
% 11/12/2008
%
% THIS PROGRAM SIMULATES THE PROPER MAGNETIC FIELD PROFILE FOR ZEEMAN
% SLOWER (SPIN—FLIP TYPE) WITHIN SPATIAL UNCERTAINTY OF +/— 1 mm DUE TO
```

```
9  % INDEXING AND DETERMINES THE WIRE WINDING PROFILE.
10 %
11 % ********** MODIFICATION AND ADDITION TO MATLAB V3 *************
12 %
13 % 1. ADDED MAGNETIC FIELD FROM MOT
14 %
15 % ************************************************************
16 %
17 % NOTE: START TO TUNE THE SLOWER WITH THE PARAMETERS ALREADY ASSIGNED IN THE CODE
18 %
19
20 home
21 clear all
22 close all
23
24 %% ************** LOAD PARAMETERS AND INITIALIZE FIELD ******************
25 load_parameters; % Load physical constants, Zeeman slower parmeters, and its configuration
26
27 %% ************** CALCULATE MAGNETIC FIELD FROM MOT COIL ******************
28
29 MOT_field;
30
31 %% ************** INITIALIZE SOLENOIDS ************************
32
33 initialize; % Initialize solenoids
34
35 %% ***************** FIT SECTION I & II ******************
36 fit_solenoids; % Fit all the solenoids to the desired magnetic field
37
38 %% ***************** ADD SOLENOIDS IN SECTION III & IV ************************
39
40 add_solenoids; % Add additional Section III & IV to FIELD
41
42 %% ************* DRAW SECTION I & II *****************
43 draw_field_solenoid; % Draw the desired and simualted magnetic fields and Zeeman slower ...
       structure
44
45 %% ***************** DRAW SOLENOIDS IN SECTION III & IV **********************
46
47 draw_solenoids % Draw additional winding profile of Secition III & IV
```

A.2.3 load_parameters.m

```
function load_parameters

%% ****************** GLOBAL CONSTANTS *************************
global C MU0 PLANCK_CONSTANT BOHR_MAGNETON BOLTZMANN_CONSTANT
global ATOMIC_WAVELENGTH ATOMIC_WAVEVECTOR GAMMA DETUNING OVEN_TEMPERATURE...
    DY_MASS INCOMING_VELOCITY WAVEVECTOR CAPTURE_VELOCITY ACCELERATION_MAX...
    FUDGE_FACTOR MAGNETIC_MOMENT
global INSIDE_RADIUS COIL_SPACING CURRENT_1 CURRENT_2 MAX_LOOP_1 MAX_LOOP_2
global FIELD_LENGTH FIELD_BEFORE FIELD_AFTER MAX_LENGTH FIELD_BEFORE_EXTENSION...
    FIELD_AFTER_EXTENSION CROSSING X_SHIFT_1 X_SHIFT_2 FLAG FIELD_END
global COIL_SPACING_3 COIL_SPACING_4 CURRENT_3 CURRENT_4 INSIDE_RADIUS_3...
    INSIDE_RADIUS_4 STARTING_POSITION_3 STARTING_POSITION_4 SOLENOID_LENGTH_3...
    SOLENOID_LENGTH_4 LAYER_3 LAYER_4 SLOWER_LENGTH SLOWER_START SLOWER_END CF_FLANGE GAP
global DISTANCE_ZSLOWER2MOT COIL_SPACING_MOT CURRENT_MOT N_LOOPS_RHO N_LOOPS_Z R_MIN A_MIN

%% ********* PHYSICAL CONSTANTS **********
C = 29979245800; % Speed of light, cm / s
MU0 = 4 * pi; % Magnetic permeability in air (= 4*pi*10^(-7) N/A^2), G * mm / A
PLANCK_CONSTANT = 6.6261 * 10^(-27) / (2 * pi); % Reduced Planck constant, erg * s
BOHR_MAGNETON = 0.927 * 10^(-20); % erg / G
BOLTZMANN_CONSTANT = 1.380658 * 10^(-16); % erg / K

%% ********** EXPERIMENTAL PARAMETERS ***************
ATOMIC_WAVELENGTH = 421.1714 * 10^(-7); % Atomic wavelength for the transition, cm
ATOMIC_WAVEVECTOR = 2 * pi / ATOMIC_WAVELENGTH; % Atomic wavevector, cm^(-1)
GAMMA = 2.08 * 10^8; % NIST A_ki, s^(-1)
DETUNING = -0.7 * GAMMA - 2 * pi * 2 * 300 * 10^6; % = \omega_l - \omega_a, McClelland 06 ...
    PRL MOT paper, s^(-1), 300 MHz is frequency of AOM
OVEN_TEMPERATURE = 1490; % K
DY_MASS = 162 / (6.022 * 10^23); % g
INCOMING_VELOCITY = sqrt(3 * BOLTZMANN_CONSTANT * OVEN_TEMPERATURE / DY_MASS); % Most ...
    probable velocity of incoming atom beam, cm / s
WAVEVECTOR = (DETUNING + ATOMIC_WAVEVECTOR * C) / C; % Wavevector of laser, cm^(-1)

CAPTURE_VELOCITY = 3000; % Our guessed optimal final velocity coming out of slower to be ...
    captured in MOT, chosen to be 30 m/s by comparing other groups, cm / s

```

```
35 ACCELERATION_MAX = (PLANCK_CONSTANT * WAVEVECTOR * GAMMA) / (2 * DY_MASS); % Maximum ...
       acceleration from recoil, cm / s^2
36 FUDGE_FACTOR = 0.5; % Fudge factor, = s0 / (1 + s0), s0 = I / I_s, 0.4, 0.5, or 0.6
37 MAGNETIC_MOMENT = (1.22 * 9 - 1.24159 * 8) * BOHR_MAGNETON; % Magnetic moment, = (g_{F'} * ...
       M_{F'} - g_F * M_F) * BOHR_MAGNETON, erg / G
38
39 %% ********************** MOT PARAMETERS *********************************
40 % dB/dz at rho = 0 (z is a vertical coordinate and rho is a radial
41 % coordinate) is targetted as about 50 G / cm. (Reference Erbium paper, McClleland)
42
43 DISTANCE_ZSLOWER2MOT = 681; % Distance from the first coil of Zeeman slower to the center ...
       of MOT, mm
44 COIL_SPACING_MOT = 4.2; % mm
45 CURRENT_MOT = 60; %A
46 N_LOOPS_RHO = 7; % 7
47 N_LOOPS_Z = 10; % 10
48 R_MIN = 6.3 * 2.54 * 10 / 2 + COIL_SPACING_MOT / 2; % The radius of the most inner loop, mm
49 A_MIN = 2.78 /2 * 2.54 * 10 + COIL_SPACING_MOT / 2; % The distance from the center of MOT ...
       to the center of most bottom coil, mm
50
51 %% ********* ZEEMAN SLOWER PARAMETERS OF SECTION I & II **********
52 INSIDE_RADIUS = 14.2875;           % The radius of the Copper tube (diameter of 1 1/8" = ...
       28.575 mm), mm
53 COIL_SPACING = 1;             % The thickness of coil (wire), mm
54
55 CURRENT_1 = 2.7;                % Current in Section I (the one far from MOT), A
56 CURRENT_2 = -2.6;               % Current in Section II (the one close from MOT), A
57 % \eta = 0.4 -> CURRENT_1 = 2.65, CURRENT_2 = -2.8
58 % \eta = 0.5 -> CURRENT_1 = 2.7, CURRENT_2 = -2.8
59 % \eta = 0.6 -> CURRENT_1 = 2.7, CURRENT_2 = -2.8
60
61 MAX_LOOP_1 = 11;                % Last solenoid of Section I in simulation
62 MAX_LOOP_2 = 29;                % Last solenoid of Section II in simulation
63 % \eta = 0.4, MAX_LOOP_1 = 11, MAX_LOOP_2 = 28
64 % \eta = 0.5, MAX_LOOP_1 = 11, MAX_LOOP_2 = 29
65 % \eta = 0.6, MAX_LOOP_1 = 11, MAX_LOOP_2 = 29
66
67 FIELD_BEFORE_EXTENSION = 60; % Extension of simulation, mm
68 FIELD_AFTER_EXTENSION = 40;  % Extension of simulation, mm
69 % \eta = 0.4 -> FIELD_BEFORE_EXTENSION = 60, FIELD_AFTER_EXTENSION = 40
```

```
% \eta = 0.5 -> FIELD_BEFORE_EXTENSION = 60, FIELD_AFTER_EXTENSION = 40
% \eta = 0.6 -> FIELD_BEFORE_EXTENSION = 60, FIELD_AFTER_EXTENSION = 40

FIELD_LENGTH = round((INCOMING_VELOCITY^2 - CAPTURE_VELOCITY^2) / (2 * FUDGE_FACTOR * ...
    ACCELERATION_MAX) * 10); % Length of the field that actually matters, mm
FIELD_BEFORE = 300;             % Gap before Zeeman slower, mm
FIELD_AFTER = 300;          % Gap after Zeeman slower, mm
MAX_LENGTH = FIELD_BEFORE - FIELD_BEFORE_EXTENSION + DISTANCE_ZSLOWER2MOT;      % Length ...
    of whole physical simulation, mm

CROSSING = round(FIELD_BEFORE + INCOMING_VELOCITY^2 / (2 * FUDGE_FACTOR * ...
    ACCELERATION_MAX) *...
    (1 - (DETUNING / (WAVEVECTOR * INCOMING_VELOCITY))^2) * 10); % Crossing point of B = 0 ...
        from z = 1, mm

X_SHIFT_1 = 7; % X Shift of the Section I of artificially fitted field (x_shift1 > 0 ...
    always, to -z direction), mm
X_SHIFT_2 = 17; % X Shift of the Section II of artificially fitted field (x_shift2 > 0 ...
    always, to +z direction), mm
% \eta = 0.4, X_SHIFT_1 = 5, X_SHIFT_2 = 18
% \eta = 0.5, X_SHIFT_1 = 7, X_SHIFT_2 = 17
% \eta = 0.6, X_SHIFT_1 = 7, X_SHIFT_2 = 17

FLAG = 1; % 0 -> chiSq is evealuated ONLY from field length, 1 -> chiSq is evaluated from ...
    the WHOLE simulated interval

FIELD_END = FIELD_BEFORE + FIELD_LENGTH; % Field end from z = 1, where field is the ...
    minimum, mm
%% ************ ZEEMAN SLOWER PARAMETERS OF SECTION III & IV **********

COIL_SPACING_3 = 4.2; % 4.2 mm diameter for bigger wire with water through, 1 mm diameter ...
    for smaller wire, mm
COIL_SPACING_4 = 1; % mm

SOLENOID_LENGTH_3 = COIL_SPACING_3  * [1 1 1 1 1 1 1 1 1 1];
SOLENOID_LENGTH_4 = COIL_SPACING_4 * [0];
% Length of Section III & IV which determines turn of windings, mm
% 5 layers of 4.2 mm wire of Section III are maximum not to go over the CF flange, but we ...
    may have more with additional construction.
% \eta = 0.4, SOLENOID_LENGTH_3 = [1 1 1 1 1 1 1 1 1 1], SOLENOID_LENGTH_4 = [0]
```

```
% \eta = 0.5, SOLENOID_LENGTH_3 = [1 1 1 1 1 1 1 1 1 1 1], SOLENOID_LENGTH_4 = [0]
% \eta = 0.6, SOLENOID_LENGTH_3 = [1 1 1 1 1 1 1 1 1 1 1], SOLENOID_LENGTH_4 = [0]

CURRENT_3 = 41; % Current of Section III, A
CURRENT_4 = 0; % Current of Section IV, A
% \eta = 0.4, CURRENT_3 = 38, CURRENT_4 = 0
% \eta = 0.5, CURRENT_3 = 41, CURRENT_4 = 0
% \eta = 0.6, CURRENT_3 = 39, CURRENT_4 = 0

CF_FLANGE = 12.7; % 1/2" (12.7 mm, thickness of 2-3/4" OD CF flange), mm

INSIDE_RADIUS_3 = 14.2875;
INSIDE_RADIUS_4 = 9.525;
% Outer diameter of tubes for Section III & IV, mm
% 14.2875 mm copper tube OD, 9.525 mm stainless steel tube OD

GAP = COIL_SPACING_3;

STARTING_POSITION_3 = FIELD_END + FIELD_AFTER_EXTENSION + 1/2 + 1/2 * COIL_SPACING_3 + GAP;
STARTING_POSITION_4 = FIELD_END + FIELD_AFTER_EXTENSION + 1/2 + SOLENOID_LENGTH_3(1)...
    + 1/2 * COIL_SPACING_4 + CF_FLANGE;
% Starting position of Section III & IV from z = 1, mm

LAYER_3 = length(SOLENOID_LENGTH_3); % Number of layers of solenoids in Section III & IV
LAYER_4 = length(SOLENOID_LENGTH_4);

%% ********* SLOWER_LENGTH CALCULATION BY CASE AND SLOWER_END *********

SLOWER_LENGTH = FIELD_LENGTH + FIELD_BEFORE_EXTENSION + FIELD_AFTER_EXTENSION...
    + 2 * 1/2 + GAP + SOLENOID_LENGTH_3(1);
% The length of a tube needed for Zeeman slower, mm
% 2 * 1/2 mm -> takes account of two halves of winding at two ends of Section I & II

SLOWER_START = FIELD_BEFORE - FIELD_BEFORE_EXTENSION;
SLOWER_END = FIELD_LENGTH + FIELD_BEFORE + FIELD_AFTER_EXTENSION + 1/2 + GAP + 1/2 * ...
    SOLENOID_LENGTH_3(1); % Physical slower end from z = 1, mm
```

A.2.4 MOT_field.m

```
% scans and computes the magnetic field for the given ranges from rho_min to rho_max and ...
    from z_min to z_max
% rho_min, rho_max, z_min, z_max in mm
% scanNplot(rho_min, rho_max, z_min, z_max, A_min, R_min, I, n_loops_rho, n_loops_z, ...
    coil_diameter, direction)
% direction: 1 for pairs of current loops in the SAME direction (Helmholtz configuration)
% direction: -1 for pairs of current loops in the OPPOSITE direction(Anti-Helmholtz ...
    configuration)
% rho and z are the coordinates of MOT (NOTE THAT THESE ARE DIFFERENT FROM THOSE IN ZSLOWER)

function MOT_field

global MAX_LENGTH A_MIN R_MIN CURRENT_MOT N_LOOPS_RHO N_LOOPS_Z COIL_SPACING_MOT MOT_FIELD

MOT_FIELD = zeros(MAX_LENGTH, 1);
B_rho_1 = zeros(N_LOOPS_RHO, N_LOOPS_Z);
z = 0;

for  m = 1 : MAX_LENGTH

    rho = MAX_LENGTH - m;

    for j = 1 : N_LOOPS_Z % number of loops in z direction

        for i = 1 : N_LOOPS_RHO % number of loops in rho direction

            A = A_MIN + (j - 1) * COIL_SPACING_MOT;
            R = R_MIN + (i - 1) * COIL_SPACING_MOT;

            %***** Upper Coil *****%
            [B_rho_u, B_z_u] = B_field(rho, z, R, A, CURRENT_MOT);


            %***** Lower Coil *****%
            [B_rho_l, B_z_l] = B_field(rho, z, R, -A, -CURRENT_MOT);

            B_rho_1(i,j) = -(B_rho_u + B_rho_l); % B_rho due to one pair of current loop

        end

```

```
38      end
39
40      MOT_FIELD(m) = MOT_FIELD(m) + sum(sum(B_rho_1)); % G
41
42  end
```

A.2.5 initialize.m

```
1   %% ************** INITIALIZE GLOBAL CONSTANTS AND VARIABLES ***************
2
3   function initialize
4
5   global DESIRED FIELD FITTED FLAG FIELD_BEFORE X_SHIFT_1 DETUNING INCOMING_VELOCITY...
6       WAVEVECTOR PLANCK_CONSTANT MAGNETIC_MOMENT CROSSING FUDGE_FACTOR ACCELERATION_MAX...
7       X_SHIFT_2 FIELD_LENGTH MAX_LENGTH MAX_LOOP_1 MAX_LOOP_2 FIELD_BEFORE_EXTENSION...
8       FIELD_AFTER_EXTENSION CURRENT_1 CURRENT_2 SOLENOID FIELD_END MOT_FIELD MEASURED_Z...
9       MEASURED_FIELD
10
11  %% ************** INITIALIZE FIELDS ********************
12  DESIRED = zeros(MAX_LENGTH, 1); % Desired (theoretical) field
13  FIELD = MOT_FIELD; % Simulated field, initially MOT_FIELD is assigned
14  FITTED = zeros(MAX_LENGTH, 1); % Artificially fitted field to which the simulated field is ...
        fitted
15
16
17  %% *************** MAKE ARTIFICIALLY FITTED FIELD ****************************
18
19  for z = 1 : FIELD_BEFORE - X_SHIFT_1 - 1
20      if FLAG == 0
21          FITTED(z) = 0;
22      else
23          FITTED(z) = (DETUNING + INCOMING_VELOCITY * WAVEVECTOR) * PLANCK_CONSTANT / ...
                MAGNETIC_MOMENT;
24      end
25  end
26
27  for z = FIELD_BEFORE - X_SHIFT_1 : CROSSING - X_SHIFT_1
```

```
28      FITTED(z) = PLANCK_CONSTANT * DETUNING / MAGNETIC_MOMENT + PLANCK_CONSTANT * ...
            INCOMING_VELOCITY * WAVEVECTOR / MAGNETIC_MOMENT *...
29          sqrt(1 - (2 * FUDGE_FACTOR * ACCELERATION_MAX * (z - FIELD_BEFORE + X_SHIFT_1) / ...
                10) / INCOMING_VELOCITY^2);
30  end
31
32  for z = CROSSING - X_SHIFT_1 + 1 : CROSSING + X_SHIFT_2
33      FITTED(z) = 0;
34  end
35
36  for z = CROSSING + X_SHIFT_2 + 1 : FIELD_END + X_SHIFT_2
37      FITTED(z) = PLANCK_CONSTANT * DETUNING / MAGNETIC_MOMENT + PLANCK_CONSTANT * ...
            INCOMING_VELOCITY * WAVEVECTOR / MAGNETIC_MOMENT *...
38          sqrt(1 - (2 * FUDGE_FACTOR * ACCELERATION_MAX * (z - FIELD_BEFORE - X_SHIFT_2) / ...
                10) / INCOMING_VELOCITY^2);
39  end
40
41  for z = FIELD_END + X_SHIFT_2 + 1 : MAX_LENGTH
42      if FLAG == 0
43          FITTED(z) = 0;
44      else
45          FITTED(z) = PLANCK_CONSTANT * DETUNING / MAGNETIC_MOMENT + PLANCK_CONSTANT * ...
                INCOMING_VELOCITY * WAVEVECTOR / MAGNETIC_MOMENT *...
46              sqrt(1 - (2 * FUDGE_FACTOR * ACCELERATION_MAX * FIELD_LENGTH / 10) / ...
                    INCOMING_VELOCITY^2);
47      end
48  end
49
50  %% *************** MAKE DESIRED FIELD *****************************
51  for z = 1 : FIELD_BEFORE - 1
52      DESIRED(z) = 0;
53  end
54  for z = FIELD_BEFORE : FIELD_BEFORE + FIELD_LENGTH
55      DESIRED(z) = PLANCK_CONSTANT * DETUNING / MAGNETIC_MOMENT + PLANCK_CONSTANT * ...
            INCOMING_VELOCITY * WAVEVECTOR / MAGNETIC_MOMENT *...
56          sqrt(1 - (2 * FUDGE_FACTOR * ACCELERATION_MAX * (z - FIELD_BEFORE) / 10) / ...
                INCOMING_VELOCITY^2);
57  end
58  for z = FIELD_BEFORE + FIELD_LENGTH + 1 : MAX_LENGTH
59      DESIRED(z) = 0;
```

```
60 end
61
62 %% ***************** INITIALIZE SOLENOIDS *************************
63 for a = 1 : MAX_LOOP_1
64     SOLENOID(a).START_I = FIELD_BEFORE - FIELD_BEFORE_EXTENSION;
65     SOLENOID(a).MAX_LENGTH = CROSSING - FIELD_BEFORE + FIELD_BEFORE_EXTENSION;
66     SOLENOID(a).LAYER = a;
67     SOLENOID(a).CURRENT = CURRENT_1;
68     SOLENOID(a).LENGTH = 0;
69 end
70
71 for a = (MAX_LOOP_1 + 1) : MAX_LOOP_2
72     SOLENOID(a).START_I = FIELD_LENGTH + FIELD_BEFORE + FIELD_AFTER_EXTENSION;
73     SOLENOID(a).MAX_LENGTH = FIELD_END - CROSSING + FIELD_AFTER_EXTENSION;
74     SOLENOID(a).LAYER = a - MAX_LOOP_1;
75     SOLENOID(a).CURRENT = CURRENT_2;
76     SOLENOID(a).LENGTH = 0;
77 end
78
79 %% ****************** MEASURED FIELD ********************************
80
81 temp = csvread('field_measurement.csv');
82 MEASURED_Z = temp(:,1);
83 MEASURED_FIELD = temp(:,2);
84
85 %plot(MEASURED_Z_LEFT, MEASURED_FIELD_LEFT, '*r', MEASURED_Z_RIGHT, MEASURED_FIELD_RIGHT, ...
       '*r')
```

A.2.6 fit_solenoids.m

```
1 %% ************** FIT ALL SOLENOIDS OF SECTION I & II TO THE FIELD *****************
2
3
4 function fit_solenoids
5
6 global MAX_LOOP_1 MAX_LOOP_2
7 global SOLENOID
8
```

```
%** FIT SOLENOIDS IN SECTION I ***
check = 1;
a = 1;
while (a <= MAX_LOOP_1) && (check == 1)
    check = fit_solenoid(a, 1);

    if check
        fprintf('Solenoid %d: Length: %.1f mm\n', a, SOLENOID(a).LENGTH)
    end
    a = a + 1;
end

%** FIT SOLENOIDS IN SECTION II ***
check = 1;
a = MAX_LOOP_1 + 1;
while (a <= MAX_LOOP_2) && (check == 1)
    check = fit_solenoid(a, -1);
    if check
        fprintf('Solenoid %d: Length: %.1f mm\n', a, SOLENOID(a).LENGTH)
    end
    a = a + 1;
end


%% ***************** SUBFUNCTIONS START *************************
% ******************************************************************

%*** FIT AN INDIVIDUAL SOLENOID TO THE fitted FIELD WITHIN GIVEN LIMITS ***
function check = fit_solenoid(a, direction)

global SOLENOID INSIDE_RADIUS COIL_SPACING
global TEMP_FIELD FIELD

TEMP_FIELD = FIELD;
modified = 0;
current = SOLENOID(a).CURRENT;
radius = (SOLENOID(a).LAYER - 0.5) * COIL_SPACING + INSIDE_RADIUS;

max_chiSq = chi_sq;

```

```
49 for i = 0 : SOLENOID(a).MAX_LENGTH - 1
50
51     position = SOLENOID(a).START_I + direction * i * COIL_SPACING;
52     add_dz_section (radius, position, current);
53     chiSq = chi_sq;
54
55     if chiSq > max_chiSq
56         break
57     end
58
59     FIELD = TEMP_FIELD;
60     max_chiSq = chiSq;
61     modified = 1;
62
63 end
64
65 if (modified) && ((i - 1) >= 1)
66     SOLENOID(a).LENGTH = i - 1;
67     check = modified;
68 else
69     SOLENOID(a).LENGTH = 0;
70     check = 0;
71 end
72
73 % ************** ADD THE FIELD FROM A TINY SOLENOID SECTION **************
74 function add_dz_section(radius, position, current)
75
76 global MU0 MAX_LENGTH TEMP_FIELD COIL_SPACING
77
78 rsq = radius * radius;
79 junk = MU0 * current * rsq;
80 twospacing = 2 * COIL_SPACING;
81
82 for z = 1 : MAX_LENGTH
83     TEMP_FIELD(z) = TEMP_FIELD(z) + junk / (twospacing * power((rsq + power(z - position, ...
         2)), 1.5));
84 end
85
86 % ************** COMPUTE CHI SQUARED ******************
87 function chiSq = chi_sq
```

```
88
89 global FITTED TEMP_FIELD FIELD_BEFORE X_SHIFT_1 FIELD_LENGTH X_SHIFT_2 CROSSING FLAG
90
91 delta = abs(FITTED - TEMP_FIELD);
92
93 if FLAG == 0
94     chiSq = sum(delta(FIELD_BEFORE - X_SHIFT_1 : CROSSING - X_SHIFT_2).^2) + ...
           sum(delta(CROSSING + X_SHIFT_2 + 1 : FIELD_BEFORE + FIELD_LENGTH + X_SHIFT_2).^2);
95 else
96     chiSq = sum(delta.^2);
97 end
```

A.2.7 add_solenoids.m

```
1  %% ************* ADD ADITIONAL SOLENOIDS IN SECTION III & IV *************
2
3  function add_solenoids
4
5  global MU0 LAYER_3 CURRENT_3 INSIDE_RADIUS_3 COIL_SPACING_3 MAX_LENGTH FIELD...
6      LAYER_4 CURRENT_4 INSIDE_RADIUS_4 COIL_SPACING_4 STARTING_POSITION_3...
7      STARTING_POSITION_4 SOLENOID_LENGTH_3 SOLENOID_LENGTH_4
8
9  for a = 1 : LAYER_3
10
11     fprintf('Additional Solenoid %d: Length: %.1f mm\n', a, SOLENOID_LENGTH_3(a))
12
13     radius = (a - 0.5) * COIL_SPACING_3 + INSIDE_RADIUS_3;
14     rsq = radius * radius;
15     junk = MU0 * CURRENT_3 * rsq;
16     twospacing = 2 * COIL_SPACING_3;
17
18     for i = 0 : SOLENOID_LENGTH_3(a) - 1
19         position = STARTING_POSITION_3 + i * COIL_SPACING_3;
20
21         for z = 1 : MAX_LENGTH
22             FIELD(z) = FIELD(z) + junk / (twospacing * power((rsq + power(z - position, ...
                   2)), 1.5));
23         end
```

```
24
25      end
26  end
27
28  for a = 1 : LAYER_4
29
30      fprintf('Additional Solenoid %d: Length: %.1f mm\n', a, SOLENOID_LENGTH_4(a))
31
32      radius = (a - 0.5) * COIL_SPACING_4 + INSIDE_RADIUS_4;
33      rsq = radius * radius;
34      junk = MU0 * CURRENT_4 * rsq;
35      twospacing = 2 * COIL_SPACING_4;
36
37      for i = 0 : SOLENOID_LENGTH_4(a) - 1
38          position = STARTING_POSITION_4 + i * COIL_SPACING_4;
39
40          for z = 1 : MAX_LENGTH
41              FIELD(z) = FIELD(z) + junk / (twospacing * power((rsq + power(z - position, ...
                    2)), 1.5));
42          end
43
44      end
45  end
```

A.2.8 draw_field_solenoid.m

```
1   %************** DRAW THE MAGNETIC FIELDS AND SOLENOID STRUCTURE ******************************
2   function draw_field_solenoid
3
4
5   global MAX_LENGTH FIELD FITTED DESIRED COIL_SPACING MAX_LOOP_1...
6       MAX_LOOP_2 SOLENOID INSIDE_RADIUS FIELD_LENGTH FIELD_BEFORE...
7       SLOWER_END SLOWER_LENGTH FUDGE_FACTOR OVEN_TEMPERATURE CAPTURE_VELOCITY...
8       WIRE_LENGTH_12 SLOWER_START MOT_FIELD MEASURED_Z MEASURED_FIELD
9
10  %% ********************** DRAW FITTED AND SIMULATED MAGNETIC FIELDS ******************
11
```

```
12 last_slowing_point = find(FIELD == min(FIELD)); % Actual last point where slowing ...
       scattering occurs, mm from z = 0, NOT equal to FIELD_END
13
14 % DRAW FIGURE 1
15 figure
16 plot(1 : MAX_LENGTH, FIELD, ':b', 1 : MAX_LENGTH, FITTED, '--g', 1 : MAX_LENGTH, DESIRED, ...
       '-r', 1 : MAX_LENGTH, FIELD - MOT_FIELD, '-k', MEASURED_Z, MEASURED_FIELD, '*r')
17 xlabel('distance of Zeeman slower along the atom beam (mm)')
18 ylabel('magnetic field (Gauss)')
19 title_fig1 = sprintf('Plot of Fitted and Simulated Magnetic Fields, \\eta = %.1f, oven ...
       temp. = %d K, v_f = %d m/s',FUDGE_FACTOR, OVEN_TEMPERATURE, CAPTURE_VELOCITY/100);
20 title(title_fig1)
21 legend('simulated field','artificially fitted field','desired field', 'simulated field - ...
       MOT field', 'measured data (B_z) with MOT OFF', 1)
22
23 range_fig_1 = 400;
24 line([SLOWER_START SLOWER_START], [-range_fig_1 range_fig_1])
25 line([last_slowing_point last_slowing_point], [-range_fig_1 range_fig_1])
26 line([SLOWER_END SLOWER_END], [-range_fig_1 range_fig_1])
27 line([MAX_LENGTH MAX_LENGTH], [-range_fig_1 range_fig_1])
28 text(SLOWER_START + 10, -range_fig_1, 'First Coil','rotation', 90);
29 text(last_slowing_point + 10, -range_fig_1, 'Last Slowing Point', 'rotation', 90);
30 text(SLOWER_END + 10, -range_fig_1, 'Last Coil', 'rotation', 90);
31 text(MAX_LENGTH + 10, -range_fig_1, 'Center of MOT', 'rotation', 90);
32
33 % DRAW FIGURE 2
34 figure
35 difference = DESIRED - FIELD;
36 plot(1 : MAX_LENGTH, difference, '.k')
37 xlabel('distance of Zeeman slower along the atom beam (mm)')
38 ylabel('desired field - simulated field (Gauss)')
39 title_fig2 = sprintf('Plot of Difference in Simulation, \\eta = %.1f, oven temp. = %d K, ...
       v_f = %d m/s',FUDGE_FACTOR, OVEN_TEMPERATURE, CAPTURE_VELOCITY/100);
40 title(title_fig2)
41 axis([FIELD_BEFORE FIELD_BEFORE+FIELD_LENGTH -5 5])
42
43 % % DRAW FIGURE 3
44 % figure
45 % plot(1 : MAX_LENGTH, difference, '.k')
46 % xlabel('distance of Zeeman slower along the atom beam (mm)')
```

```
% ylabel('desired field − simulated field (Gauss)')
% title_fig3 = sprintf('Plot of Difference in Simulation, \\eta = %.1f, oven temp. = %d K, ...
    v_f = %d m/s',FUDGE_FACTOR, OVEN_TEMPERATURE, CAPTURE_VELOCITY/100);
% title(title_fig3)
% %range_fig_3 = 1;
%
% gradient = (FIELD(MAX_LENGTH) − FIELD(MAX_LENGTH − 1)) * 10; % Field gradient (dBz/dz, G ...
    / cm) at the center of MOT
% gradient_fig = sprintf('%.2f G/cm',gradient);
% text(MAX_LENGTH, 0, gradient_fig);
%
% line([SLOWER_START SLOWER_START], [−range_fig_3 range_fig_3])
% line([last_slowing_point last_slowing_point], [−range_fig_3 range_fig_3])
% line([SLOWER_END SLOWER_END], [−range_fig_3 range_fig_3])
% line([MAX_LENGTH MAX_LENGTH], [−range_fig_3 range_fig_3])
% text(SLOWER_START + 10, −range_fig_3, 'First Coil','rotation', 90);
% text(last_slowing_point + 10, −range_fig_3, 'Last Slowing Point', 'rotation',90);
% text(SLOWER_END + 10, −range_fig_3, 'Last Coil', 'rotation', 90);
% text(MAX_LENGTH + 10 , −range_fig_3, 'Center of MOT', 'rotation', 90);
%
% axis([last_slowing_point last_slowing_point+300 −range_fig_3 range_fig_3])

% DRAW FIGURE 3 gradient
figure
plot(1.5 : MAX_LENGTH − 0.5, diff(FIELD) * 10, '.k')
xlabel('distance of Zeeman slower along the atom beam (mm)')
ylabel('dBz/dz (Gauss / cm)')
title_fig3 = sprintf('Plot of dBz/dz in Simulation, \\eta = %.1f, oven temp. = %d K, v_f = ...
    %d m/s',FUDGE_FACTOR, OVEN_TEMPERATURE, CAPTURE_VELOCITY/100);
title(title_fig3)
axis([MAX_LENGTH − 10 MAX_LENGTH −24.5 −23.5])



%% ****** DRAW ZEEMAN SLOWER STRUCTURE **************

WIRE_LENGTH_12 = 0; % Total length of wire in Section I & II

% DRAW FIGURE 4
figure
```

```
84  hold on
85  axis equal
86  axis([0 MAX_LENGTH 0 70 * COIL_SPACING])
87  xlabel('distance of Zeeman slower along the atom beam (mm)')
88  ylabel('radial distance (mm)')
89  title_fig4 = sprintf('Coil Profile of Zeeman Slower, \\eta = %.1f, oven temp. = %d K, v_f ...
        = %d m/s',FUDGE_FACTOR, OVEN_TEMPERATURE, CAPTURE_VELOCITY/100);
90  title(title_fig4)
91  text_fig4 = sprintf('The length of copper tube required is %.2f mm.', SLOWER_LENGTH);
92  text(0 , -120 , text_fig4)
93
94
95  %% ********* MAKE A FILE FOR AUTOCAD DRAWING (ONLY SECTION I & II DRAWN) *************
96  fid = fopen('drawing.scr','w');
97
98  fprintf(fid,'multiple\n');
99  fprintf(fid,'circle \n');
100 mm2inch = 1 / 25.4; % mm to inch conversion for AutoCAD
101
102 %% ******************************************************
103
104 for a = 1 : MAX_LOOP_2
105     if SOLENOID(a).CURRENT == 0;
106         continue;
107     end
108     if a <= MAX_LOOP_1
109         direction = +1; % Scanning direction (+1 -> along +z-axis)
110     else
111         direction = -1;
112     end
113
114     for i = 0 : (SOLENOID(a).LENGTH - 1) / COIL_SPACING
115
116         z = SOLENOID(a).START_I + direction * i * COIL_SPACING;
117         x = (SOLENOID(a).LAYER - 0.5)* COIL_SPACING + INSIDE_RADIUS;
118         plot(z, x,'.k');
119
120         WIRE_LENGTH_12 = 2 * pi * x + WIRE_LENGTH_12;
121
122         %% ****** DRAWING FOR AUTOCAD, POSITION AND RADIUS ****
```

```
123          fprintf(fid, '%f,%f\n', z * mm2inch, x * mm2inch);
124          fprintf(fid, '%f\n', COIL_SPACING / 2 * mm2inch);
125          %% ***************************************************
126
127      end
128  end
129
130  fprintf('WIRE_LENGTH_12 = %.2f ft, %.2f m.\n', WIRE_LENGTH_12 * 0.00328083, WIRE_LENGTH_12 ...
         * 10^(-3));
131
132  tilefigs([2 2], 50)
133
134  fclose(fid);
```

A.2.9 draw_solenoids.m

```
1   %% ***************** DRAW ADDITIONAL SOLENOIDS *********************
2
3   function draw_solenoids
4
5   global LAYER_3 STARTING_POSITION_3 SOLENOID_LENGTH_3 COIL_SPACING_3...
6       INSIDE_RADIUS_3 LAYER_4 STARTING_POSITION_4 SOLENOID_LENGTH_4 COIL_SPACING_4...
7       INSIDE_RADIUS_4 CURRENT_3 CURRENT_4 WIRE_LENGTH_34
8
9   WIRE_LENGTH_34 = 0; % Total length of wire in Section III & IV
10
11  for a = 1:LAYER_3
12
13      if CURRENT_3 == 0;
14          continue;
15      end
16
17      for  i = 0 : (SOLENOID_LENGTH_3(a) -1) / COIL_SPACING_3
18
19          z = STARTING_POSITION_3 + i * COIL_SPACING_3;
20          x = (a - 0.5) * COIL_SPACING_3 + INSIDE_RADIUS_3;
21          plot(z, x,'.k');
22
```

```
        WIRE_LENGTH_34 = 2 * pi * x + WIRE_LENGTH_34;

    end
end

for a = 1:LAYER_4

    if CURRENT_4 == 0;
        continue;
    end

    for  i = 0 : (SOLENOID_LENGTH_4(a) -1) / COIL_SPACING_4

        z = STARTING_POSITION_4 + i * COIL_SPACING_4;
        x = (a - 0.5) * COIL_SPACING_4 + INSIDE_RADIUS_4;
        plot(z, x,'.k');

        WIRE_LENGTH_34 = 2 * pi * x + WIRE_LENGTH_34;

    end

end

fprintf('WIRE_LENGTH_34 = %.2f ft, %.2f m.\n', WIRE_LENGTH_34 * 0.00328083, WIRE_LENGTH_34 ...
    * 10^(-3));
```

A.2.10 B_field.m

```
% Computes the components of magnetic field (unit of G) due to a loop of coil with current
% rho, z, R, A in mm
% I in A (Ampere)

function [B_rho, B_z] = B_field(rho, z, R, A, I)

global MU0

% argument of complete elliptical integral
k = sqrt(4 * R * rho / ((R + rho)^2 + (z - A)^2));
```

```
11
12 alpha = 0 : pi/200 : pi/2; % limits used in elliptical integrals
13
14 % first term involving elliptical integrals in B_rho
15 integrand_1_rho = (sin(alpha).^2 - 1) ./ ((1 - k^2) * sqrt(1 - k^2 * sin(alpha).^2));
16 ellip_int_term_1_rho = 4 * R / ((R + rho)^2 + (z - A)^2) * trapz(alpha , integrand_1_rho);
17
18 % second term involving elliptical integral in B_rho
19 integrand_2_rho = sqrt(1 - k^2 * sin(alpha).^2);
20 ellip_int_term_2_rho = 2 * R / ((1 - k^2) * ((R + rho)^2 + (z - A)^2)) * trapz(alpha, ...
       integrand_2_rho);
21
22 % computes B_rho at a point of interest
23 B_rho = - MU0 * I * (z - A) / (2 * pi) / sqrt((R + rho)^2 + (z - A)^2)...
24     * (ellip_int_term_1_rho + ellip_int_term_2_rho);
25
26 % first term involving elliptical integrals in B_z
27 integrand_1_z = 1 ./ sqrt(1 - k^2 * sin(alpha).^2);
28 ellip_int_term_1_z = trapz(alpha , integrand_1_z);
29
30 % second term involving elliptical integral in B_z
31 integrand_2_z = sqrt(1 - k^2 * sin(alpha).^2);
32 ellip_int_term_2_z = (2 * R * (R + rho) / (((R + rho)^2 + (z - A)^2) * (1 - k^2)) - 1 / (1 ...
       - k^2)) * trapz(alpha, integrand_2_z);
33
34 % th
35 B_z = MU0 * I / (2 * pi) / sqrt((R + rho)^2 + (z - A)^2) * (ellip_int_term_1_z + ...
       ellip_int_term_2_z);
```

A.3 Quadrupole field coil simulation

B_field.m is written in Appendix A.2.10.

A.3.1 MOT_COIL.m

```
1 % ********** THIS PROGRAM IS ONLY FOR CIRCULAR MOT COIL. **********
2
3 % COMPUTES AND PLOT THE MAGNETIC FIELD FROM MANY PAIRS OF CURRENT LOOPS
```

```
4  % IN THE SAME OR THE OPPSITE DIRECTIONS
5
6  clear
7  close all
8  home
9
10 %% PARAMETERS USED IN THIS SIMULATION
11 global mu0
12
13 d = -1;
14 % direction of current
15 % -1 (opposite direction) for Anti-Helmholtz configuration, +1 (same direction) for ...
       Helmtholtz configuration
16 % -1 for MOT coil
17
18 mu0 = 4 * pi; % permeability for free space (close to air), G mm / A
19
20 coil_diameter = 4.2;
21 % diameter of wire used, mm
22
23 I = 60;
24 % electric current used, A
25
26 n_loops_rho = 7;
27 % number of turns in rho direction
28
29 n_loops_z = 10;
30 % number of turns in z direction
31
32 A_min = 2.78 /2 * 25.4 + coil_diameter / 2;
33 % the distance from the center of MOT to the center of bottom most coil, mm
34
35 R_min = 6.3 * 25.4 / 2 + coil_diameter / 2;
36 % the radius of the most inner loop, mm
37
38 %% MAIN SCRIPT
39
40 [B_rho, B_z] = scanNsum_field(0, 300, 0, 0, A_min, R_min, I, n_loops_rho, n_loops_z, ...
       coil_diameter, d);
41
```

```
plot_field(0, 300, 0, 0, B_rho, B_z, d)

[B_rho, B_z] = scanNsum_field(0, 0, -500, 500, A_min, R_min, I, n_loops_rho, n_loops_z, ...
    coil_diameter, d);

plot_field(0, 0, -500, 500, B_rho, B_z, d)
```

A.3.2 scanNsum_field.m

```
% scans and computes the magnetic field for the given ranges from rho_min
% to rho_max and from z_min to z_max
% plots the results
% rho_min, rho_max, z_min, z_max in mm

function [B_rho, B_z] = scanNsum_field(rho_min, rho_max, z_min, z_max, A_min, R_min, I, ...
    n_loops_rho, n_loops_z, coil_diameter, d)

n = 100; % division (number of steps) between rho_min and rho_max or z_min and z_max
drho = (rho_max - rho_min) / n;
dz = (z_max - z_min) / n;

% initialize B field variables
B_rho_1 = zeros(n_loops_rho, n_loops_z);
B_z_1 = zeros(n_loops_rho, n_loops_z);
B_rho = zeros(1, n + 1);
B_z = zeros(1, n + 1);

for m = 1 : n + 1

    rho = rho_min + (m - 1) * drho;
    z = z_min + (m - 1) * dz;

    for j = 1 : n_loops_z % number of loops in z direction

        for i = 1 : n_loops_rho % number of loops in rho direction

            A = A_min + (j - 1) * coil_diameter;
            R = R_min + (i - 1) * coil_diameter;
```

```
29
30              %***** Upper Coil *****%
31              [B_rho_u, B_z_u] = B_field(rho, z, R, A, I);
32
33              %***** Lower Coil *****%
34              [B_rho_l, B_z_l] = B_field(rho, z, R, -A, d*I);
35
36              B_rho_1(i,j) = B_rho_u + B_rho_l; % B_rho due to one pair of current loop
37              B_z_1(i,j) = B_z_u + B_z_l; % B_z due to one pair of current loop
38
39          end
40
41      end
42
43      B_rho(m) = B_rho(m) + sum(sum(B_rho_1)); % G
44      B_z(m) = B_z(m) + sum(sum(B_z_1)); % G
45
46  end
```

A.3.3 plot_field.m

```
1   function plot_field(rho_min, rho_max, z_min, z_max, B_rho, B_z, d)
2
3   %% *** LOAD DATA OF MEASURED FIELD ***
4
5   temp1 = csvread('MOT_separate.csv');
6   temp2 = csvread('MOT_together.csv');
7
8   MEASURED_RHO_1 = temp1(:,1);
9   MEASURED_FIELD_RHO_1 = temp1(:,2);
10
11  MEASURED_Z_1 = temp1(:,3);
12  MEASURED_FIELD_Z_1 = temp1(:,4);
13
14  MEASURED_RHO_2 = temp2(:,1);
15  MEASURED_FIELD_RHO_2 = temp2(:,2);
16
17  MEASURED_Z_2 = temp2(:,3);
```

```
MEASURED_FIELD_Z_2 = temp2(:,4);


%%

n = 100; % division (number of steps) between rho_min and rho_max or z_min and z_max
drho = (rho_max - rho_min) / n;
dz = (z_max - z_min) / n;

if rho_min ~= rho_max
    x_vector = rho_min + drho * [0 : n];
    xlabel_fig = sprintf('\\rho (mm)');
    title_fig = sprintf('Magnetic Field Profile as a Function of \\rho, z = %.1f mm',z_min);
else
    x_vector = z_min + dz * [0 : n];
    xlabel_fig = sprintf('z (mm)');
    title_fig = sprintf('Magnetic Field Profile as a Function of z, \\rho = %.1f mm',rho_min);
end

% if d == -1
%     if rho_min ~= rho_max
%           if d == -1
%         dBz_dz = (B_z(1) - B_z(0)) / dz;
%
%
%
%     else
%     dBrho_drho = (B_rho(1) - B_rho(0)) / drho;
%     end
% end
%

figure

if rho_min ~= rho_max
    plot(x_vector, B_rho, ':b', MEASURED_RHO_1, MEASURED_FIELD_RHO_1, '.r', ...
        MEASURED_RHO_2, MEASURED_FIELD_RHO_2, '*k')
    legend('simulated field','measured data (separate)', 'measured data (together)', 1)
else
    plot(x_vector, B_rho)
```

```
57 end
58
59 xlabel(xlabel_fig)
60 ylabel('magnetic field B_{\rho} (Gauss)')
61 title(title_fig)
62 if d == -1 && rho_min ~= rho_max
63     text_fig = sprintf('dB_\\rho/d\\rho(\\rho = 0) = %.2f G / cm', (B_rho(2) - ...
           B_rho(1))/drho * 10);
64     text(0, 0, text_fig)
65     text(10,-10, 'from simulation')
66 end
67
68 figure
69
70 if z_min ~= z_max
71     plot(x_vector, B_z, ':b', MEASURED_Z_1, MEASURED_FIELD_Z_1, '.r', MEASURED_Z_2, ...
           MEASURED_FIELD_Z_2, '*k')
72     legend('simulated field','measured data (separate)', 'measured data (together)', 1)
73 else
74     plot(x_vector, B_z)
75 end
76 xlabel(xlabel_fig)
77 ylabel('magnetic field B_z (Gauss)')
78 title(title_fig)
79 if d == -1 && z_min ~= z_max
80     text_fig = sprintf('dB_z/dz(z = 0) = %.2f G / cm', (B_z(n/2 + 1) - B_z(n/2))/dz * 10);
81     text(0, 0, text_fig)
82     text(10,-10, 'from simulation')
83 end
```

A.4 Optical pumping at 684 nm

This section describes the optical pumping theory and simulation we considered in the case of possible spin-impurity of atoms from the narrow-line cooling, which is not implemented in our current set-up.

A.4.1 Theory and simulation result

In order to reduce the spin and dipolar relaxation, which causes heating and atom number loss, all the population in the Zeeman sub-levels needs to be transferred to the energetically lowest Zeeman sub-level.

By shining the σ^- laser beam with a homogeneous magnetic field, which defines the quantization axis, the population initially distributed in the Zeeman sub-levels are pumped to the lowest Zeeman sub-level [Fig. A.3 (a)]. In addition, using the optical transition from $J = 8$ to $J' = 8$ (for bosonic isotopes), one can optically pump the atoms to the dark state $m_J = -8$, where the atoms do not scatter any photon. In the optical pumping, there are two important experimental parameters to be considered: the wavelength and the spontaneous decay rate of the transition used.

The 684-nm transition (Fig. 2.2) has been chosen to minimize heating in the optical pumping process. As the atom is optically pumped toward the dark state, it scatters photons, which results in the energy increase in the atom. In this scattering process[1], the energy transferred is

$$\Delta E = \sqrt{N_{\rm p}}\,\frac{\hbar^2 k^2}{2m} \tag{A.1}$$

where $N_{\rm p}$ is the number of scattered photons and k is the wavevector of the photon. Therefore, the longer wavelength causes less heating to the atom.

The next consideration is the spontaneous decay rate, which determines the scattering rate and the pumping time. Although there are no empirical or theoretical data of the spontaneous decay rate γ on the 684-nm transition, γ is (roughly) estimated to be 360 kHz, by comparing the relative intensities. Before experimentally implementing the optical pumping, computer simulation was done. The time evolution of the optical pumping process is described by a set of rate equations with Clebsch-Gordon coefficients [72]:

$$\begin{aligned}
\dot{P}_m(t) &= P_{m+1}(t)\Gamma_s({}^8_8CG^-_{m+1}s^-_{m+1})^8_8CG^0_m \\
&+ P_{m+2}(t)\Gamma_s({}^8_8CG^-_{m+2}s^-_{m+2})^8_8CG^+_m \\
&- P_m(t)\Gamma_s({}^8_8CG^-_m s^-_m)({}^8_8CG^0_{m-1} + {}^8_8\,CG^+_{m-2}),
\end{aligned} \tag{A.2}$$

where the photon scattering rate $\Gamma_s(s)$ has dependence on a saturation parameter s as

$$\Gamma_s(s) = \frac{\Gamma}{2}\frac{s}{s+1}, \tag{A.3}$$

and the saturation parameter dependent on the magnetic field has a following expression as

$$s^-_m = \frac{s_0}{1 + s_0 + 4(\delta + ((m-1)g_e - mg_g)\mu_{\rm B}B/\hbar)^2/\Gamma^2}. \tag{A.4}$$

[1]This scattering is a random walk in the momentum space.

The simulation parameters are the beam intensity of 1.5 mW/cm^2, the magnetic field of 3 G, and zero detuning and its result is shown in Fig. A.3 (b). The optical pumping time of 10 ms is negligible, compared to the life ($\sim$ min) of the optical dipole trap. Using the the optical pumping time and the scattering rate, N_{p} is estimated to be 45, and thus $\Delta E \lesssim 1\,\mu\ \mathrm{K} \cdot k_{\mathrm{B}}$.

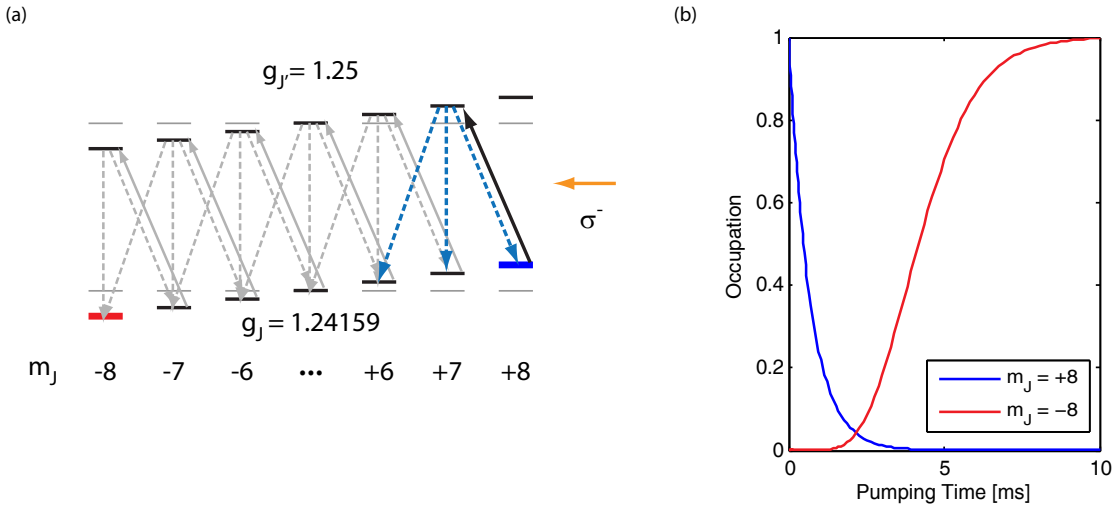

Figure A.3: Optical pumping at the 684-nm transition. (a) The population transfer scheme by the optical pumping. (b) The time evolution of Zeeman sub-levels from simulation with the scattering rate of $0.004\gamma/2$.

A.4.2 DysprosiumOpticalPumpingTheory.m

```
%% DysprosiumOpticalPumpingTheory.m

% THIS MATLAB SCRIPT SIMULATES THE OPTICAL PUMPING AND PLOTS THE POPULATION
% OF EACH STATE OF m_J (GROUND STATE) AS A FUNCTION OF TIME.
% VERSION 1.0
% 10/20/2009
% SEO HO YOUN
% REFERENCE ON THEORY : WERNER THESIS PFAU GROUP P.92

clc
close all
clear all

global hbar muB Gamma I_s ge gg I delta B dm Gamma_s

```

```
%% LASER COOLING AND TRAPPING PARAMETERS OF DYSPROSIUM
Gamma = 2*pi * 360e3; % Estimated natural linewidth, s^-1
ge = 1.25; % Lande-g factor for excited state
lambda = 684e-7; % Vacuum wavelength of Dysprosium, cm

c = 29979245800; % Speed of light, cm / s
hbar = 6.6261 * 10^(-27) / (2 * pi); % Reduced Planck constant, erg * s
muB = 0.927 * 10^(-20); % Bohr magneton, erg / G
I_s = pi*hbar*2*pi*c*Gamma/(3*lambda^3) / 10^4; % Saturation intensity as a two-level ...
    atom, mW/cm^2
gg = 1.24159; % % Lande-g factor for ground state

%% SIMULATION SETTINGS
I = 10 *I_s; % Intensity of laser field for optical pumping, mW/cm^2
display(I)

delta = - 0 * Gamma; % detuning of optical pumping laser field, s^-1
B = 3; % Magnetic field, Gauss
dm = 9; % Offset used in simulation to avoid the negative index

%% SOLVE THE COUPLED DIFFERENTIAL EQUATIONS AND PLOT THE SOLUTIONS

tLimit = 10e-3;
[t,y] = ode45('DysprosiumP', [0 tLimit], [1 0 0 0 0 0 0 0 0 0 0 0 0 0 0 0 0]);
t = t*10^3;
tLimit = tLimit*10^3;

figure(1)
plot(t,y(:,1),t,y(:,2),t,y(:,3),t,y(:,4),t,y(:,5),t,y(:,6),t,y(:,7),...
    t,y(:,8),t,y(:,9),t,y(:,10),t,y(:,11),t,y(:,12),t,y(:,13),t,y(:,14),...
    t,y(:,15),t,y(:,16),t,y(:,17))
xlabel('Pumping Time [ms]')
ylabel('Occupation')
title(sprintf('Theoretical Calculation of the Optical Pumping Process (\\sigma^+) of ...
    Dysprosium, Effective Scattering Rate \\gamma/2 * s/(1+s) = %.3f \\gamma/2', ...
    mean(Gamma_s)/(Gamma/2)))
legend('m_J = -8', 'm_J = -7', 'm_J = -6', 'm_J = -5','m_J = -4','m_J = -3',...
    'm_J = -2','m_J = -1','m_J = 0','m_J = +1','m_J = +2','m_J = +3','m_J = +4','m_J = ...
        +5','m_J = +6','m_J = +7','m_J = +8','Location','EastOutside')
xlim([0 tLimit])
```

```
52 ylim([0 1])
53
54 figure(2)
55 plot(t,y(:,1),t,y(:,17))
56 xlabel('Pumping Time [ms]')
57 ylabel('Occupation')
58 title(sprintf('Theoretical Calculation of the Optical Pumping Process (\\sigma^-) of ...
       Dysprosium, Effective Scattering Rate \\gamma/2 * s/(1+s) = %.3f \\gamma/2', ...
       mean(Gamma_s)/(Gamma/2)))
59 legend('m_J = +8', 'm_J = -8','Location','EastOutside')
60 xlim([0 tLimit])
61 ylim([0 1])
```

A.4.3 DysprosiumP.m

This code requires ClebschGordan.m (available at Ref. [96]) and Wigner3j.m (avalable at Ref. [97]).

```
1  function dydt = DysprosiumP(t, y)
2
3  % Solve optical pumping theory, Werner thesis p.91
4
5  global hbar muB Gamma I_s ge gg I delta B dm Gamma_s
6
7  %% SIMULATION PARAMETER CALCULATION
8
9  % s = zeros(17,1);
10 % Gamma_s = zeros(17,1);
11 % CGm = zeros(17,1);
12 % CGp = zeros(17,1);
13 % CG0 = zeros(17,1);
14 % % index is the m_J for the ground state
15
16 for m = -8 : 7
17     CGm(m + 1 + dm) = ClebschGordan(8, 1, 8, m + 1, -1, m)^2;
18     CGp(m + dm) = ClebschGordan(8, 1, 8, m, +1, m + 1)^2;
19     % ClebschGordan(J,J_photon,J',m_J, m_photon ,m_J') m_photon = +1 for
20     % sigma^+, m_photon = -1 for sigma^-, m_photon = 0 for pi polarization
21 end
22 for m = -8 : 8
```

```
    CG0(m + dm) = ClebschGordan(8, 1, 8, m, 0, m)^2;
end

for m = -8:7
    s = (I/I_s) / (1 + 4*(delta + (ge*(m + 1) - gg*m)*muB * B / hbar)^2 / Gamma^2);
    Gamma_s(m + dm) = Gamma / 2 * CGp(m+dm)*s / (CGp(m+dm)*s + 1);
end

%% COUPLED DIFFERENTIAL EQUATIONS
dydt = zeros(size(y));

for m = -8 : 8
    if m == -8
        dydt(m+dm) = - y(m+dm)*Gamma_s(m+dm)*(CG0(m+1+dm) + CGm(m+2+dm));
    elseif m == -7
        dydt(m+dm) = y(m-1+dm)*Gamma_s(m-1+dm)*CG0(m+dm)...
            - y(m+dm)*Gamma_s(m+dm)*(CG0(m+1+dm) + CGm(m+2+dm));
    elseif m == 7
        dydt(m+dm) = y(m-1+dm)*Gamma_s(m-1+dm)*CG0(m+dm)...
            + y(m-2+dm)*Gamma_s(m-2+dm)*CGm(m+dm)...
            - y(m+dm)*Gamma_s(m+dm)*CG0(m+1+dm);
    elseif m == 8
        dydt(m+dm) = y(m-1+dm)*Gamma_s(m-1+dm)*CG0(m+dm)...
            + y(m-2+dm)*Gamma_s(m-2+dm)*CGm(m+dm);
    else
        dydt(m+dm) = y(m-1+dm)*Gamma_s(m-1+dm)*CG0(m+dm)...
            + y(m-2+dm)*Gamma_s(m-2+dm)*CGm(m+dm)...
            - y(m+dm)*Gamma_s(m+dm)*(CG0(m+1+dm) + CGm(m+2+dm));
    end

end
```

Appendix B

CAD

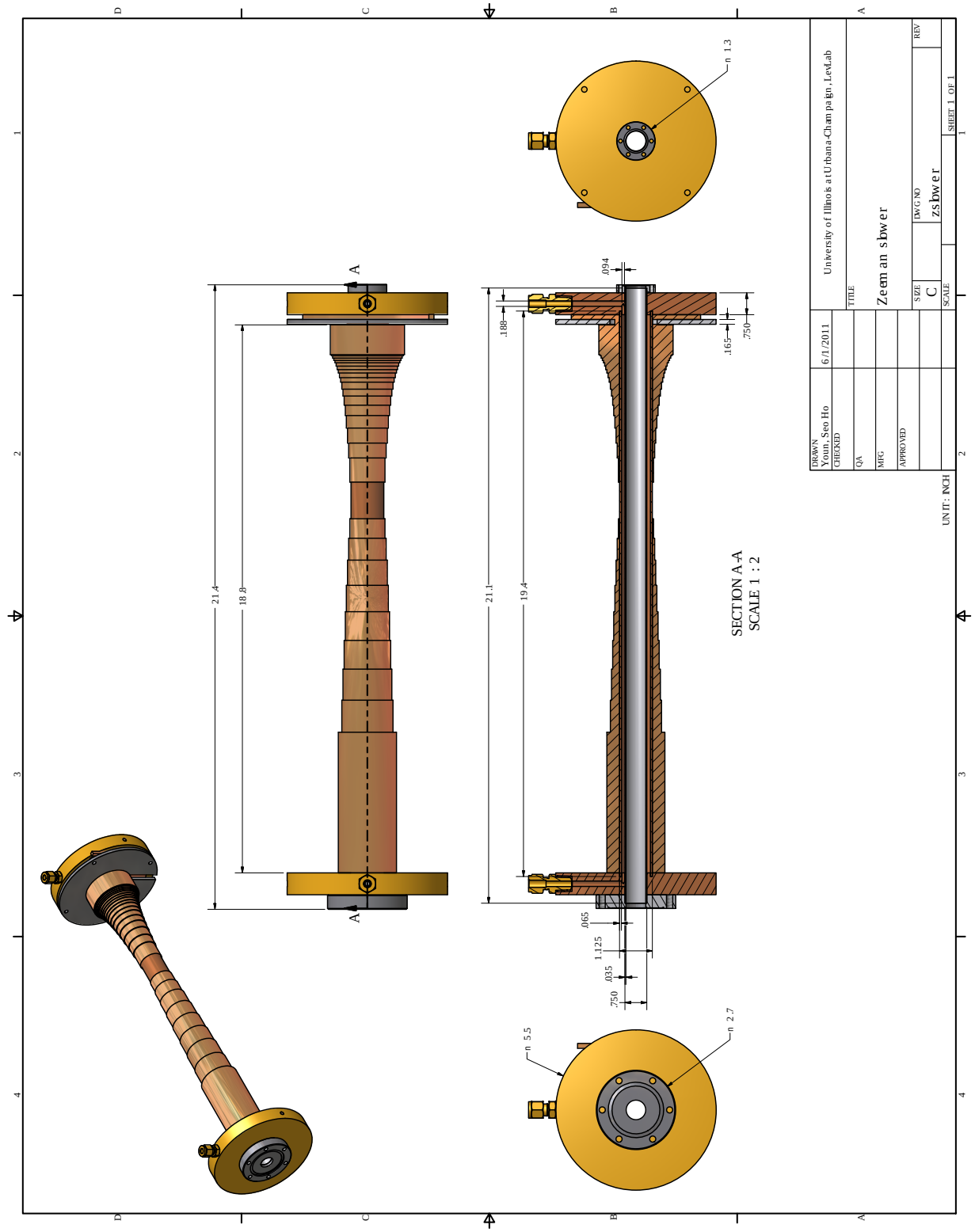

Figure B.1: Zeeman slower.

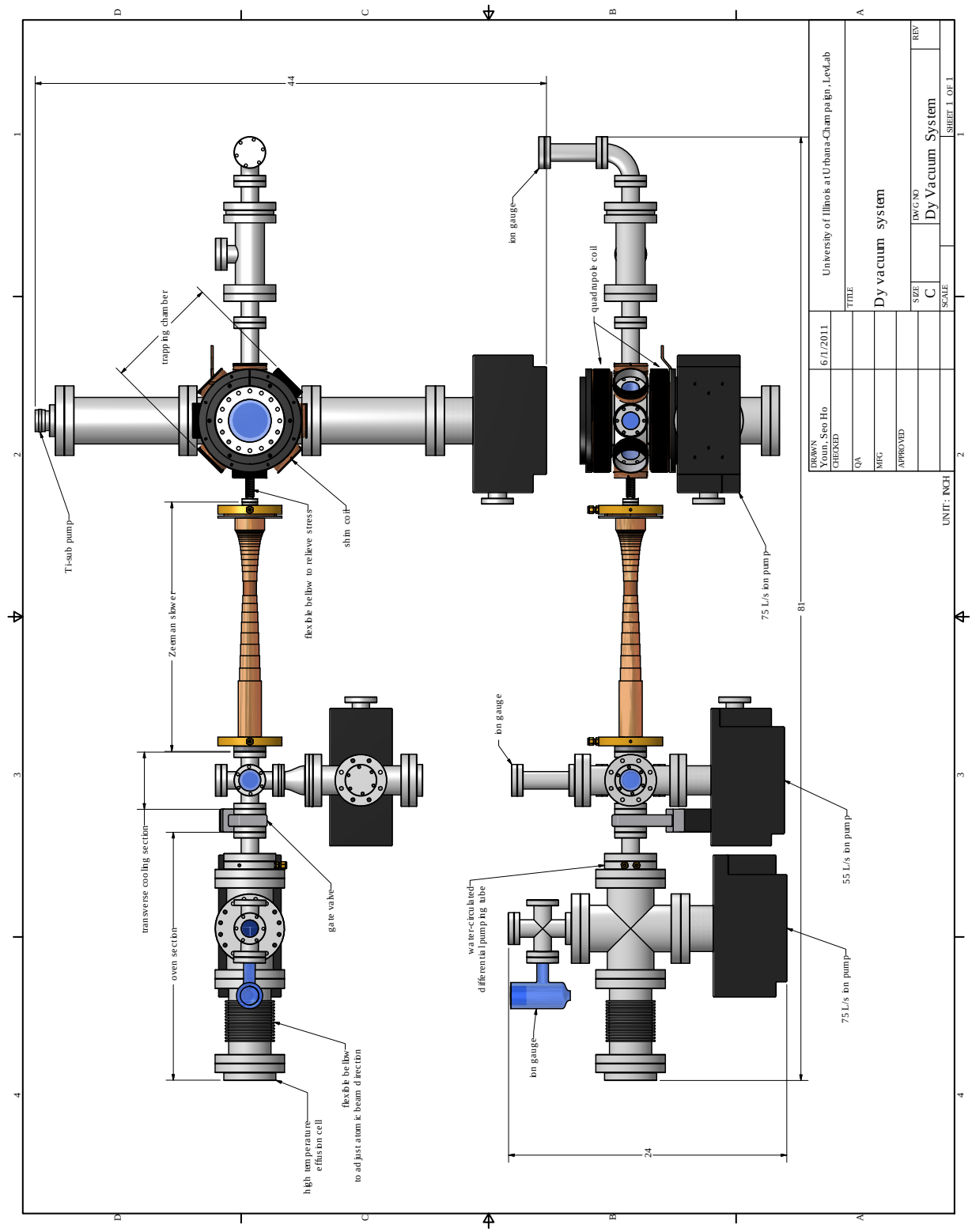

Figure B.2: Dy vacuum system.

References

[1] Emsley, J. *The Elements* (Oxford Univ. Press, New York, 1995).

[2] Lu, M., Youn, S. H. & Lev, B. L. Spectroscopy of a narrow-line laser-cooling transition in atomic dysprosium. *Phys. Rev. A* **83**, 012510 (2011).

[3] Lahaye, T., Menotti, C., Santos, L., Lewenstein, M. & Pfau, T. The physics of dipolar bosonic quantum gases. *Rep. Prog. Phys.* **72**, 126401 (2009).

[4] Fradkin, E., Kivelson, S. A. & Oganesyan, V. Electron Nematic Phase in a Transition Metal Oxide. *Science* **315**, 196 (2007).

[5] Fradkin, E., Kivelson, S. A., Lawler, M. J., Eisenstein, J. P. & Mackenzie, A. P. *Annu. Rev. Condens. Matter Phys.* **1**, 7 (2010).

[6] *CRC Handbook of Chemistry and Physics* (CRC Press, New York, 2010), 91st edn.

[7] Martin, W. C., Zalubas, R. & Hagan, L. *Atomic Energy Levels–The Rare Earth Elements* (NSRDS-NBS, **60**, Washington, D.C., 1978).

[8] Leefer, N., Cingöz, A. & Budker, D. Measurement of hyperfine structure and isotope shifts in the Dy 421 nm transition. *Opt. Lett.* **34**, 2548 (2009).

[9] Hancox, C. *Magnetic Trapping of transition-metal and rare-earth atoms using buffer gas loading.* Ph.D. thesis, Harvard University (2005).

[10] White, M. R. *Ultracold atoms in a disordered optical lattice.* Ph.D. thesis, University of Illinois at Urbana-Champaign (2009).

[11] Youn, S. H., Lu, M. & Lev, B. L. Anisotropic sub-Doppler laser cooling in dysprosium magneto-optical traps. *Phys. Rev. A* **82**, 043403 (2010).

[12] Metcalf, H. J. & van der Straten, P. *Laser Cooling and Trapping* (Springer-Verlag, New York, 1999).

[13] van der Straten, P., Shang, S.-Q., Sheehy, B., Metcalf, H. & Nienhuis, G. Laser cooling at low intensity in a strong magnetic field. *Phys. Rev. A* **47**, 4160 (1993).

[14] Leefer, N., Cingöz, A. & Budker, D. Measurement of hyperfine structure and isotope shifts in the Dy 421-nm transition (2009). `arxiv:0904.1438v2`.

[15] Anderson, M. H., Ensher, J. R., Matthews, M. R., Wieman, C. E. & Cornell, E. A. Observation of Bose-Einstein Condensation in a Dilute Atomic Vapor. *Science* **269**, 198 (1995).

[16] Davis, K. B. *et al.* Bose-Einstein Condensation in a Gas of Sodium Atoms. *Phys. Rev. Lett.* **75**, 3969 (1995).

[17] Bradley, C. C., Sackett, C. A., Tollett, J. J. & Hulet, R. G. Evidence of Bose-Einstein Condensation in an Atomic Gas with Attractive Interactions. *Phys. Rev. Lett.* **75**, 1687 (1995).

[18] Anglin, J. R. & Ketterle, W. Bose-Einstein condensation of atomic gases. *Nature* **416**, 211 (2002).

[19] DeMarco, B. & Jin, D. S. Onset of Fermi Degeneracy in a Trapped Atomic Gas. *Science* **285**, 1703 (1999).

[20] Chu, S. Cold atoms and quantum control. *Nature* **416**, 206 (2002).

[21] Griesmaier, A., Werner, J., Hensler, S., Stuhler, J. & Pfau, T. Bose-Einstein Condensation of Chromium. *Phys. Rev. Lett.* **94**, 160401 (2005).

[22] Fradkin, E. & Kivelson, S. A. Electron Nematic Phases Proliferate. *Science* **327**, 155 (2010).

[23] Miyakawa, T., Sogo, T. & Pu, H. Phase-space deformation of a trapped dipolar Fermi gas. *Phys. Rev. A* **77**, 061603 (2008).

[24] Fregoso, B. M., Sun, K., Fradkin, E. & Lev, B. L. Biaxial nematic phases in ultracold dipolar Fermi gases. *New J. Phys.* **11**, 103003 (2009).

[25] Quintanilla, J., Carr, S. T. & Betouras, J. J. Metanematic, smectic, and crystalline phases of dipolar fermions in an optical lattice. *Phys. Rev. A* **79**, 031601 (2009).

[26] Fregoso, B. M. & Fradkin, E. Ferronematic Ground State of the Dilute Dipolar Fermi Gas. *Phys. Rev. Lett.* **103**, 205301 (2009).

[27] Fregoso, B. M. & Fradkin, E. Unconventional magnetism in imbalanced Fermi systems with magnetic dipolar interactions. *Phys. Rev. B* **81**, 214443 (2010).

[28] Doyle, J., Friedrich, B., Krems, R. & Masnou-Seeuws, F. Editorial: Quo vadis, cold molecules? *Eur. Phys. J. D* **31**, 149 (2004).

[29] Ospelkaus, S. *et al.* Ultracold polar molecules near quantum degeneracy. *Faraday Discuss.* **142**, 351 (2009).

[30] Ospelkaus, S. *et al.* Quantum-State Controlled Chemical Reactions of Ultracold Potassium-Rubidium Molecules. *Science* **327**, 853 (2010).

[31] Ni, K. K. *et al.* Dipolar collisions of polar molecules in the quantum regime. *Nature* **464**, 1324 (2010).

[32] Giovanazzi, S., Görlitz, A. & Pfau, T. Tuning the Dipolar Interaction in Quantum Gases. *Phys. Rev. Lett.* **89**, 130401 (2002).

[33] Sukachev, D. *et al.* Magneto-optical trap for thulium atoms. *Phys. Rev. A* **82**, 011405(R) (2010).

[34] Yi, S., Li, T. & Sun, C. P. Novel Quantum Phases of Dipolar Bose Gases in Optical Lattices. *Phys. Rev. Lett.* **98**, 260405 (2007).

[35] Chan, Y.-H., Han, Y.-J. & Duan, L.-M. Supersolid and charge density-wave states from anisotropic interaction in an optical lattice (2010). `arxiv:1005.1270`.

[36] Lahaye, T. *et al.* Strong dipolar effects in a quantum ferrofluid. *Nature* **448**, 672 (2007).

[37] McClelland, J. J. & Hanssen, J. Laser Cooling without Repumping: A Magneto-Optical Trap for Erbium Atoms. *Phys. Rev. Lett.* **96**, 143005 (2006).

[38] Chicireanu, R. *et al.* Simultaneous magneto-optical trapping of bosonic and fermionic chromium atoms. *Phys. Rev. A* **73**, 053406 (2006).

[39] Hancox, C. I., Doret, S. C., Hummon, M. T., Luo, L. & Doyle, J. M. Magnetic trapping of rare-earth atoms at millikelvin temperatures. *Nature* **431**, 281 (2004).

[40] Newman, B. *et al.* (2010). To be published.

[41] Wang, B., Wang, D.-W. & Sarma, S. D. Bose-Fermi solid and its quantum melting in a one-dimensional optical lattice. *Phys. Rev. A* **82**, 021602(R) (2010).

[42] Sadler, L., Higbie, J. M., Leslie, S. R., Vengalattore, M. & Stamper-Kurn, D. M. Spontaneous symmetry breaking in a quenched ferromagnetic spinor Bose-Einstein condensate. *Nature* **443**, 312 (2006).

[43] Wu, C. Hidden symmetry and quantum phases in spin-3/2 cold atomic systems. *Mod. Phys. Lett. B* **20**, 1707 (2006).

[44] Baym, G. & Hatsuda, T. Private communication (2009).

[45] Li, Y. & Wu, C. The j-triplet Cooper pairing with magnetic dipolar interactions (2010). `arxiv: 1005.0889`.

[46] Ronen, S. & Bohn, J. L. Zero sound in dipolar Fermi gases. *Phys. Rev. A* **81**, 033601 (2010).

[47] Ronen, S., Bortolotti, D. C. E. & Bohn, J. L. Radial and Angular Rotons in Trapped Dipolar Gases. *Phys. Rev. Lett.* **98**, 030406 (2007).

[48] Leefer, N. A. *et al.* 34–43 (World Scientific, Singapore, 2009). Proceedings of the 7th Symposium on Frequency Standards and Metrology.

[49] Derevianko, A. & Cannon, C. Quantum computing with magnetically interacting atoms. *Phys. Rev. A* **70**, 062319 (2004).

[50] Saffman, M. & Mølmer, K. Scaling the neutral-atom Rydberg gate quantum computer by collective encoding in holmium atoms. *Phys. Rev. A* **78**, 012336 (2008).

[51] Connolly, C. B., Au, Y. S., Doret, S. C., Ketterle, W. & Doyle, J. M. Large spin relaxation rates in trapped submerged-shell atoms. *Phys. Rev. A* **81**, 010702 (2010).

[52] Dalmonte, M., Pupillo, G. & Zoller, P. One-Dimensional Quantum Liquids with Power-Law Interactions: The Luttinger Staircase. *Phys. Rev. Lett.* **105**, 140401 (2010).

[53] Moore, M. G. & Sadeghpour, H. R. Controlling two-species Mott-insulator phases in an optical lattice to form an array of dipolar molecules. *Phys. Rev. A* **67**, 041603 (2003).

[54] Petrov, D. S., Salomon, C. & Shlyapnikov, G. V. Diatomic molecules in ultracold Fermi gases - novel composite bosons. *J. Phys. B* **38**, S645 (2005).

[55] Bijlsma, M. J., Heringa, B. A. & Stoof, H. T. C. Phonon exchange in dilute Fermi-Bose mixtures: Tailoring the Fermi-Fermi interaction. *Phys. Rev. A* **61**, 053601 (2000).

[56] Bohn, J. L., Cavagnero, M. & Ticknor, C. Quasi-universal dipolar scattering in cold and ultracold gases. *New J. Phys.* **11**, 055039 (2009).

[57] Ticknor, C. & Rittenhouse, S. Three Body Recombination of Ultracold Dipoles to Weakly Bound Dimers. *Phys. Rev. Lett.* **105**, 013201 (2010).

[58] Ketterle, W. & van Druten, N. J. *Evaporative cooling of trapped atoms*, vol. 37, 181–236 (Academic Press, San Diego, CA, 1996). Advances in Atomic, Molecular, and Optical Physics, B.

[59] Youn, S. H., Lu, M., Ray, U. & Lev, B. L. Dysprosium magneto-optical traps. *Phys. Rev. A* **82**, 043425 (2010).

[60] Lu, M., Youn, S. H. & Lev, B. L. Trapping Ultracold Dysprosium: A Highly Magnetic Gas for Dipolar Physics. *Phys. Rev. Lett.* **104**, 063001 (2010).

[61] Kobtsev, S., Lev, B., Fortagh, J. & Baraulia, V. Powerful narrow-line source of blue light for laser cooling Yb/Er and Dysprosium atoms. *Proc. of SPIE* **7578**, 75782F–1 (2010).

[62] Schunemann, U., Engler, H., Grimm, R., Weidemuller, M. & Zielonkowski, M. Simple scheme for tunable frequency offset locking of two lasers. *Rev. Sci. Inst.* **70**, 242 (1999).

[63] Drever, R. W. P. *et al.* Laser Phase and Frequency Stabilization Using an Optical Resonator. *Appl. Phys. B* **31**, 97 (1983).

[64] Dzuba, V. A., Flambaum, V. V. & Lev, B. L. Dynamic polarizabilities and magic wavelengths for dysprosium. *Phys. Rev. A* **83**, 032502 (2010).

[65] Chikkatur, A. P. *Colliding and Moving Bose-Einstein Condensates: Studies of superfluidity and optical tweezers for condensate transport.* Ph.D. thesis, Massachusetts Institute of Technology (2002).

[66] Li, D. Reduction of residual gas in a sputtering system by auxiliary sputter of rare-earth metal. *J. Vac. Sci. Technol. A* **20**, 33 (2002).

[67] Leefer, N. *et al.* Transverse laser cooling of a thermal atomic beam of dysprosium. *Phys. Rev. A* **81**, 043427 (2010).

[68] Phillips, W. D. & Metcalf, H. Laser Deceleration of an Atomic Beam. *Phys. Rev. Lett.* **48**, 596 (1982).

[69] Barrett, T. E., Dapore-Schwartz, S. W., Ray, M. D. & Lafyatis, G. P. Slowing Atoms with σ^- Polarized Light. *Phys. Rev. Lett.* **67**, 3483 (1991).

[70] Boyd, M. *Novel Trapping Techniques For Shaping Bose-Einstein Condensates.* Ph.D. thesis, Massachusetts Institute of Technology (2006).

[71] Schmidt, P. O. *Scattering properties of ultra-cold chromium atoms.* Ph.D. thesis, Physikalisches Institut der Universität Stuttgart (2003).

[72] Werner, J. *Observation of Feshbach resonances in an ultracold gas of ^{52}Cr.* Ph.D. thesis, Physikalisches Institut der Universität Stuttgart (2006).

[73] Griesmaier, A. R. *Dipole-dipole interaction in a degenerate quantum gas: Bose-Einstein condensation of chromium atoms.* Ph.D. thesis, Physikalisches Institut der Universität Stuttgart (2006).

[74] Ban, H. Y., Jacka, M., Hanssen, J. L., Reader, J. & McClelland, J. J. Laser cooling transitions in atomic erbium. *Opt. Express* **13**, 3185 (2005).

[75] McClelland, J. J. Natural linewidth of the 401-nm laser-cooling transition in Er I. *Phys. Rev. A* **73**, 064502 (2006).

[76] Berglund, A. J., Lee, S. A. & McClelland, J. J. Sub-Doppler laser cooling and magnetic trapping of erbium. *Phys. Rev. A* **76**, 053418 (2007).

[77] Bernardini, M. *et al.* Air bake-out to reduce hydrogen outgassing from stainless steel. *J. Vac. Sci. Technol. A* **16**, 188 (1998).

[78] `http://www.mathworks.com/support/tech-notes/1100/1107.html#2`.

[79] Brzozowski, T. M., Maczynska, M., Zawada, M., Zachorowski, J. & Gawlik, W. Time-of-flight measurement of the temperature of cold atoms for short trap-probe beam distances. *J. Opt. B: Quantum Semiclass. Opt.* **4**, 62 (2002).

[80] Ellis, G. *Control System Design Guide Third Edition* (Elsevier Academic Press, USA, 2004).

[81] Berglund, A. & McClelland, J. J. Private communication (2009).

[82] Dzuba, V. A. & Flambaum, V. V. Theoretical study of some experimentally relevant states of dysprosium. *Phys. Rev. A* **81**, 052515 (2010).

[83] Stuhler, J. *et al.* Continuous loading of a magnetic trap. *Phys. Rev. A* **64**, 031405(R) (2001).

[84] Bradley, C. C., McClelland, J. J., Anderson, W. R. & Celotta, R. J. Magneto-optical trapping of chromium atoms. *Phys. Rev. A* **61**, 053407 (2000).

[85] Kim, K., Noh, H.-R., Ha, H.-J. & Jhe, W. Direct observation of the sub-Doppler trap in a parametrically driven magneto-optical trap. *Phys. Rev. A* **69**, 33406 (2004).

[86] Dalibard, J. & Cohen-Tannoudji, C. Laser cooling below the Doppler limit by polarization gradients: simple theoretical models. *J. Opt. Soc. Am. B* **6**, 2023 (1989).

[87] Ungar, P. J., Weiss, D. S., Riis, E. & Chu, S. Optical molasses and multilevel atoms: theory. *J. Opt. Soc. Am. B* **6**, 2058 (1989).

[88] Drewsen, M. *et al.* Investigation of sub-Doppler cooling effects in a cesium magneto-optical trap. *Appl. Phys. B* **59**, 283 (1994).

[89] Walhout, M., Dalibard, J., Rolston, S. L. & Phillips, W. D. $\sigma^+ - \sigma^-$ Optical molasses in a longitudinal magnetic field. *J. Opt. Soc. Am. B* **9**, 1997 (1992).

[90] Werner, J., Wallis, H. & Ertmer, W. Atoms with anomalous Zeeman effect in a 1D-magneto-optical molasses. *Opt. Commun.* **94**, 525 (1992).

[91] Xu, X. *et al.* Single-Stage Sub-Doppler Cooling of Alkaline Earth Atoms. *Phys. Rev. Lett.* **90**, 193002 (2003).

[92] Shang, S.-Q., Sheehy, B., Metcalf, H., van der Straten, P. & Nienhuis, G. Velocity-selective resonances and sub-Doppler laser cooling. *Phys. Rev. Lett.* **67**, 1094 (1991).

[93] Chang, S., Kwon, T.-Y., Lee, H.-S. & Minogin, V. G. Laser sub-Doppler cooling of atoms in an arbitrarily directed magnetic field. *Phys. Rev. A* **66**, 043404 (2002).

[94] Berglund, A., Hanssen, J. & McClelland, J. Narrow-Line Magneto-Optical Cooling and Trapping of Strongly Magnetic Atoms. *Phys. Rev. Lett.* **100**, 113002 (2008).

[95] `http://www.mathworks.cn/matlabcentral/fileexchange/328-tilefigs-m`.

[96] `http://www.mathworks.com/matlabcentral/fileexchange/5276-clebschgordan-m`.

[97] `http://www.mathworks.de/matlabcentral/fileexchange/5275-wigner3j-m`.

Vita

Youn, Seo Ho

Education

Aug. 2007 - Aug. 2011: University of Illinois at Urbana-Champaign

Ph.D. in Physics

Advisor: Professor Benjamin L. Lev

Field of study: atomic, molecular, and optical physics

Research topic: Bose-Fermi mixtures of ultracold gases of dysprosium

Sept. 2004 - June 2007: University of California, Los Angeles

B.S. in physics

Summa Cum Laude, June 2006

Undergraduate advisor: Professor Chun Wa Wong

Aug. 2001 - June 2004: El Camino Community College, Torrance, CA

Major in physics

Outstanding academic achievement award in physics, May 2004

Outstanding academic achievement award in mathematics, May 2003

March 1997 - Dec. 1997: Kyungwon University, Seongnam, South Korea

Major in electrical-electronic engineering

Academic Appointments

Jan. 2008 - July 2011: Research Assistantship

Design and rapid development of dysprosium apparatus

Vacuum procedures, lasers, optics, computer numerical analysis and programming, electronics, machining skills, CAD design and drawing

Sept. 2010 - Dec. 2010: Teaching Assistantship

Physics 401: *Classical Physics Laboratory*

Upper level laboratory course for physics and engineering majors

Teachers Ranked as Excellent by their Students, March 2011

Sept. 2008 - June 2009: Teaching Assistantship

NSF Entrepreneurial Leadership in Science Teaching and learning (EnLiST) program

Design of lecture and laboratory course for high school physics teachers

Construction of rubidium saturated absorption spectroscopy apparatus

Sept. 2007 - Dec. 2007: Teaching Assistantship

Physics 140: *How Things Work*

Introductory and hands-on experience physics course for non-science majors

Sept. 2005 - June 2007: Undergraduate Laboratory Assistantship

Design and numerical analysis of table-top experiments on classical mechanics of falling chains

Publications

M. Lu, S.-H. Youn, and B. L. Lev, Spectroscopy of a narrow-line laser cooling transition in atomic dysprosium, *Phys. Rev. A* **83**, 012510 (2011).

S.-H. Youn, M. Lu, and B. L. Lev, Anisotropic sub-Doppler laser cooling in dysprosium magneto-optical traps, *Phys. Rev. A* **82**, 043403 (2010).

S.-H. Youn, M. Lu, U. Ray, and B. L. Lev, Dysprosium magneto-optical traps, *Phys Rev A* **82**, 043425 (2010).

M. Lu, S.-H. Youn, B. L. Lev, Trapping ultracold dysprosium: A highly magnetic gas for dipolar physics, *Phys. Rev. Lett.* **104**, 063001 (2010).

C. W. Wong, S.-H. Youn, and K. Yasui, The falling chain of Hopkins, Tait, Steele and Cayley, *Eur. J. Phys.* **28**, 385 (2007).

C. W. Wong, S.-H. Youn, and K. Yasui, Two falling-chain demonstrations based on Einstein's equivalence principle, arXiv:physics/0609219v1 (2006).